Juan Manuel Costa Miscione

Evaluating the role of damage in the mechanics of chip segmentation

São Paulo

2022

Juan Manuel Costa Miscione

Evaluating the role of damage in the mechanics of chip segmentation

Document presented to the Graduate Program in Escola Politécnica of the Universidade de São Paulo as a partial requirement to obtain the degree of Master of Science

Escola Politécnica da Escola de São Paulo

Programa de Pós-Graduação em Engenharia Metalúrgica e de materials

Supervisor: Claudio Geraldo Schön

São Paulo

2022

Ficha catalográfica

Juan Manuel Costa Miscione

Evaluating the role of damage in the mechanics of chip segmentation

Document presented to the Graduate Program in Escola Politécnica of the Universidade de São Paulo as a partial requirement to obtain the degree of Master of Science

São Paulo, 27/12/2022:

Claudio Geraldo Schön
Supervisor

Professor
Alisson Rocha Machado

Professor
Ankit Srivastava

São Paulo
2022

STATEMENT OF AUTHORSHIP

I hereby declare that the thesis submitted is my own work. All direct or indirect sources used are acknowledged as references. I further declare that I have not submitted this thesis at any other institution in order to obtain a degree.

To my soon-to-be wife, who supported the distance. To my parents, who supported my Life. To the Lord, who supported my Soul.

ACKNOWLEDGEMENTS

"The riddles of God are more satisfying than the solutions of man"

G. K. Chesterton

ABSTRACT

The mechanics of chip segmentation is still controversial with regards to its root cause. Whether by thermoplastic instability or damage, chip segmentation is caused by local loss of strength of the chip in the region of primary shear. This work is mainly focused on the discussion of the different theories and the root cause of the phenomenon both by numerical and experimental viewpoints. Numerical experiments deal with the constitutive models that describe softening and damage in finite element simulations, while the experimental part deals with the phenomenon of chip segmentation in a brittle material with anomalous yield behavior, namely an iron aluminide intermetallic. This work concludes that damage mechanics dominate the phenomenon of chip segmentation, at least in materials with limited ductility, and that thermal effects are to be used only as an extension of the theory. In materials with considerable ductility, the numerical models cannot predict chip segmentation without the consideration of thermal effects, where the variables of thermal softening and softening due to damage strongly contribute to the phenomenon.

Keywords: damage, machining, simulation

LIST OF FIGURES

LIST OF TABLES

List of Equations

Nomenclature

$\dot{\gamma}$	strain rate	s^{-1}
$\dot{\varepsilon}$	shear rate	s^{-1}
γ	shear strain	-
λ	rake angle	$^{\circ}$
λ_t	thermal conductivity	$\mathrm{W\,m^{-1}\,K}$
$\mathbf{n_i}$	unit length direction vector	-
$\mathbf{T}_j^{(n)}$	traction vector	$\mathrm{N\,m^{-2}}$
s	stress deviator tensor	MPa
μ	*Lode* parameter	-
μ_f	friction coefficient	-
ϕ	primary shear angle	$^{\circ}$
σ_v	von Mises equivalent stress	MPa
σ_{ij}	components of the *Cauchy* stress tensor	MPa
σ_{NZ}	normal stress acting on the shear plane	MPa
τ	shear stress acting on the shear plane	MPa
θ_c	Lode angle	rad
ε	strain	-
h_s	segment length	μm
K_C	critical stress intensity factor	$\mathrm{MPa\,m^{1/2}}$
K_h	Hollomon's strength coefficient in hardening model	MPa
n	strain hardening exponent	-
$\mathbf{p}$	pressure	$\mathrm{N\,m^{-2}}$
A	Jonhson-Cook's flow stress coefficient	MPa

A_C	shear plane area	mm
B	Johnson-Cook's strength coefficient	MPa
C	Johnson-Cook's strain rate coefficient	-
F_P	principal horizontal cutting force	N
F_Q	principal vertical cutting force	N
h	depth of cut	mm
h'	chip thickness	mm
K	strength coefficient for hardening model	MPa
m	Johnson-Cook's thermal softening coefficient	-
R	machining main force	N
R'	reaction main force	N
R_C	chip cutting ratio	-
T	temperature	°C
V	cutting speed	$\mathrm{m\,s^{-1}}$
V_C	chip velocity	$\mathrm{m\,s^{-1}}$

ACRONYMS

APB	anti-phase boundary
FEM	Finite Element Method
IUS	International Unit System
PEEQ	Equivalent plastic deformation

CONTENTS

1 INTRODUCTION

According to Merchant [1], 15% of the price of all manufactured products arising from industrialized countries consist of machining costs. The fraction is naturally above average in case the material is a hard to machine one, such as a nickel superalloy or a titanium alloy. Hence, a major concern of machining is adequacy and optimization of parameters such as speeds and feeds [2], in addition to geometry, failure mechanisms and chemical composition of tool material [3].

The formal study of machining technology dates from 1882, and until now, there is no unified theory that explains all the different phenomena present in the process. Hill [4], had already proven, according to the uniqueness theory, that it is not possible to establish a single analytical and viable solution to the metal cutting problem based on a single shear angle. Hence, any attempt to solve the problem of the shear angle by analytical deduction would be unfruitful. The majority of the metal cutting theories are then *phenomenological*, *i.e.*, they are based on the observation and description of phenomena obtained by experimental methods.

The problem within a phenomenon-based model, for example the segmentation during machining, is in the incorrect root cause attribution. As it will be discussed in Section 1.2.4, there is a controversial debate regarding the root of the chip segmentation phenomena. Many works affirm that segmentation is the product of thermoplastic instability during high speed machining. Hence, the authors often develop modified constitutive equations based on high temperature softening. However, based on this root cause, it would be impossible to describe segmentation phenomena in low cutting speeds. Other authors affirm that segmentation is a fracture exclusive phenomenon, or at the very least, a mixture of both [5].

A theory can only be useful insofar as it can predict and describe the studied phenomenon in all conditions in which it is present. For that, the development of the machining technology will be integrally approached in this work — the different theories and constitutive models used in history to describe, predict forces, chip morphologies and increase productivity of the process — to finally develop a solution to the apparent contradiction between different chip segmentation theories.

1.1 MACHINING OPERATIONS

Machining is the most overarching process with regards to complexity. The combination of different tool and work materials, dimensions and geometries create an uncountable of possible outcomes and therefore, processing conditions [2]. Figure

1 presents different machining operations commonly found in industrial settings for different geometrical obtained features.
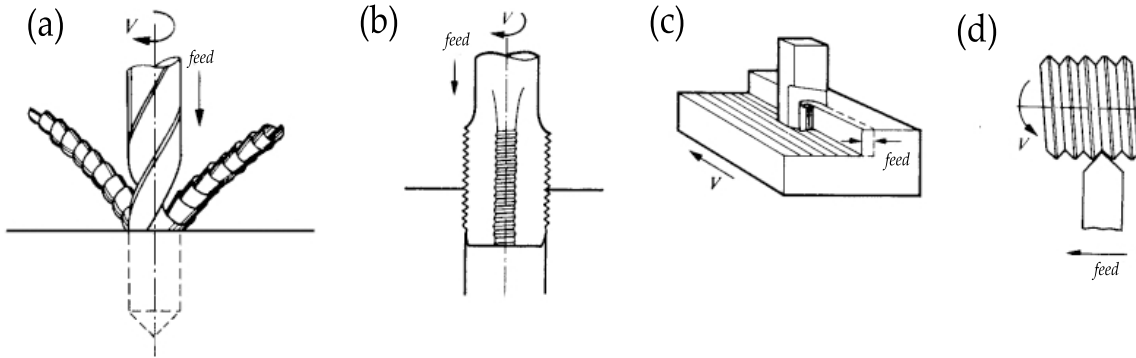
Figure 1 – Common machining operation. (a) drilling, (b) tapping, (c) planning e (d) threading. *Source*: adapted from [5]

Figure 2 illustrates the overarching of different industrial shape processing routes with regards to complexity (measured in an arbitrary unit C) and component size (em kg). Machining is highlighted in orange.
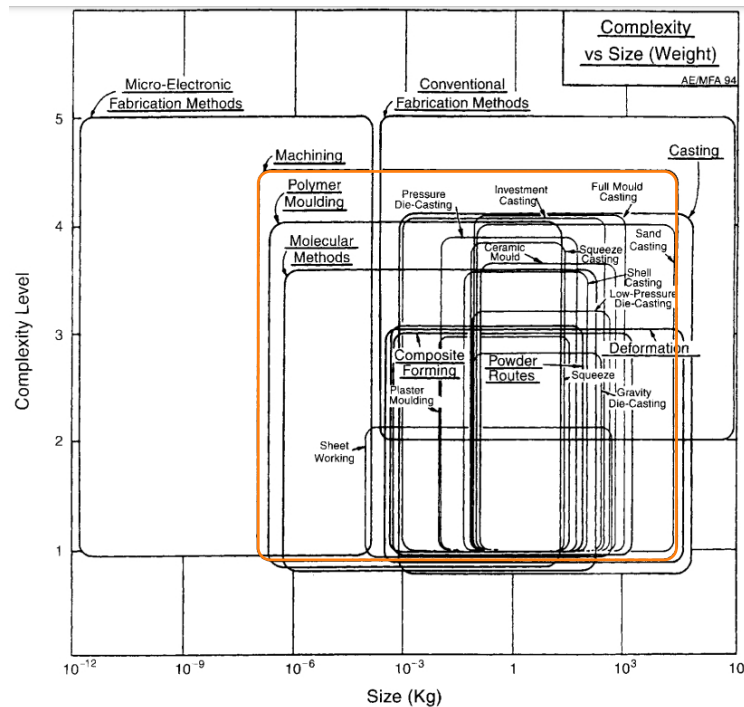
Figure 2 – Overarching of different industrial shape processing routes with regards to complexity (measured in an arbitrary unit C) and component size (in kg). *Source*: adapted from [6]

Despite the immense magnitude of variables, machining operations can be derived from a fundamental model: the orthogonal cutting model. This model is common to every other conventional machining process. This model is utilized to study machining due to the capacity to decompose forces in a single plane and thus determine chip

formation characteristics, stresses and deformation, deriving semi-orthogonal and/or oblique machining operations from it, such as in conventional turning or milling.

1.2 FUNDAMENTAL MACHINING THEORY

1.2.1 Mechanics of orthogonal cutting

As previously stated, forces involved in cutting and consequent stresses, deformation and shear rates applied to the material are among the major variables of interest in the studying of machining. These are fundamentally important to define parameters (materials, speeds and feeds) applicable to the material, and hence, its machinability. The variables that will further be discussed are derived by the *Piispanen*'s deck card model [7] that, despite its limitations, contains the fundamental features of the chip formation mechanism and simplifies the derivation of geometrical relations between tool and workpiece.

The model presented in Figure 3 is a transversal section of a chip produced by orthogonal cutting. The reason for using orthogonal cutting as a standard convention is because the forces can be decomposed in a single plane. A schematic model of orthogonal cutting is presented in Figure 4 (a), clearly illustrating the geometrical relations of the tool-workpiece pair and its respective resultant forces. The forces R and R′ are the forces between the tool face and the chip and the force between the workpiece and the chip along the shear plane, denoted in dashed lines in Figure 4 (a). For equilibrium conditions, these must be equal, R=R′. The material moves in a velocity V relative to the cutting edge, generating a chip with velocity V_C . The tool has a rake angle λ and cuts with a depth of cut h [5].
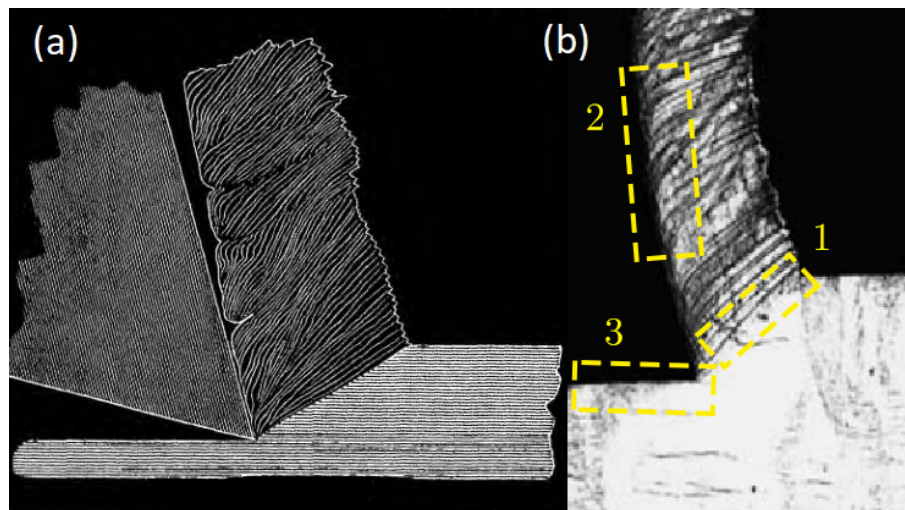
Figure 3 – (a) Illustration from Mallock's original work (1882) and (b) modern etched photomicrography of an orthogonal cutting chip section. Sources: (a) [8], (b) [9]

The forces R e R′ are usefully decomposed in three sets of forces that can be visually displayed in a circle with radius R, according to Merchant (1945) *apud* Machado et al. [10], as presented in Figure 4 (b):
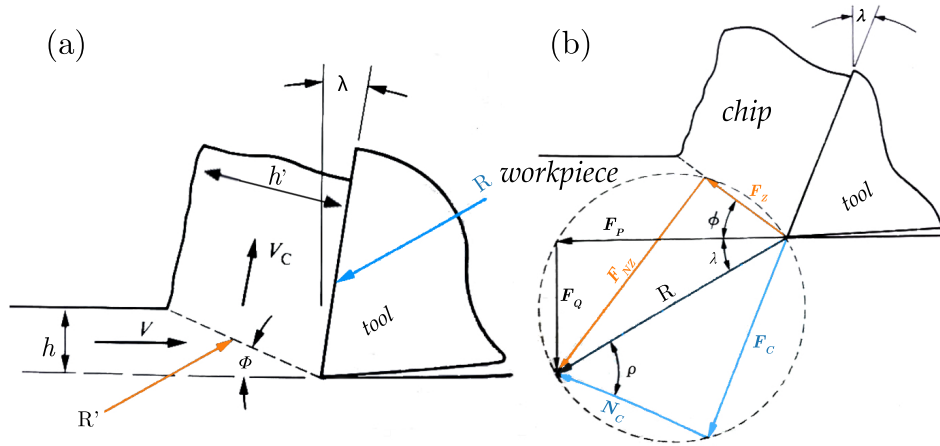
Figure 4 – Main machining and reaction forces, R e R' in orthogonal cutting e (b) free body diagram of the chip, with decomposed forces and geometric relations according to Merchant's circle [11]. *Source*: Modified from [5]

(1) in the horizontal and vertical directions, F_P e F_Q (principal horizontal and vertical cutting forces, respectively)

(2) across and perpendicular to the shearing plane, F_Z and F_{NZ}

(3) across and perpendicular to the tool face, F_C e N_C

The forces presented in item (1) are the decomposed of R, and are very useful, since they are perpendicular to each other and hence can be measured by dynamometry. They relate to the shear angle ϕ in order to calculate the forces acting on the shear plane (F_Z e F_{NZ}). Similarly, with the forces presented in item (1) we can also calculate acting forces on the interface between the tool and workpiece (F_C e N_C), according to the following equations:

$$F_Z = F_P \cos \phi - F_Q \sin \phi, \tag{1}$$

$$F_{NZ} = F_P \sin \phi + F_P \cos \phi, \tag{2}$$

$$F_{\mathrm{c}} = F_P \sin \lambda + F_Q \cos \lambda, \tag{3}$$

$$N_{\mathrm{c}} = F_P \cos \lambda - F_Q \sin \lambda. \tag{4}$$

After measuring horizontal and vertical forces (F_P e F_Q), the friction coefficient acting on the rake face (μ_f), the normal (σ_{NZ}) and shear stresses (τ_Z) acting on the shear plane can be determined, as obtained by the following equations:

$$\sigma_{NZ} = \frac{F_{NZ}}{A_C} = \frac{(F_P \cos\phi - F_Q \sin\phi)\sin\phi}{b\,h}, \tag{5}$$

$$\tau_Z = \frac{F_Z}{A_C} = \frac{(F_P \sin\phi - F_Q \cos\phi)\sin\phi}{b\,h}. \tag{6}$$

In orthogonal cutting, shear plane area A_C is related to the cutting depth (h) and cutting width (b) through the equation 7

$$A_c = \frac{b\,h}{\sin\phi}. \tag{7}$$

The only remaining variable of interest to relate with F_Q e F_P is the friction coefficient; this can be calculated through equation 8 ($\mu_f = \tan\rho$, in which ρ is the angle between e N_C as shown in Figure 4(b), also known as friction angle):

$$\mu_f = \frac{F_c}{N_c} = \frac{F_Q + F_P \tan\rho}{F_P - F_Q \tan\rho}. \tag{8}$$

Shear strain (γ) , according to Piispanen's model, can be defined as $\Delta S/\Delta Y$, as presented in figure 5 (a) as general shear and (b) in orthogonal cutting. Hence,

$$\gamma = \frac{\Delta S}{\Delta Y} = \frac{AD}{CD} + \frac{DB'}{CD} = \tan(\phi - \lambda) + \cot\phi, \tag{9}$$

or,

$$\gamma = \frac{\cos\lambda}{\sin\phi\cos(\phi - \lambda)} \tag{10}$$

The combination of orthogonal cutting energy consumption analysis and the representative data obtained by Merchant [11], results on the knowledge that most of the energy consumed ($\approx$70%) in the cutting process is expended in plastic deformation on the shear plane, while the fraction expended by friction between the tool and workpiece is about $^1/_3$ of total energy consumption [5].
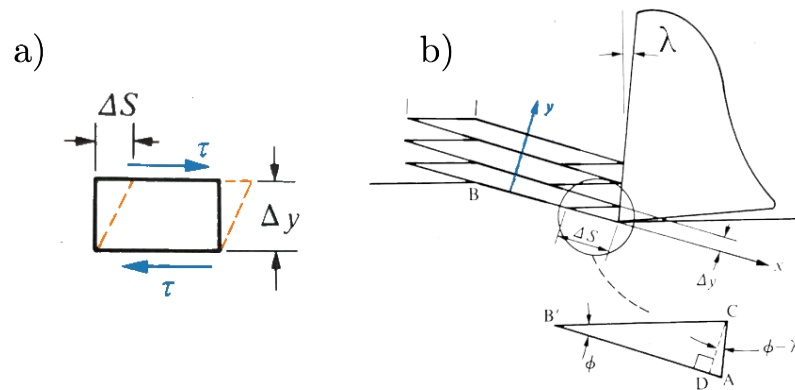
Figure 5 – Shear strain (a) generalized and (b) in orthogonal cutting. *Source*: Modified from [5]

The analytical equations presented in the previous paragraphs are derived from the Piispanen's deck card model (1937)[*] — a mere approximation of the real phenomenon, *i.e.*, it considers that that the all the plastic shear happens in a single perfect plane, that the friction between tool and workpiece is purely elastic, assumes an arbitrarily chosen shear plane, ignores the presence of *built-up edges* produced during cutting and the presence of secondary shear zones. However, the approximations are important to understand the fundamentals of orthogonal cutting: the presence of the primary shear zone and interaction between the chip and the tool's rake face.

It must be noted that in the majority of the previously proposed equations (1, 2, 5, 6 and 9), the ϕ angle is fundamentally important for the definition of the magnitude of stresses and strains. For determining ϕ, the micrographic method as presented in Figure 3 can be used. Although that is not viable for a large number of samples. Another useful method consists in determining the cutting ratio (R_C), defined as the uncut chip thickness (h)[†], as illustrated in Figure 4.

The aim of metallographic methods, theoretical models and finite element simulations is the attempt to predict the ϕ angle, as it is the most important variable in the chip formation mechanism and, hence, fundamental for the determination of forces and stresses produced by the cutting process. The following sections will describe the major theories and models that integrally attempt to describe the strain/strain-rate/temperature effect in chip formation, and the difficulties associated with it.

---

[*]Originally written in finnish (Väinö Piispanen, *Teknillinen Aikakauslenti* 27, 1937), the article was rewritten in english in 1948's *Journal of Applied Physics* volume. Besides the mathematical descriptions presented in the previous paragraphs, he also proposed a new theory of chip segmentation

[†]A vantage of using orthogonal cutting as a standard model is that the uncut chip thickness, under these conditions, is equal to the depth of cut (h=h′)

1.2.2   Chip formation analytical modelling

The first model that provided the geometrical and variable relations presented in equations 1-9 are derived from the Piispanen's [7] *deck of cards* model. However, as previously stated, this model is very limited, as it confines all the deformation in a single plane and considers the friction between *the pair*(tool-chip) to be fully elastic. This model was specifically presented in Figure 5(b).

Hastings; Mathew; Oxley [12] model fixed these issues. Friction, in this case, is not treated as purely elastic phenomena but also considered to be produced by a region of plastic shearing between the pair; this zone was previously defined as the *secondary shear zone*. The ϕ angle is product of the equilibrium between the forces normal to the tool in the interface of the pair and the forces acting in the *primary* shear zone, which itself depends on the resistance of the material, of the work done by the tool and the stresses distributed in the region region between A and B of Figure 6 (a). The orange zone represents the region on which the material is being plastically deformed. In Figure 6 (b), a finite element simulation of a SAE 4340 steel chip produced by the present author illustrates the accuracy of the model in attempting to represent both a primary and secondary shear zone, now not only restricted to a single plane. This model better represents the features of a real chip formation, such as the presented in Figure 3 (b).

Figure 6 – (a) Chip formation mechanism model according to Hastings; Mathew; Oxley [12], illustrating the primary and secondary shear zones and the speed relation between chip and workpiece and (b) simulation produced by the present author. *Sources*: (a) adapted from [12]. (b) Field variable results produced from a simulation by the current author

---

*6324 plane strain elements with approximately 5 μm characteristic length each, tool speed is 6 m s^{-1}, depth of cut is 0.2 mm and the plasticity and damage model used was a *Johnson-Cook* according to

The historical milestone achieved by Oxley's model is the consideration of the material properties to predict strength on the cutting conditions, these are known as to be variable in regards to strain rate and temperature, which can, in the case of ferrous alloys, under normal cutting speeds, reach up to 10^4 and 10^6 s^{-1}, with temperatures up to $150 - 250$ °C and $400 - 1200$ °C in the primary and secondary shear zone, respectively [2].

In Oxley's model, extrapolation of material behaviour in machining conditions, by means of constitutive equations, are:

- Strain hardening, as approximated by a Hollomon's parabolic law [14][*]:

$$\sigma = \mathrm{K}_h \, \varepsilon^n, \tag{11}$$

   where σ is the instantaneous yield strength, K_h is a material strength constant and n is the strain hardening exponent [14].

- Temperature and strain rate, on which k_{chip} the flow stress in the chip k_{chip} becomes a function of according to machining regime (mainly calculated strain and strain rates) with a velocity modified temperature $\mathrm{T}_{\mathrm{mod}}$ expressed in equation 12.

$$\mathrm{T}_{\mathrm{mod}} = \; T(1 - \nu \, log \frac{\dot{\varepsilon}}{\epsilon_0}), \tag{12}$$

where T is the calculated temperature, $\dot{\varepsilon}$ is the calculated shear rate, $\dot{\varepsilon_0}$ is a reference value, A, b, and ν are material constants fitted from experiments [17][†].

The Oxley's model, although being a realistic model based in competition of the forces in interfacial and primary shear zones, presents several disadvantages due to his analytical nature:

- Considering material property usage, too little experimental methods approximate to real obtained machining conditions: very high strain rates, deformations and

---

Sulaiman; Roshan; Ariffin [13]

[*]The effect of hardening with plastic deformation is a studied and applied phenomenon since the bronze age, its quantification and in-depth study came to be of interest in XX's century, with the development of dislocation theory and its relation to plastic deformation and strain hardening. See, *e.g.*, Hollomon [14], Ludwik [15] e Hirth [16]

[†]The velocity modified temperature was the first attempt at extrapolating material behaviour with regard both to temperature and strain rate [5]

temperatures for a good approximation of k_{AB} [*]. There also have been concerns [5] with regards to the strains being confined in very small volumes in comparison of those obtained in these tests

- The obtained temperatures, strains and strain rates don't contemplate the different chip types, as those presented in subsection 1.2.3

- The model depends in a contact length l_C, and according to Childs; Maekawa; Obikawa [9] *"the contact length is a difficult quantity to measure, and even to define [...] the 45% of the contact length furthest from the cutting edge may carry only 15% of the rake face load"*

- The model considers the solid as a perfectly ductile material, *i.e.*, no presence of negative strain hardening effects or fracture under large deformations, which seem to contradict experimental evidence [18]

The non-linear nature of the chip formation mechanism of a single metallic material results in a system on which analytical description becomes extremely difficult. A global analytical theory that spans through the description of the behaviour of all ductile metallic materials becomes nearly impossible. The behaviour of each material depends on an infinity of metallurgical and mechanical, micromechanisms of fracture and localized deformation variables that cannot be accounted for in simple equations and correlations. Models like Oxley's are restricted to a material niche [19]. Furthermore, there is an extensive need of extrapolations, approximations and testing to make the theory successful in predicting cutting forces and chip morphology. Different chip morphology obtained with different metallurgical and parametric cutting variables are presented in subsection 1.2.3. The great number of morphologies and different phenomena present in machining theory will be used as an argument for the difficulty of formulating global analytical cutting theories, alongside the proof by Hill *via* the uniqueness theory [4].

1.2.3 Types of chip

We can define two groups of chip types produced by a cutting edge according to morphology:

- Discontinuous chips, as those presented in Figure 7 (a) and (e)

- Continuous chips, which in turn are separated in:

---

[*]Strain rates obtained by impact testing can reach those when machining, but these tests are often restricted to strains up to 1, while in machining *apparent* strains of 40-50 are possible to be observed in the secondary shear zone [2]

(1) non-segmented, as presented in Figure 7 (b), (c) and (d)

(2) segmented, as presented in Figure 7 (f)
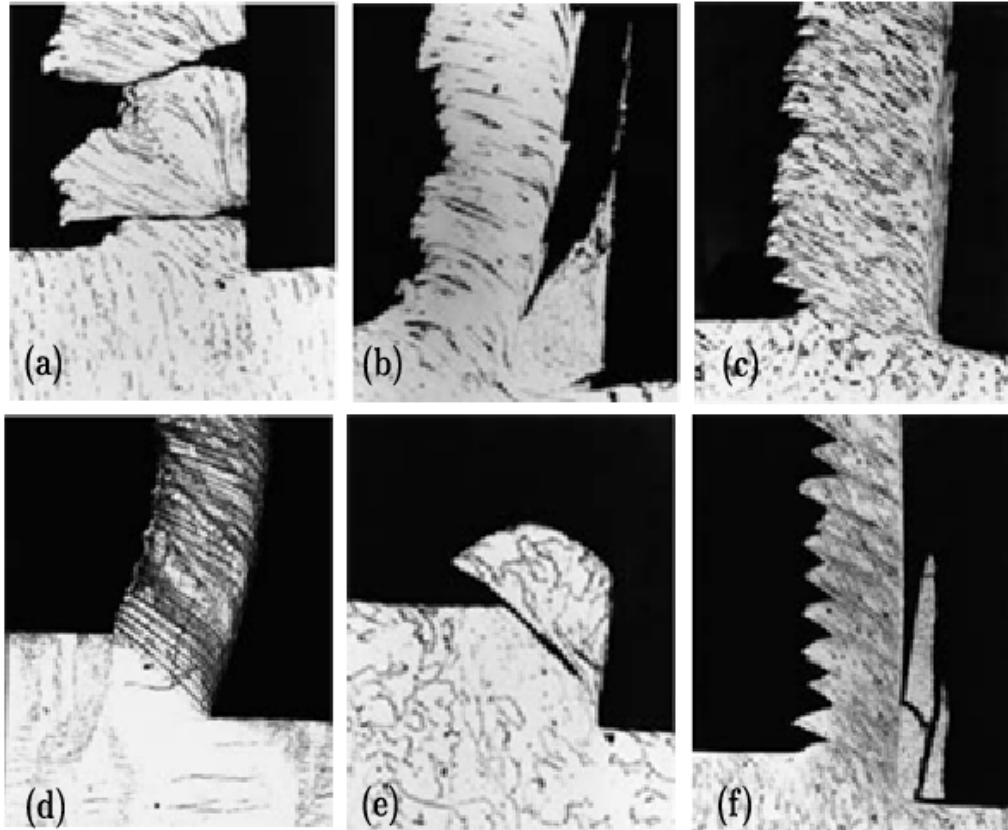
Figure 7 – Morphology of different chips obtained with 5 mm feed, for different materials and cutting speeds — cutting speeds are indicated in $[\text{m min}^{-1}]$: (a)[5], (b)[25] and (c)[55] are mild steel. (d)[50] is brass. (e)[120] is leaded brass. (f)[30] is austenitic stainless steel. *Source*: adapted from [9]

Figure 7 resumes the effects of different materials and machining condition's effect in resultant chip morphology. According to Childs; Maekawa; Obikawa [9], the main factors that determine chip morphology are (1) the deformation regime of the cutting material (strength, strain hardening, inelastic heat), (2) the interfacial condition of the pair (rake angle, contact and cutting tool geometry) and (3) friction between the pair (tribological characteristics).

The first row images of the Figure 7 illustrates the cutting speed variation's effect on chip morphology for the same material (in this case, mild steel), there is a clear discontinuity in the chip at low speeds, following the presence of a *built-up edge* in the pair's interface at in intermediate speeds and further stable cutting regime with a continuous non-segmented chip formation mechanism at higher speeds. According to Ernst (1938) *apud* Trent; Wright [2] the cause of segmentation in lower speeds is product of the high capacity of strain hardening of the material in low temperature deformation,

on which the hardened material strongly adheres to the tool's rake face, hampering the sliding of the chip through the rake face. High adhesion and seizure causes a great deformation on the shear plane and subsequent fracture in the free surface of the chip. This phenomenon can be identified by the very low ϕ angle and a greater secondary shear than of normal machining conditions — about ¼ to ½ of the chip thickness — as presented in Figure 7 (a).

By further increasing cutting speed from very low to intermediate (from ≈5 to ≈25, in the case of mild steel), the presence of the *built-up edge* begins to be observed in most alloys with considerable ductility and strain hardenability, such as presented in (b) and (f) of Figure 7. The built-up edge is one of the most important characteristic in ductile materials, as it has a great influence in cutting forces and superficial quality of the machined workpiece [2]. The built-up edge is formed due to the incapacity of the shear stresses in the pair's interface to continuously move the adhered material through the rake face of the tool. That is the result of a major feature of a metal cutting — the condition of *seizure**, according to Trent; Wright [2].

The built-up edge can be observed both through dynamometry and metallography. In a specific range of cutting speeds, a volume of the workpiece material itself adheres to the tool, creating a dummy edge, artificially increasing λ and reducing the forces necessary to produce the chip [9]. Figure 8 presents the variation of cutting forces F_Q e F_P with regards to cutting speed for different materials. It is possible to observe a decrease in cutting forces in the low to moderate cutting speeds, on which the speed range depends on the strain hardening nature of the material itself. Beyond speed, the built-up edge formation depends, naturally, on the tribological characteristics of the pair, *i.e.*, of the chip shearing condition in the secondary shear zone with regards to friction.

The built-up edge is a dynamic body that grows over the tool's movement until it loses its stability due to the interfacial shear stresses. The instability causes fracture of the highly strain hardened and geometrically acute body and subsequently directs it downwards the tool, causing it to damage the machined surface. Besides, when machining materials such as titanium and stainless steel, on which temperature, strain hardening and consequently tribochemical interaction between the pair becomes a major concern, adhesion between the built-up edge and the tool can become so strong as to catastrophically fracture the tool in very low contact times, turning the process non-viable [2].

---

*The condition of seizure is observed as approximating to the tool's rake face, where the relative speed of the chip and tool are virtually null and the material is sheared across the contact length, with little or no sliding in between the surfaces. The condition of seizure is more severe with higher strain hardenability (such as in metals with higher strain hardening exponent n), lower melting temperature or high thermodynamic affinity between the workpiece and tool materials
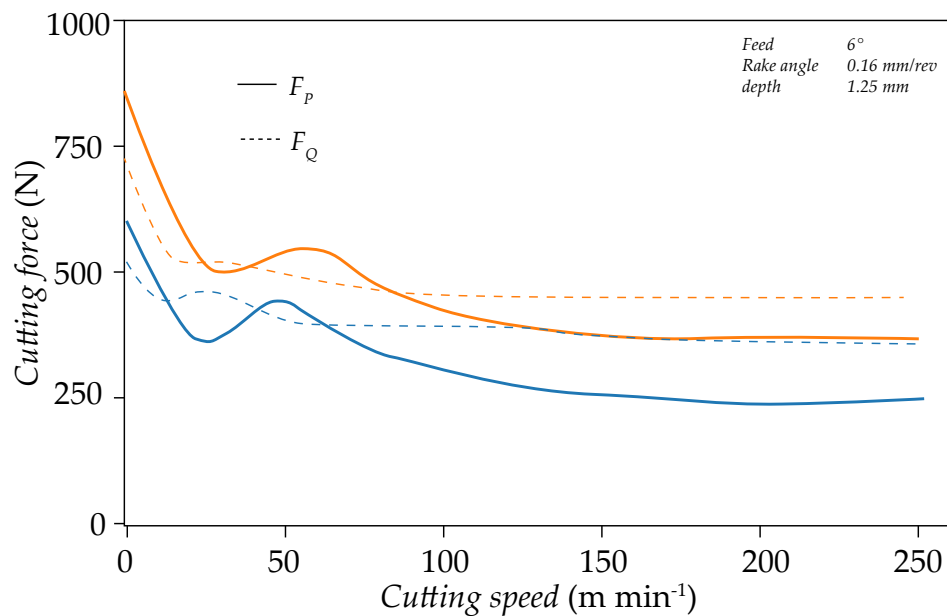
Figure 8 – Variation of cutting forces, F_P and F_Q with speed for a - - - austenitic stainless steel and - - - mild steel. *Source*: adapted from [2]

1.2.4 Mechanics of chip segmentation

The segmentation process, as presented in Figure 7 (f), is another recurrent mechanism of chip formation, sometimes present in every cutting condition for certain materials such as titanium alloys [20], nickel superalloys [21] and intermetallic alloys [22, 23]. In other materials, like steels and aluminium alloys, segmentation is present in specific machining conditions and/or specific heat treatments. Although much effort has been given in the development of constitutive laws to simulate tool forces during machining (*e.g.*, [24, 25]), flow stress models alone cannot give satisfactory results on chip morphology regarding segmentation and strain localization [5]. To be able to do so they require further modification based on its arbitrarily selected root cause. Chip segmentation and strain localization during chip formation remain controversial in regard to its physical cause: either adiabatic shear banding, as proposed by Komanduri; Schroeder [26] or periodic crack growth, as proposed by Shaw; Vyas [27] and Ueda; Iwata; Nakayama [28].

Adiabatic shear was initially believed to be the cause of chip segmentation in materials with poor thermal properties [29], like titanium [30] and nickel-based superalloys [26], as a result of the competition between adiabatic thermal softening and strain-hardening in the shear plane. Nevertheless, adiabatic shear banding alone cannot explain chip segmentation of brittle, or hardened, materials in low cutting speeds. In this case, chip segmentation can only be explained by a fracture-based model as discussed by Vyas (1999)[31]. While fracture has been extensively researched as to be fully responsible for the segmentation phenomena [32], the fact that the ductile shear

fracture is initialized at the tool tip rather than in the free surface results in an unrealistic approximation to experimental evidence (see, *e.g.*, [27, 33]).

Segmentation, as explained by fracture mechanics instead of purely through elastoplastic arguments, could explain not only pronounced segmentation [30], but the presence of surface roughness (as understood in chip formation as regions of strain localization) in the free surface of non-segmented chips. The latter is a major concern to machining technology as virtually every type of chip presents this characteristic as illustrated in Figure 7 (b), (d) and (c). Further development of a pure fracture mechanics model for chip segmentation simulation in finite element method will be made by the present author in Section 1.6.

In (d) and (e) of Figure 7, it can be observed the effect of a second dispersed phase in the chip formation mechanism of ductile materials. Second phase dispersion with negligible strengthening effects increases an alloy machinability *e.g.*, graphite in grey and ductile cast irons; lead in brasses and free machining steels; manganese sulfide and tin in aluminium alloys. These elements (C, S Pb and Sb) are strategically added to metallic alloys (or inherited from composition, such as gray and ductile irons) to facilitate the machining process — being either by reducing the cutting forces by producing stress concentrations in the matrix, either by reducing the stacking volume of chips due to chip breakage [34] or either by lubrication of the secondary shear zone due to low melting temperature of these constituents [5]. Alloys with these additions are named *free-cutting* alloys.

Vyas; Shaw, Komanduri; Brown [31, 20] presented the mechanism of chip segmentation due to the formation of microcracks along the shear plane in the presence of second phase particles, some of them are:

- dislocation pile up at a strong obstacle,

- pile up of immobile dislocations,

- pile up in the form of a low angle boundary,

- grain boundary fracture and

- separation of inclusions and formation of voids.

being the last item the most important mechanism for the formation of microcracks along shear bands in high strain regimes.

We can summarize by affirming that the chip formation mechanism is a complex process, which depends on the most diverse phenomena as the early discussed — segmentation, discontinuity, strain localization, free surface roughness and built-up edges.

These phenomena are hardly predictable by analytical global theories, such as those discussed in the current and 1.2.1 subsections. However difficult it is to correlate the different phenomena into a single theory, they present the same common characteristic: they tend to reduce the work done by the dynamic system — either through free surface fracture and roughness (as to decrease the excess work made through plastic deformation); either through the force reduction due to the presence of a built-up edge or through segmentation in order to reduce the shear plane extent. It is necessary, hence, a description that relates the necessity of the reduction of work made by the system with the metallurgical and parametrical properties of the process. This relation creates a non-linear relation between the major physical quantities of interest in metal machining. The best description that can be utilized to predict the behaviour of a dynamical system in a complex domain, according to the necessity of reduction of the total work done by it, is the variational description, based on a *hamiltonian* principle of minimum virtual work [35][*].

The *Finite Element Method* (FEM) is largely used in modern engineering to solve complex elasticity, plasticity, heat and mass transfer problems through discretization and division of the global problem – the *domain* – into smaller problems, where a corresponding variational is method applied in each *element* — the *subdomain*. This produces a very large system of *linear algebraic equations*. The main objective of the discretization is to utilize the computational abilities of modern hardwares to solve the governing global equation of the problem – naturally a *partial differential equation*. It is one of the most used and most important engineering analysis methods[†], as the elements can be used to discretize the shape of products, structures and prototypes, simulating local stresses, temperatures and strains. This greatly facilitates design processes to reduce negative effects of trial and error approaches in design, or from the impossibility of obtaining analytical solutions to a determined problem [40].

Figure 9 presents modern photomicrographs of chip sections of a 4340 steel as obtained by the experiments of Arrazola et al. [41] with varying λ and the *quick-stop* method and the corresponding finite element simulations produced by the author in the conditions of (a) $\lambda = +6°$ and (b) $\lambda = -6°$, illustrating the ability of finite element models in describing chip formation features such as primary and secondary shear zones, segmentation caused by elastoplastic instability and fracture in the free surface. Simulation by the finite element methods are a reliable way of validating results obtained by dynamometry and micrographic analysis.

---

[*]Modern reformulations of *newtonian* mechanics — *Lagrangian* in 1788 and *Hamiltonian* in 1833 were extremely important to the development of variational methods for the solution of complex dynamical systems described by *differential equations*, such as those produced by the finite element method [36]

[†]Not only engineering, but even works in the field of medicine, biology and geology have utilized finite elements in the study of related problems. This is so because *partial differential equations* are very successful in the mathematical description of natural phenomena (see, *e.g.*, [37], [38] and [39])
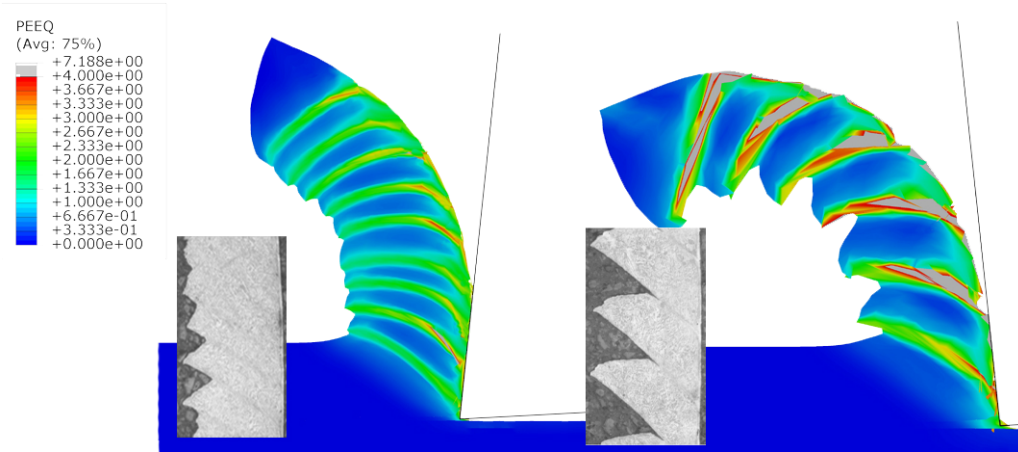
Figure 9 – Experimental obtained and simulated sections of chips produced by orthogonal cutting with varying rake angle: (a) $+6°$ and (b) $-6°$, field variable is PEEQ (equivalent plastic deformation). *Source* of simulations: author; *Source* of the photomicrographs: [41]

Variational methods were already applied to modelling of machining processes in the 60s and 70s to obtain theoretical cutting temperature [42], the presence of *built-up edge* [43] and the cutting forces [44] by finite differences in discrete elements or by relaxing iterative methods. It is not objective of this work to study the theory of numerical solution of differential equations. However, the understanding of the variables, approximations, limitations and mathematical formulation of finite element methods to study physical phenomena is necessary, since the accuracy of the studied model depends on the mathematical description of elastoplastic, thermal and contact properties. Subsection 1.5 will attempt to explain, in a brief manner, the fundamental principles and the general theory of finite elements, its advantages, disadvantages and the applicability to study the chip formation mechanism. In the following section, the way on which the stress is computed and characterized according to *continuum mechanics* will be presented, as well as the major properties of the *Cauchy* stress tensor that will be fundamental to the development of the damage evolution model present in Section 1.6.

1.3 CHARACTERIZATION OF STRESS

Stress is the physical quantity that characterizes internal forces exerted by the constituent atoms or molecules of a body when subjected to a change of the equilibrium position. The characterization of the stress state of solid materials subjected to external forces is fundamental for the understanding of the events that follow this phenomenon – namely *plasticity* and *fracture*. Stresses present in a material point contained in a three-dimensional space can be fully represented as a second order tensor, known as the *Cauchy* tensor.

1.3.1 Stress tensor

As stress is the definition of a force acting across a surface, Cauchy realized that the stress quantity can vary infinitely with any plane chosen as the reference plane. However, when described with regards to three planes – in the corresponding three-dimensional space – the stress on a material point can be fully described, independently of the adopted rotational reference, as long as the planes are perpendicular to each other. Hence, the dimension of the stress tensor is 3x3 with the 9 components σ_{ij} that completely define the stress state of a material point in a deformed configuration. The dimensions of stress are therefore force across area (in the International Unit System, IUS, $\mathrm{N\,m^{-2}}$). The tensor components are product of a *traction* vector, $\mathbf{T}_j^{(n)}$ with an unit length direction vector $\mathbf{n}_i$ perpendicular to a imaginary surface, in a way that

$$\mathbf{T}_j^{(n)} = \sigma_{ij}\mathbf{n}_i,$$

where $i, j = 1, 2, 3$, therefore

$$\sigma = \begin{pmatrix} \sigma_{11} & \sigma_{12} & \sigma_{13} \\ \sigma_{21} & \sigma_{22} & \sigma_{23} \\ \sigma_{31} & \sigma_{32} & \sigma_{33} \end{pmatrix} = \begin{pmatrix} \sigma_1 & \tau_{12} & \tau_{13} \\ \tau_{21} & \sigma_2 & \tau_{23} \\ \tau_{31} & \tau_{32} & \sigma_3 \end{pmatrix}. \tag{13}$$

Each traction vector can be decomposed into a normal and two shear stress components in a Cartesian coordinate system, as associated with a single plane. The result of these decompositions is the Cauchy stress tensor. A visual illustration of the vector, planes and resultant Cauchy stress tensor are presented in Figure 10.

1.3.2 Invariants of the stress tensor

According to Swiss philosopher Bonsack [46] mathematical entities known as *invariants* can be utilized as a metaphysically neutral criterion of physical reality. Mostly, in conventional mathematical and engineering problems, given an algebraic entity, we calculate invariants from itself and its components. However, algebraic entities can only
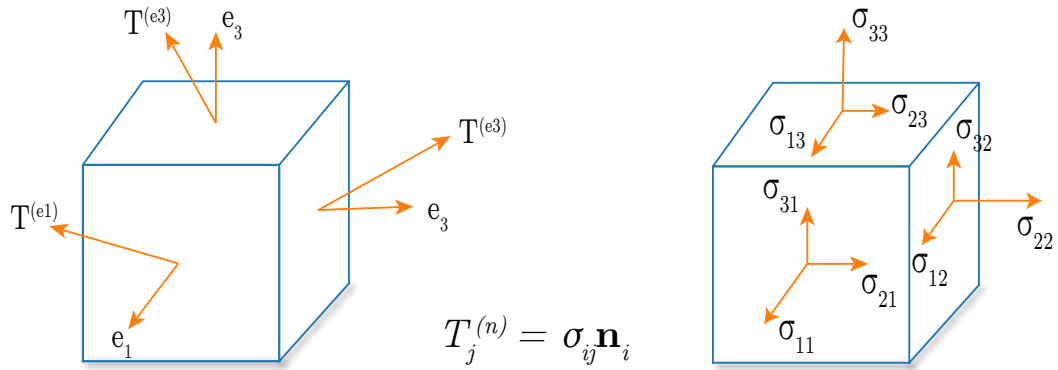
Figure 10 – Transformation of traction vectors $\mathbf{T}_j^{(n)}$ in coordinate stresses, as Cauchy components. *Source*: adapted from [45]

be possible to measure according to its *invariants*, *i.e.*, properties that are independent of transformations, operations or arbitrarily chosen coordinate system. Invariants are, therefore, *real* mathematical entities, or *observables* of a physical system.

Vector quantities, for instance, contain invariants known as direction and "length", which are independent of coordinate system transformations. Similarly, the Cauchy stress tensor has three principal invariants that are independent of transformation or arbitrarily chosen coordinate systems. These are known as rotational invariants:

$$I_1 = \sigma_{kk} = \text{tr}(\sigma),$$

$$I_2 = \frac{1}{2}(\sigma_{ii}\sigma_{jj} + \sigma_{ij}\sigma_{ji}) = \frac{1}{2}\left[(\text{tr}(\sigma))^2 - \text{tr}(\sigma^2)\right], \tag{14}$$

$$I_3 = \det(\sigma_{ij}) = \det(\sigma).$$

One of the most important invariants computed from these invariants is the *pressure*, $\mathbf{p}$, or mean principal stress, σ_m, which is the average of the principal stresses:

$$-\mathbf{p} = \sigma_m = \frac{\sigma_{11} + \sigma_{22} + \sigma_{33}}{3} = \frac{I_1}{3}. \tag{15}$$

1.3.3 Stress deviator tensor

One of the most important ideas for the modern theories of plasticity is the fact that hydrostatic stresses are negligible[*] when it comes to plastic strength[†]. The rigorous

---

[*]There is an interesting critique of the amount of the *negligibleness* of the hydrostatic stresses in flow stress, developed by Bai; Wierzbicki [47], from which this work is based on, but rather with regards to fracture

[†]Tresca, in 1869[48] already noted the fact that ductile materials never "fail" with normal strains, *i.e.*, the material fails strictly in shear with regards to normal stresses, with virtually no volume alteration across the strain path

approach of the 1913 von Mises article[*] gave rise to a new algebraic entity – fundamental to the modern plasticity theories – that represents the "independence" of hydrostatic stresses in plastic deformation, known as the stress deviator tensor.

By separating the contribution of the stresses that would generate – for a compressive body – an increase or decrease of volume without a change in shape, such as:

$$\sigma_{ij} = \underbrace{s_{ij}}_{deviator} + \underbrace{p\,\delta_{ij}}_{hydrostatic} \,, \tag{16}$$

on which the s expresses the component of the stress tensor that is responsible for the shape deviation of the material point,

$$s = \begin{pmatrix} \sigma_{11} - \mathbf{p} & \sigma_{12} & \sigma_{13} \\ \sigma_{21} & \sigma_{22} - \mathbf{p} & \sigma_{23} \\ \sigma_{31} & \sigma_{32} & \sigma_{33} - \mathbf{p} \end{pmatrix}. \tag{17}$$

Similarly as the stress tensor, the deviator tensor also has related invariants of extreme importance to plasticity and fracture theories. They are defined according to the deviator tensor s and the principal invariants of σ, respectively:

$$J_1 = s_{kk} = 0,$$

$$J_2 = \frac{1}{2}\mathrm{tr}(s^2)$$
$$= \frac{1}{3}I_1^2 - I_2, \tag{18}$$

$$J_3 = \frac{1}{3}\mathrm{tr}(s^3)$$
$$= \frac{2}{27}I_1^3 - \frac{1}{3}I_1 I_2 + I_3.$$

The J_2 invariant is the invariant utilized in the von Mises yield criterion that states that the yielding of a ductile material begins when J_2 reaches a critical value. In modern damage and ductile fracture theories, the most important variables used to determine the influence of the stress state in plastic deformation and fracture are principal mean stress σ_m and the equivalent von Mises stress σ_v . Both values were

---

[*]MISES, R v. Mechanik Der Festen Körper Im Plastisch-Deformablen Zustand. **Nachrichten von der Gesellschaft der Wissenschaften zu Göttingen, Mathematisch-Physikalische Klasse**, v. 1913, p. 582–592, 1913

thought to sufficiently describe the effect of the stress field in damage models. While σ_v defines the magnitude of stresses applied, the σ_m defines the compression condition of the surrounding material in the deformation zones and hence, the fracture restraining forces. However these variables can't describe an essential characteristic of deformation: the difference between tensile and compressive strains. This difference is best described as the macroscopic direction on which the deviation occurs inside the material: it can even tend to approximate or separate atoms from each other, independently of the restriction caused by the external environment or the material itself.

Although σ_m is capable of partially differentiating compressive and tractive environments, the difference is not clear enough with regards to the loading type. In a *reductio ad absurdum* argument, the qualitative characteristic of σ_m is illustrated by analyzing the results of Bridgman (1952)[50] and Shaw (1980)[18] in tensile and shearing tests, on which the testing pressures reached 4500 and 500 MPa, respectively. The tensile and shearing tests, even though naturally characteristic with regards to loading type, were highly compressive with regards to triaxiality. The only entity that can explicit the fundamental difference between tension and compression, *i.e.*, the resultant direction of approximation or separation of the material point itself in conditions of deviation is the third invariant of the stress deviator, J_3, which presents positive values in traction and negative in compression, independently of σ_m.

Although not possessing practical value by itself, the invariant can be used to define inside a cylindrical system of coordinates (ξ, ρ, θ) – a space known as the *Haigh-Westergaard*[*] stress space – an angle known as *Lode* angle[†], or deviatoric polar angle, θ_c. Figure 11 presents the *Haigh-Westergaard* stress space, its coordinates, the position of the Lode angle, the hydrostatic and projected stress axes in the yield surfaces, contained in a plane perpendicular to the former, known as the π plane.

The definition of a polar angle depends on an arbitrary relation to the π plane. In this work, the Lode angle will be defined in the positive cosine, on which $\pi/6$ and $\pi/2$ and corresponding to the projected axes σ_{2p} and σ_{3p} are the angles that define a triaxial shear stress. Normalizing the value of the θ_c to correspond with +1 value for traction, -1 for compression, we define the Lode *parameter*, μ.

---

[*]In honor of the engineers Bernard P. Haigh [51] and Harold M. Westergaard [51], who developed a vast amount of work on stress space and plasticity theory of metallic materials.

[†]In honor of Dr. Walter Lode by his works on the influence of the mean principal stress, σ_m in the plasticity of ductile materials
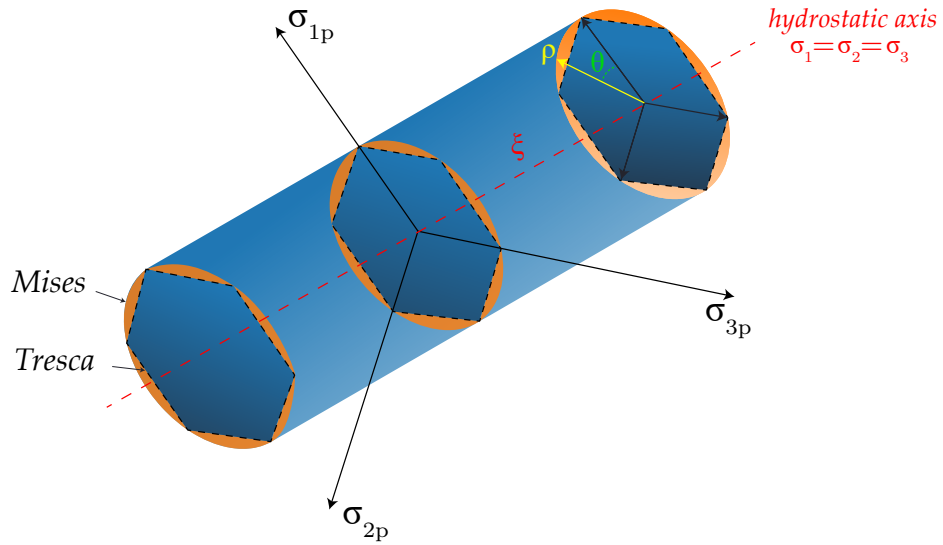
Figure 11 – Haigh–Westergaard stress space described by invariant cylindrical coordinates (ξ, ρ, θ), with Tresca and Mises yield surfaces, position of the *Lode* angle θ_c and the hydrostatic axis. The σ_{1_p},σ_{2_p} and σ_{3_p} axes are the projected σ_1, σ_2 and σ_3 axes on the yield surface. *Source*: the author

$$\mu = \cos(3\theta_c) = \frac{3\sqrt{3}}{2} \frac{J_3}{J_2^{3/2}} = \left(\frac{r}{\bar{\sigma}}\right)^3,$$

where, $\qquad\qquad\qquad$ (19)

$$r = \sqrt[3]{\frac{27}{2} J_3}.$$

Figure 12 presents the π plane with the projected axes and the Lode angle, θ_c
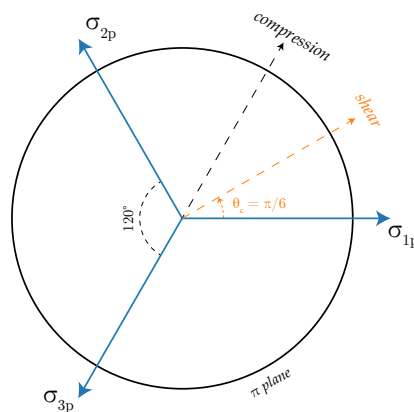
Figure 12 – The π plane with the projected axes, σ_{1p},σ_{2p} and σ_{3p}, the Lode angle, θ_c and the triaxial compression and shearing positions

1.4 BEHAVIOR OF METALLIC MATERIALS UNDER MACHINING CONDITIONS

It is of fundamental importance to utilize constitutive equations that identifies and accurately predicts the response of different materials to external phenomena for mathematical modelling – such as in the case of finite element modelling – in order to describe the mechanical conditions on which the chip is formed. These phenomena can be separated into four with regards to its nature:

(1) elastic

(2) plastic

(3) fracture

(4) friction

The first item defines rigidity of the solid and its deformations in a stressed condition. The second defines yielding, or permanent deformation resulting from the solid body when stressed upon a certain critical stress. The third defines the limit on which the body can be deformed without the disruption of the plastic flow and how this disruption evolves with time. The fourth is related to tribological properties between the pair and when subjected to relative motion.

The first three items can be illustrated and separated in a very familiar representation to engineers and material scientists: the stress $\times$ strain curve. Figure 13 presents an example of this curve, separating, illustratively, the three first phenomena previously described:

Each phenomenon has to be modeled, by means of mathematical equations, with the finality of accurately representing satisfactory results of cutting forces and real machining conditions. The modelling method will be described with rigor in subsection 1.5. However, it is worthy to mention some important aspects of Figure 13.

The green region can be modeled from purely physical considerations. For isotropic materials, with only two properties: the Young's Modulus E and the *Poisson* coefficient ν. The yellow region is modeled with more approximations, as it will be explained in Section 1.4.2, the plastic deformation effects on the properties of the solid are too complex to be modeled in macroscopic configurations from physical/*ab initio* considerations, as it depends on dislocation density and its elastic interactions, non-conservative motions with regards to temperature and the resultant stress fields. The macroscopic parabolic approximations, though, can be satisfactory with regards to experimental results. The orange region is fracture, and is overlapping the plasticity
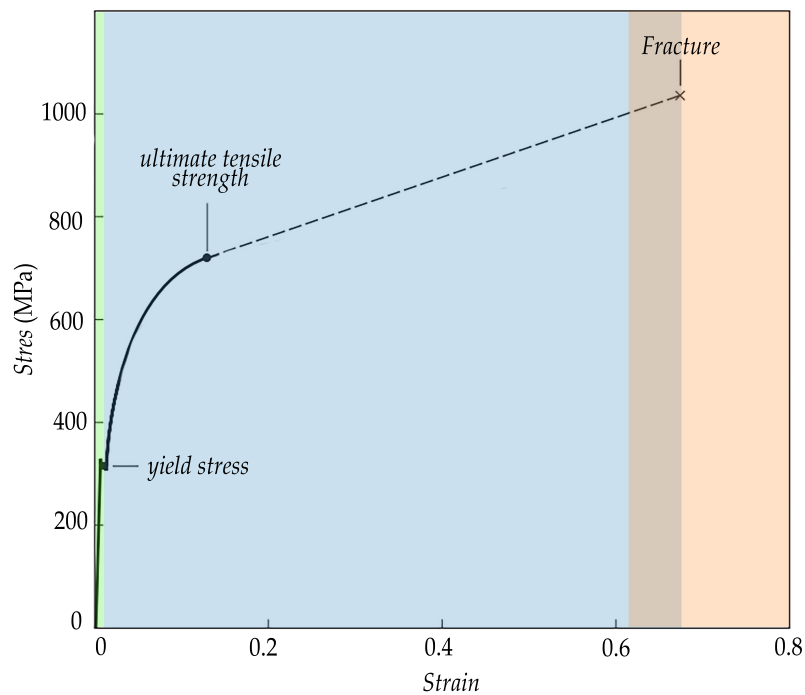
Figure 13 – Stress-strain curve for a hot-rolled 4140 steel illustrating 3 phenomena: elastic (green), plastic (yellow) and fracture(red). *Source*: adapted from [52]

region, this is explained once the fracture characteristics in ductile materials is resultant from the progressive damage along the strain path – this phenomena will be better explained in Section 1.4.3.

1.4.1 Elasticity

Elasticity, in mild terms, deals with stress and subsequent instantaneous desformations. It's necessary to separate, in an useful manner, the way on which we define elastic phenomena when dealing with metallic materials – macro and micromechanically. The first deals with the elastic fields produced by dislocations inside a crystal body or defects and their interaction during plastic deformation, the second one defines the rigidity of the body when subjected to different conditions of mechanical requirement, which as experimental evidences suggests, in engineering terms [52], is virtually independent of the former. This subsection will deal with the latter phenomenon, which we can measure directly from the stress strain curve – which is mostly dependent on physical and crystallographic considerations far beyond the scope of this work – and its effect on directing the work done during machining operations.

The first correct definition of the elastic problem was given by Hooke, *ut tensio sic vis** [53], is the major historical milestone on constitutive equations, as defined the linear elastic character of most solid bodies. With a great repertoire of experiments with

---

*with the extension, the force

different materials: wood, glasses and metallic springs, Hooke unveiled a fundamental characteristic of solid bodies: the capacity of the body to dislocate from its original equilibrium position, and the strength necessary to do so [54].

The Hooke's law, in a more rigorous definition, is given by [55]:

$$\sigma_{ij} = C_{ijkl}\,\varepsilon_{kl}, \tag{20}$$

$$\varepsilon_{ij} = S_{ijkl}\,\sigma_{kl}, \tag{21}$$

where C_{ijkl} and S_{ijkl} are the elastic constants of the crystal structure. In most metallic materials, the elastic modulus is measured in terms of the Young's modulus, E, and shear modulus, G. As most metallic materials are cubic, these moduli can be defined for any crystallographic direction $[ijk]$, according to the equations [56]:

$$\frac{1}{E_{ijk}} = S_{11} - 2[(S_{11} - S_{12}) - \frac{1}{2}S_{44}] \times (l_{i1}^2\, l_{j2}^2 + l_{j2}^2\, l_{k3}^2 + l_{i1}^2\, l_{k3}^2), \tag{22}$$

$$\frac{1}{G_{ijk}} = S_{44} + 4[(S_{11} - S_{12}) - \frac{1}{2}S_{44}] \times (l_{i1}^2\, l_{j2}^2 + l_{j2}^2\, l_{k3}^2 + l_{i1}^2\, l_{k3}^2). \tag{23}$$

Where E_{ijk} and G_{ijk} are the Young's and shear moduli, respectively, in the direction $[ijk]$, on which l_{i1}, l_{j2} e l_{k3} are the directional cosines of the $[ijk]$ direction.

Equations 20, 21, 22 and 23 bring two important notions: the scalar parameter E, known as Young's or elastic modulus, that defines the relation between stress and strain in the elastic regime and the existence of fundamental property variation with regards to direction of mechanical requirement.

The measurable property in an uniaxial tensile test of a polycrystalline metal is the Young's modulus[*] E, which is related to the elastic constants and to the Poisson coefficient ν according to: [†].

---

[*]We consider isotropy in polycrystalline samples, with the exception of those with strong crystallographic texture (such as those resulted from high deformation processes, *e.g.,* rolling, drawing, etc.), due to the somewhat random orientation of the crystals inside the polycrystalline solid, eliminating the macroscopic effects of anisotropy

[†]The Poisson coefficient is the negative ratio of the transversal and axial deformation, $\nu = -\frac{\varepsilon_{11}}{\varepsilon_{22}}$, and is a fundamental material property – it varies in most cases from 0 to 0.5, *e.g.,* rubbers presents values next to 0.5, metals between 0.21 and 0.30, however some biological (such as cartilage or corneæ) and synthetic materials can present zero or even negative Poisson coefficients [52]

$$
\begin{pmatrix} \sigma_x \\ \sigma_y \\ \sigma_z \\ \tau_{yz} \\ \tau_{xz} \\ \tau_{xy} \end{pmatrix} = \frac{E}{(1+\nu)(1-2\nu)} \begin{pmatrix} 1-\nu & \nu & \nu & 0 & 0 & 0 \\ \nu & 1-\nu & \nu & 0 & 0 & 0 \\ \nu & \nu & 1-\nu & 0 & 0 & 0 \\ 0 & 0 & 0 & \frac{1-2\nu}{2} & 0 & 0 \\ 0 & 0 & 0 & 0 & \frac{1-2\nu}{2} & 0 \\ 0 & 0 & 0 & 0 & 0 & \frac{1-2\nu}{2} \end{pmatrix} \begin{pmatrix} \varepsilon_x \\ \varepsilon_y \\ \varepsilon_z \\ 2\gamma_{yz} \\ 2\gamma_{xz} \\ 2\gamma_{xy} \end{pmatrix}. \quad (24)
$$

Where τ and γ are tensile and shear deformations, respectively.

1.4.2 Plasticity

As earlier explained, metal crystals deform by the slipping of the most densely packed crystallographic planes. Schmid and Boas [56] in the seminal work *kristallplastizität*, determined what would be the nature of metal plasticity. Briefly, the rules are [57]:

- the plastic flow begins when the resolved shear stress* on a possible slip system reaches an "unique" CRSS value

- the CRSS value is not affected by other stress components except the one along the Burgers' vector, *i.e.,* glide shear stress

In 1926, *Frenkel* [58] calculated the theoretical shear strength of metallic materials by considering rows of atoms separated by a distance A under a shear stress. The results from his calculations were apparently incoherent: the theory generated strength values up to three orders of magnitude greater than the experimental results. The historical context of the calculation was not a mere coincidence, once that it was already part of an extensive work of the decade to understand the role of crystallinity and elasticity on the widely known results obtained from 1899 and 1900 in Ewin's and Rosehain's works [59, 60], that demonstrated that the plastic deformation in single crystals formed micro-*steps* in the surface of deformed metallic crystals.

Although the importance of the dislocation theory for the development and understanding of plasticity theory, it is not within the scope of this work to describe the plastic deformation in these terms, but rather to describe the mechanical and micrographic phenomena produced by the severe plastic deformation in machining processes (with allegedly $\varepsilon = 10 - 50$) according to Trent; Wright [2]. For this, we will describe the

---

*The resolved shear stress τ_R is the acting shear stress due to a certain directional applied stress σ, as calculated by $\tau_R = \sigma \cos \lambda \cos \phi$, where λ and ϕ are the angles between the stress and the slip direction, and the stress and the normal of the plane

major strain hardening theories of metallic materials and correlated effects, to justify the author's choices with regards to modelling to be described in the Section 1.5.

In intermediate strain regimes, specially in materials with low SFE or reduced slip mechanisms[*], strain generates slipping of specific crystal planes ny the simultaneous movement of thousands of dislocations in restrict regions inside the grain, the regions of intense dislocation slip are known as shear bands. The phenomenon is illustrated in Figure 14 (a). It has been observed that even in materials with poor thermal properties, like Ti-6Al-4V, chip segmentation is often followed by elongated dimple-like features in the free surface of the segments, while the bulk of the chip presents little to no evidence of material separation [61]. This provides further evidence of fracture induced segmentation with initiation in the free surface, rather than adiabatic shear banding. Shaw [5], mentions that thermal softening ought to occur only on extensions of the shear fracture, and should be impossible to predict segmentation purely with thermal assumptions.
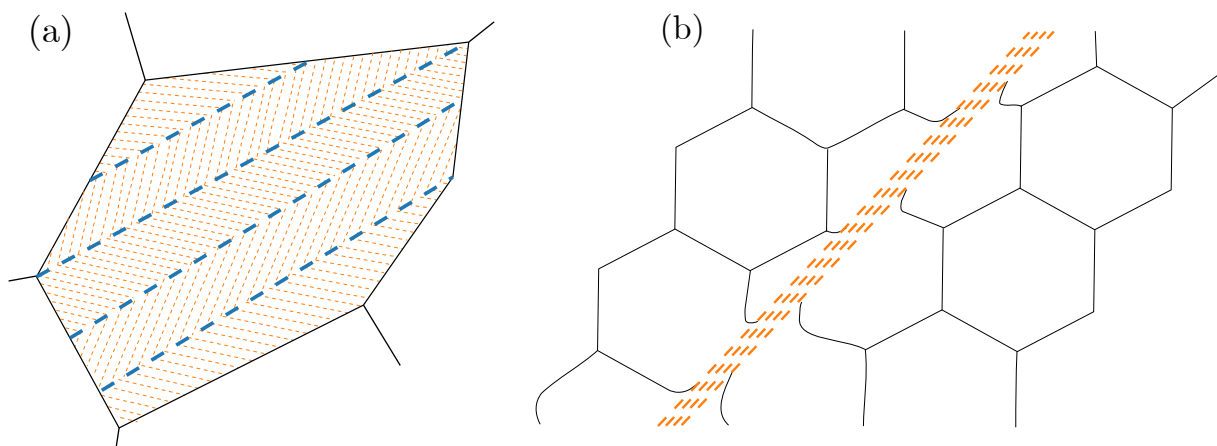
Figure 14 – (a) slip bands - - - inside a deformed grain (b) shear band - - - crossing the microstructure. *Source*: the author

In severe deformation regimes, specially in materials with low SFE, strains can concentrate in very narrow regions not restricted to crystallographic orientation, across numerous grains. This phenomenon is mostly present in very high strain conditions, with high strain rate or even with high temperature deformations, and is characterized by a local decrease in strength. Hence, shear bands are characterized as a *softening* process. While the root causes of shear banding had been a subject of intense debate, the *softening* effect is believed to be caused by stress concentration due to missing a favorable slip mechanism with respect to macroscopic stress and hence nucleation of dislocation in adjacent regions, favoring the localization of strain [62]. Shear bands are regions of very high dislocation density, twinning and normally associated with regions

---

[*]Von Mises criteria for ductile material states that is necessary, for a crystal aggregate, at least 5 independent slip systems in order to accommodate an arbitrary plastic deformation, and hence, present a considerable ductility.

with initial phenomena of recovery and recrystallization, due to high temperature. Figure 14(b) illustrates a generic micrographic aspect of shear bands.

Shear bands are the most visible aspect of plastic deformation in machining. In fact, segmented chip formation as presented in Figure 7 and even in continuous chips with surface roughness, the shear banding is the dominant aspect of chip formation. While shear banding is known since Tresca, the nature of the shear banding root cause remains mostly unknown [63]. Strong correlation with *hardness* was already pointed out by Pursche; Meyer, Dodd; Bai [64, 63]. Furthermore, in these studies, no clear correlation between softening and the initiation of adiabatic shear banding was found. Higher strength steels in higher temperature presented a higher tendency towards *adiabatic* shear banding. Medyanik; Liu; Li [65] and Schoenfeld; Wright [66] pointed out the necessity for a ductile damage evaluation of *adiabatic* shear banding, as a multi-physics approach. Which, in effect, is a critique of the *sola thermica* considerations of adiabatic shear banding models.

Chip segmentation, in certain alloys and/or conditions, is an exclusive phenomenon of higher cutting speeds, such as in cutting of titanium alloys [67]. This was initially used as an argument for the treatment of segmentation as a thermoplastic instability rather than a fracture phenomenon [68]. Nevertheless, in apparently continuous chips, it can be shown that segmentation and flow localization is still present, as shown by the results of Guo; Compton; Chandrasekar [33], this is believed to be caused by the decrease of the shear plane length when fracture initiate and grow in the free surface, denominated geometrical softening, contributing to flow localization [33]. The effect of hydrostatic stresses on the free surface roughness during the formation of continuous-like chips was already pointed out by Shaw [5]. The evidence of flow disruption even in apparently continuous chips, as those presented in the works of Guo; Compton; Chandrasekar [33], provides further evidence for a fracture initiated phenomenon, rather than a thermal one.

1.4.3 Fracture

A milestone of chip segmentation theory through fracture mechanics was introduced by Mabrouki et al. [32]: Hillerborg's critical energy release rate G_f. This parameter was computed from a mixed fracture toughness parameter through K_{IC} and K_{IIC}, and was used to predict the evolution of fracture after the onset of damage of the elements in the finite element model. Although resulting in a reasonably good prediction of chip morphology and cutting forces, the fact that the ductile shear fracture is initialized at the tool tip rather than in the free surface results in an unrealistic approximation to experimental evidence [27, 33]. Also, the model fails to predict segmentation dependence on depth of cut as presented in [69] or the presence and variation of chip free surface

Mode I
opening

Mode II
shearing

Mode III
tearing
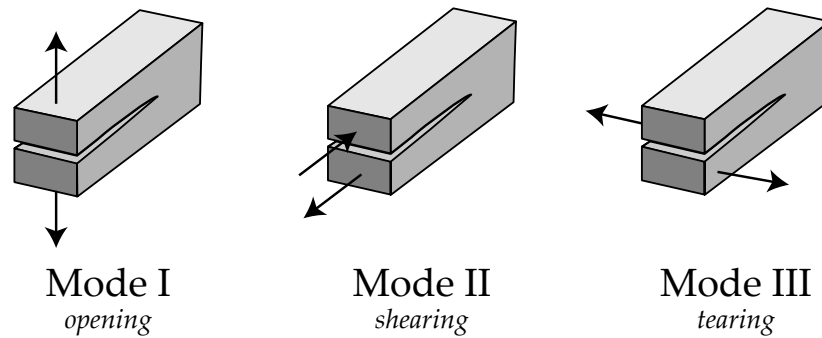
Figure 15 – fracture modes for critical stress intensity factors. *Source*: the author

roughness.

In the work of Razanica et al. [70], the damage evolution law during machining was based on a time dependent viscoplastic Bingham-type model with a constant fracture energy release rate for the dissipation of the plastic components, based solely on the principal stresses for determination of the fracture threshold. The Cockcroft-Latham ductile failure criterion is an early attempt to differentiate the effects of the normal stresses on the amount of plastic work per unit volume that can be performed by the material [71].

Fracture by tensile straining of ductile engineering alloys in regular tensile testing conditions is well known to be caused by void growth and coalescence, and a cup and cone fracture morphology in the macroscopic scale [72].

The macroscopic morphology is explained by the local dominating stress/strain state; a tensile-mode I crack is present at the center of the specimen, where tensile stress conditions dominate, whilst a mixed mode I and II fracture is present at the edges of the sample, where shear stress conditions are approached [52]*

The loading type of critical stress intensity factors determine the type of property. K_{IC} refers to the critical stress intensity factor in a mode I loading type, and so on. The loading types are illustrated in Figure 15.

The voids may nucleate inside a crystal due to differential lattice rotation and/or twinning, in grain boundaries, due to plastic incompatibility between neighboring grains, and in interfaces of rigid inclusions [52] during plastic deformation. As plastic deformation continues, these voids grow larger, and their growth rate is dependent on the stress state of the constraining material, defined by the competition between the growth caused by straining and hydrostatic stresses produced by the surrounding material [73].

Once voids begin to grow and coalesce, the material is considered damaged

---

*it is necessary, though, to state that the *mode I* and *II*, in this case, refers to the loading mode - tensile or shearing, not to the plane condition of stresses – plane *stress* and plane *strain*

and the bulk loses its stiffness and strength due to the increasing volume fraction of voids, in competition to the strain hardening of the remaining material [74]. The connection between ductile damage and chip segmentation arises from the periodic formation of damaged zones as the chip is being produced, as proposed by Sowerby; Chandrasekaran [75].

1.4.3.1 Fracture characteristics of intermetallic Fe₃Al

Fracture of intermetallic materials is one of the main reasons for the limited large scale and widespread applicability of these materials, the presence of complex crystal structures in this type of materials results in a group on which the majority of the candidates present virtually no ductility due to the inability to comply with the Mises criteria for ductile materials – the need of 5 independent slip systems. In the case of Iron Aluminide, the $D0_3$ and B_2 are cubic which would render higher ductility than most candidates. Even so, these alloys present, in ambient condition, a maximum of 2% tensile strain before brittle cleavage fracture [76]. In the case of Fe3Al, von Mises criteria is just one of many needed factors to produce necessary ductility There are still factors which contribute to brittleness, such as air moisture.

In tensile testing, the ductility difference between testing in atmospheric, moist conditions with pure oxygen is almost sevenfold (from 2% to 17% in both FeAl and Fe₃Al cases) [77]. The environment effect is related to the reduction of water molecules present in moist environment during oxidation of the newly formed surface during deformation [78]:

$$2Al + 3H_2O \rightarrow Al_2O_3 + 6H^+ + 6e^-. \tag{25}$$
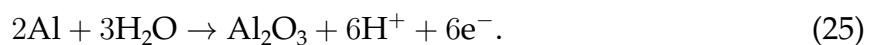
Part of the atomic H_{ads} (adsorbed) will be absorbed by the metallic structure, and allocated, according to DFT (*Density Functional Theory*) calculations, in the regions close to tetrahedral interstitial sites of the Fe₃Al crystal [79]. According to results obtained with ECNI (*Electrochemical Nanoindentation*) [80], atomic hydrogen is responsible to:

(a) reduction of shear strength caused by softening of atomic bonding inside the crystal

(b) reduction of the energy needed for dislocation nucleation

(c) reduction of dislocation mobility

All these factors are determinant to the embrittlement of a ductile metallic material.

Fracture of Fe_3Al and FeAl in environmental conditions is characterized by long and shiny transgranular cleavages. With additions of chromium, the increase in ductility is accompanied by characteristic mixed inter-transgranular cleavage fracture [81]. When tested in dry oxygen environments, fracture rises fibrous tearing within surfaces and ductile fractographic features emerge, along with an increase in ductility [82, 78, 83]. In ordinary machining conditions, the chip formation mode is ductile, as shown in Figure 16, this indicates that under compressive, with very low triaxiality, under high cutting speeds we can make use of ductile damage models to describe fracture of Fe_3Al under machining conditions. Figure 17 presents the characteristics of these three fractures under tensile strains.
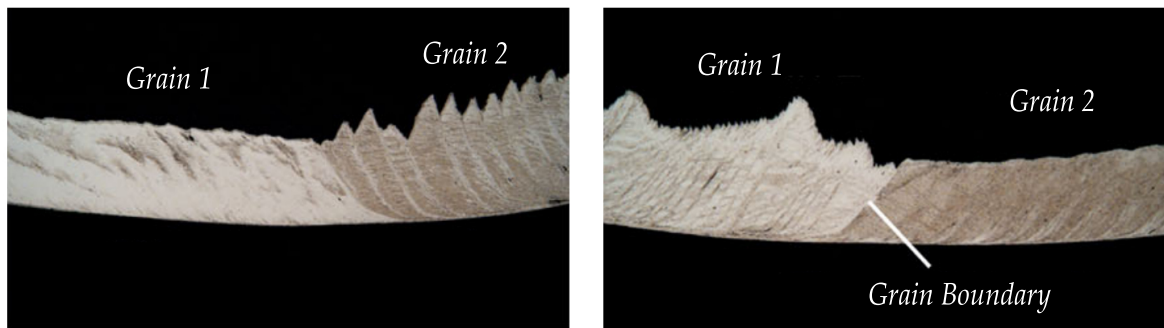
Figure 16 – Change in the chip formation mechanism with grain orientation during machining of an Fe_3Al alloy. *Source*: [84]

As a material with very limited (but present) ductility, we can characterize a stress intensity factor to predict the stress intensity (the scaling intensity of stress) near the tip of the crack for Fe_3Al alloys. The toughness of a material can be described in terms of which stress intensity is necessary for a sharp crack to become rapid and catastrophic. Under plane strain conditions, this is called the critical stress intensity
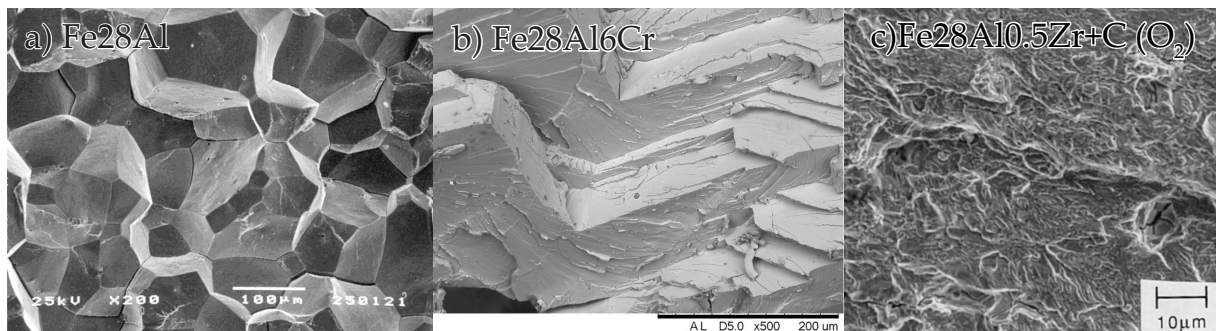
Figure 17 – Three different fractographic morphologies for iron aluminides, a) and b) were tested under normal environment conditions. Alloy c) was tested in oxygen gas. Increasing evident faceting and fibrillation is seen from b) to c). *Sources*: a)[85] b)[86], c)[83]

factor $(K_C)^*$ and it is a specific material property.

1.4.4 Friction

We previously defined the friction force acting on the shear plane, a friction coefficient based on the orthogonal cutting model and Coulomb friction law (μ_f) from the F_c and F_p cutting forces. By definition, it is a force that resists the relative motion between two surfaces in contact. What remains to address is the nature of this friction and the effects of surface properties. The proportionality of Coulomb law $F = \mu N$, comes from the fact that real solid surfaces are not completely flat, and hence only the top of the hills of the surfaces touch each other. If the contact area is infinitely small, we can imagine that the mean stress acting on the real contact area is equal to the yield stress of the material. The material then deforms plastically, increasing the contact area, while atoms become closer and closer. If the surface is close enough, bonding (or welding) occurs, but since these materials are identical, the mean stress of the region of the contact area remains the same – this approximates the Coulomb proportionality to most engineering sliding solutions, where the contact area is very small [2].

In metal cutting, however, dissimilar materials are used, on which the cutting tool is much higher than the material being cut. When two materials of different flow stress are in contact, the force required to move one body over another becomes independent of normal stresses, since the contact area is mostly always total. This is what causes the condition of seizure previously mentioned: the contact area becomes total in the rake face of the tool, and the material is perfectly sheared with the movement of the adjacent material. There is a chip plastic shearing component in friction that depended mostly on the regime of plastic deformation, defined by ductility, strain hardening exponent, *et cætera*. When this condition of seizure tends to infinity, in some cases, the material becomes somewhat permanently adjacent relative to material movement, creating a *built-up* edge, as previously mentioned.

While the friction forces are easy to calculate and estimate, the real phenomenon is very complex, which is intrinsically related to workpiece strength when considering empirical evidence [2]. Friction forces are inherently present in machining, and only in very specific cases friction forces can be reduced. Like in the case of grey cast iron or *free-machining* steel and brasses, on which the graphite or lead intermetallic acts as a lubricant for the machining tool.

---

*In this case, the lowest critical stress intensity factor is obtained under plane strain conditions, *i.e.*, under maximum triaxial constraint

1.4.5 Thermal effects

As illustrated in Figure 8, an increase in cutting speed leads to the reduction of cutting forces in most metal alloys. This is explained by the softening of alloys due to increase in temperature. The most important heat source in metal machining is the region of material shearing near the rake face during the condition of seizure [2].

While forces and stresses are important in metal machining, they are not the ones that limit the rate of material removal in industrial machining conditions, but temperature. An increase in temperature increases the action of the principal mechanisms responsible for tool wear, such as rake and flank wear due to diffusion or gross fracture due to temperature caused tool tip softening [2, 5].

Most models used for the simulation of cutting mechanisms use a thermal softening parameter, usch as in Johnson; Cook [87] [87] and Mirzaie; Mirzadeh; Cabrera [88] models. The thermal softening parameters will be presented in Section 1.5.

1.4.5.1 Thermal effects in intermetallic Fe3Al

An important aspect of Fe_3Al alloys is the anomalous yield behavior with temperature. While most alloys present a reduction of yield stress with temperature[*], Fe_3Al presents hardening near the $B0_3 \rightarrow D0_3$ region. The anomaly is illustrated in Figure 18 for Fe28Al with 5 at% Cr, 1 at% Nb with traces amount of B and Si (alloy 91, 92 and 85) with different previous ordering treatments in the $D0_3$ and B_2 regions.

The anomaly "*was explained in terms of the nucleation, easy glide and then high work hardening of perfect superdislocations*"[†] in the $D0_3$ lattice. The $< 111 >$ perfect superdislocation is split into two pairs of partial dislocations, with Burger's vector of $1/4 < 111 >$ and bound by anti-phase boundaries (APB). The two $1/4 < 111 >$ partials are locked by a local climb process in the temperature range of the hardening phenomena ($\approx 500°C$)[90].

If the reduction of cutting forces are mainly explained by reduction in shear strength due to temperature, then the cutting forces when machining Fe_3Al would vary less than of most metals. While Fe_3Al was in-depth studied with regards to machining conditions in [84, 91], the impact of the anomaly in the relation between cutting forces and cutting speed was not in scope, but rather the relation between temperature and crystallographic orientation. However, the cutting forces were less in the $180m\,min^{-1}$

---

[*]While some strengthening is found in some alloys due to phase transformation, such as secondary hardening in high speed steels, anomalous yield strength with no phase transformation/precipitation can only be found in intermetallic alloys

[†]MORRIS, D. G.; PEGUIRON, D.; NAZMY, M. Yield Stress and Stress Anomaly in an Fe3Al Alloy. **Philosophical Magazine A**, Taylor & Francis, v. 71, n. 2, p. 441–463, fev. 1995. ISSN 0141-8610. DOI: 10.1080/01418619508244368, p. 1.
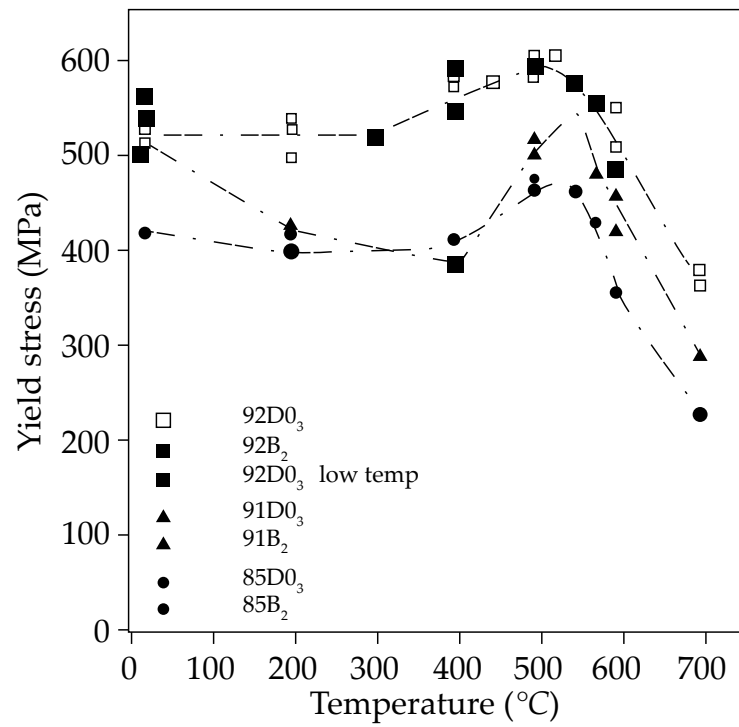
Figure 18 – Yield stress anomaly for different Fe$_3$Al-*based* alloys. *Source*: adapted from [89]

than the 60m min^{-1}, this can be attributed to the reduction in contact area between tool and workpiece [2].

1.5   THE FINITE ELEMENT METHOD

The importance of equation solving to quantify physical processes is given by the capacity of prediction the behavior of a system, given an initial or boundary condition. The behavior or a physical system, constituted of known and quantified phenomena, can be modeled with the aid of partial differential equations (PDEs), that determine the rate of change of a physical quantity with relation to another. It is the role of engineers, physicists and mathematicians to model physical phenomena in a quantifiable manner, in order to understand possibilities, limitations and capacity of the physical system to provide the needs of technology, increase productive performance in industry and to enhance our understanding of physical processes [92].

The finite element method is one of the ways to solve, numerically, PDEs by the discretization of a larger problem into smaller ones. The method is notoriously well-known due to the advantage in most dynamic, heat transfer and electromagnetic engineering problems: the spatial discretization of a component, product or structure. This body discretization allows to analyze locally all strains, temperatures, electromagnetic potentials and heat and mass flow. Hence, the finite element method became one of the most important tools in design and optimization of components in modern engineering [93]. Figure 19, presents a curved surface representing an exact analytical solution of a PDE, and its approximate solution, represented by the sum of finite plane elements, united by nodes, representing the discretization of a real domain in simple subdomains. We can observe the importance in selection of types and the quantity of elements: while more elements mean better approximation to the real solution, the computational cost increases, just as the solution completion time.
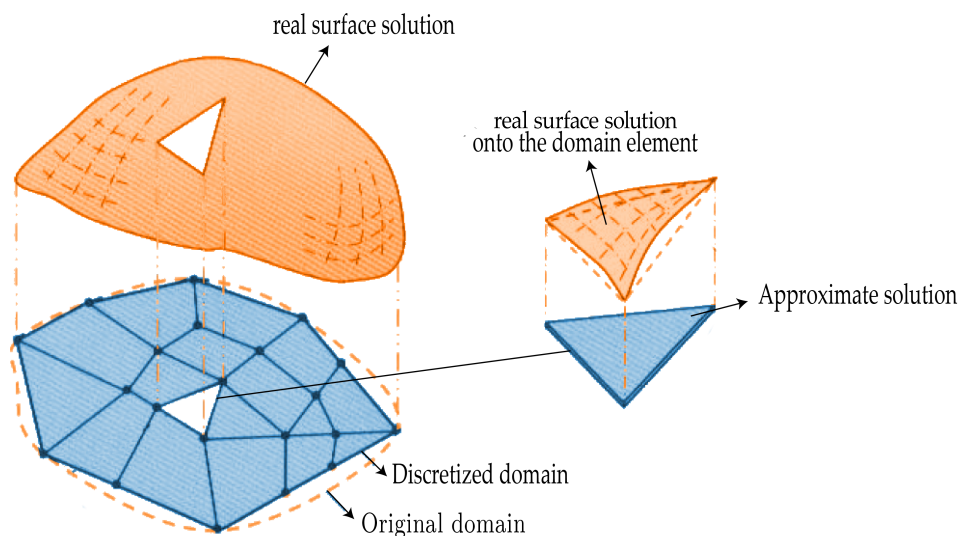
Figure 19 – Approximation of a curved surface – representing an exact analytical solution – by the discretization in subdomains of lesser complexity. *Source*: adapted from [92]

The justification of the choosing of a numerical solution rather than analytical one (as previously presented in subsections 1.2.1 and 1.2.3), is a consequence of the great difficulty or even impossibility of solving PDEs by means of mathematical manipulation, analytically. By including complexities like non-linear properties (like hardening and softening due to damage), or geometrical and structural geometries, the problem becomes impossible to be solved [93]

The finite element method consists, briefly, in the following steps [93]:

- The discretization of a domain in simpler subdomains, called finite elements, on which the totality of elements represent a finite element mesh.

- The approximation of the physical process in each finite element – produced by functions (*e.g.*, polynomials) in each node of the element, producing an algebraic equation in the form of a matrix for each element, determining displacements, strains and stresses.

- Algebraic equations are reunited and balanced with the aid of fundamental physical processes as conservation of mechanical, thermal and electromagnetic energy, minimizing a residual associated to the approximate solution or virtual work to be produced by the body *

In order to solve a differential equation, we search for the approximation $\bar{u}$ for a function u – which is an exact solution to a PDE – in the form of [93]:

$$u \approx \bar{u} = \sum_{j=1}^{m} c_j \, \phi_j,\tag{26}$$

on which c_j are undetermined coefficients, ϕ_j are the test functions. The nature of the method comes with the need of selection, the quantity and types of equation to the determination of the c_js coefficients.

In the finite element method, each element and node's algebraic equations are disposed in a matrix and solved simultaneously in order to approximate the global real solution according to boundary and continuity conditions [36], dynamical system's energy principles [35] or by reducing an $R(x)$ residual arising from the error of the weight functions as when applied as a solution to the PDE[†], the $R(x)$ residual and the weight functions w_i, according to [35]:

---

*The balancing of test functions to be applied for the approximation of the real result is due to the formulation of the PDE in its weak form – making not necessary for the results to obey the strictly imposed conditions of the PDE, but rather to an approximation based on minimization of associated residuals [35]

[†]in the Galerkin method, weight functions – responsible for the reduction of the R residual, are equivalent to the test equations ϕ_j presented in Equation 26.

$$\int_{x_0}^{x_1} R(x)\, w_i\, dx = 0 \quad \cdot \quad R(x) = \mathcal{L}\bar{u} - f, \tag{27}$$

where $\mathcal{L}$ is a differential operator, w_i is a weight function and f is a differentiable, continuous function in x.

Computational implementation for the solution of finite element problems are divided in three parts:

- preprocessing and modelling

- processing or analysis

- post processing

Thermomechanical properties, damage and plasticity constitutive equations, geometry and boundary conditions are defined in the preprocessing and modelling part, where node algebraic equations, element matrices and boundary conditions are defined [92]. In the software Abaqus - SIMULIA™, *e.g.*, preprocessing produces and .inp file which contains model informations as node and element position, element type, boundary conditions, materials and respective constitutive equations, contact properties and output requirements as equivalent stresses and strains, deformations, strain rates, damage, temperature and heat flow. Furthermore, this output is compiled and post processed for visualization [94].

The results, after iterative methods of residual reductions, when converged to a successful solution, are compiled and post processed. When these are time-dependent, they are separated in *steps*, which present a solution (scalar or vector components of stress, strain, temperature, etc.) for each element or node with time. An example of the results of post-processing was already illustrated in 6(b).

The next subsections will illustrate the steps for the modelling of a finite element model (FEM) of an orthogonal cutting process, explaining the different constitutive equations, boundary conditions, geometry and assumptions used for the model to predict, adequately, the complexities within the mechanism of chip formation of metallic materials presented in subsection 1.2.3.

1.5.1 Interaction and contact conditions

In order to simulated contact interaction between tool and workpiece, it is necessary to describe the frictional and normal stresses acting along the rake face of the
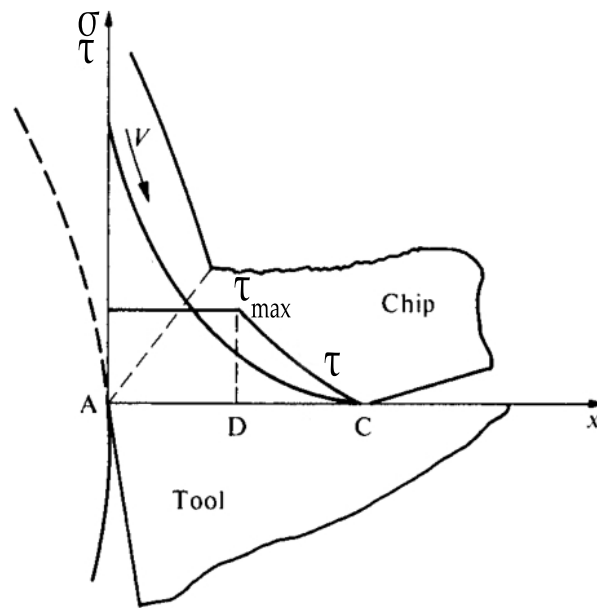
Figure 20 – Distributions of shear and normal stresses in the tool. *Source*: adapted from [5]

tool. Figure 20 presents the distributions of both stresses in the rake face of a cutting tool.

From the distributions, it is important to notice that in the regions from A to D, the normal stresses are sufficiently high to suppress microcrack formation, and shear plastic deformation dominates the chip formation mechanism. The constant shear strain is consistent with the previously defined region of *seizure*, on which the maximum shear stresses in the tool face in contact with the workpiece are determined by the strength of the workpiece material [95, 96]. Hence, the contact conditions in finite element machining is often described in terms of a maximum shear force, $\tau_{\max}$, defined in terms of the flow stress of the material, and a constant friction coefficient μ_f whenever $\tau < \tau_{\max}$.

1.5.2 Plasticity modelling

In ductile materials, elastic deformations are the only produced in a body until the plastic flow stress is reached – this stress defines a limit from which the deformations become permanent. In an uniaxial tensile test, this condition is reached when the applied stress $\sigma_{11} > \sigma_y$, where σ_y is the flow stress. In some metals, flow stress is evident, as in the stress-strain curve presented in Figure 13. However, many metals don't present a serrated flow stress or discontinuities in the region of the plastic stress [*], so the linear characteristic of the elastic stress-strain is used to define a 2% strain offset line that

---

[*]the serrated flow stress is known as the *Portevin-Le Chatelier*, the limit between elastic and plastic deformation is well-defined, and the fast sudden movement of dislocations from stress fields caused by solute atoms generate sudden flow stress drops, which appear in the stress-strain curve

follows the elastic stress and defines, in the intersection between the line and the flow curve, the flow stress of an ill-defined elastic-plastic material.

Tensile tests are important as they define the flow stress of a material, but they cannot, alone, explain the flow stress of materials in complex states of stress. For that, we define flow criteria. One of these criteria is the well-known *Von Mises* [49] criterion, which defines a stress condition for the initiation of plastic strain. Despite the importance of this criterion, it doesn't define the material's behavior after plastic strain occurs, *i.e.*, the magnitude of the hardening and the geometry of deformation. These are fundamental for modelling plasticity until fracture.

The mathematical modelling of ductile materials tries to reproduce the results illustrated in Figure 13. In order to do so, many models based on parabolic hardening were proposed. The first one was proposed by Hollomon [97],

$$\bar{\sigma}_y = K\,\varepsilon^n, \tag{28}$$

where K and n are material constants defined as the strength coefficient and hardening exponent, respectively.

Including the initial flow stress $\bar{\sigma}_{y0}$, we have the *Ludwik-Hollomon* equation:

$$\bar{\sigma}_y = \bar{\sigma}_{y0} + K\,\varepsilon^n. \tag{29}$$

Many other works, since the publication of the work of *Hollomon*, in 1945, aproximated the plastic behavior of materials with a parabolic hardening law*. The most used model for the definition of material behavior that include the contribution of strain-rate and temperature, and hence, largely used in simulation of cutting processes, is the *Johnson-Cook* [98] model, defined by:

$$\bar{\sigma}_y = \underbrace{[A + B(\bar{\varepsilon})^n]}_{\text{hardening}} \underbrace{\left[1 + C\ln\frac{\dot{\bar{\varepsilon}}}{\dot{\bar{\varepsilon}}_0}\right]}_{\substack{\text{strain} \\ \text{rate}}} \underbrace{\left[1 - \left(\frac{T - T_r}{T_m - T_r}\right)^m\right]}_{\substack{\text{thermal} \\ \text{softening}}}, \tag{30}$$

where the parameter A [MPa] and B [MPa] correspond to the value of $\bar{\sigma}_{y0}$ e K, respectively, and define a hardening due to plastic deformation. The constants C [-] and m [-] define the behavior of the material with respect to strain-rate and temperature rise, respectively. T_m [K] is the melting temperature of the material. T_r [K] e $\dot{\bar{\varepsilon}}_0$ [-] are reference values.

---

i.e., the relation $\bar{\sigma} = K\,(\varepsilon + \varepsilon_0)$, that defines the intersection of the stress-strain curve in the point of $\bar{\sigma}_{y0}$, is used in many computational simulation codes that discretize the elastic and plastic contributions, like in [47]. It is important to state that in this and the other *Hollomon* relations, the values of K and n are different and cannot be transposed

In this work, the $\left(\frac{T-T_r}{T_m-T_r}\right)^m$ term in equation 30 will be defined as the θ_m parameters, on which 0 means unaffected and 1 means completely softened.

1.5.3 Inelastic heat generation

In coupled temperature-displacement finite element simulation, the generation of heat during inelastic heat straining is usually defined in terms of a fraction of the work done by the strained material, named the Taylor-Quinney coefficient [99, 100]. In fact, less than 10% of the straining energy is stored in defects, the rest is expressed in terms of latent heat conversion [52]. The rise in temperature due to heat generation is defined as:

$$\mathrm{d}T = \frac{\beta}{\rho C_p}\bar{\sigma}_y \mathrm{d}\varepsilon,$$
(31)

where β is the Taylor-Quinney coefficient (fraction of energy converted to heat during plastic work), C_p is the heat capacity of the material. The $\bar{\sigma}_\varepsilon \mathrm{d}_y$ term defines the plastic work while the $\frac{\beta}{\rho C_p}$ term indicates the definition of temperature increase.

1.6 DAMAGE MODELS

1.6.1 Damage initiation model

While Elastic Plastic and Linear Elastic Fracture Mechanics (EPFM and LEFM) are historically connected with the description stress and strain fields around crack tips, the origin of cracks or flaws inside material volume is considered to be beyond the scope of these subjects, as to it was considered that intrinsic flaws are always somewhat always present in materials. FEM simulations are computationally limited to the scale of the element size when modelling fracture evolution during strain, so the dimple-originated fracture is often simulated by assigning a cumulative degradation variable to the volume element with *ad hoc* reduction of the element's strength through a strain path across a certain stress state, as in the cumulative damage models of Johnson; Cook [98] and Wilkins; Streit; Reaugh [101]. Although hydrostatic stress has, in most cases, negligible effect on flow stress, the strain and stress at damage initiation are mostly dependent both on this variable *i.e.*, on the dimensionless hydrostatic pressure η (also known as triaxiality) and on the Lode angle θ_c (see, for example, [102, 47]).

The triaxiality factor is defined as the ratio between the hydrostatic and von Mises equivalent stress,

$$\eta = \frac{\sigma_m}{\bar{\sigma}},$$
(32)

and is well known to be responsible for constraining the growth rate of voids [102]. The Lode angle θ_c (or the normalized, presently used, Lode parameter μ) is defined in terms of an invariant cylindrical coordinate system (in a Haigh–Westergaard stress space), (ξ, ρ, θ). A representation of the stress space, the yield surface and related variables were already presented in Figure 11

The J_2 invariant defines only shape deviation, but the J_3 invariant can point to the intrinsic difference between tension and compression in yield theories that disregard the effect of hydrostatic pressure, such as in von Mises (VN) and Tresca yield criteria. Variable μ is defined in the range of $-1 < \mu < 1$, with -1 being in the compression meridian and 1 in the traction meridian. Therefore, the Lode angle, a function of the third stress invariant, is believed to define growth characteristics of voids during material failure, as supported by substantial experimental evidence [103, 104, 105, 106].

The damage initiation criterion states that the plastic strain at the onset of ductile failure ($\epsilon_D(\eta, \mu, \dot{\bar{\epsilon}})$) is a function of the stress triaxiality, Lode parameter and equivalent plastic strain rate [98, 47]. Hence, the following expression for the monotonic increasing damage initiation variable for the element, ω_F is defined:

$$\omega_F = \sum_{i=0}^{n} \frac{\mathrm{d}\bar{\epsilon}_i}{\epsilon_{D\,i}}, \tag{33}$$

where $\mathrm{d}\bar{\epsilon}$ is the strain increment, i is the time step and n is the time step when the damage initiation criterion is met, which in turn is when $\omega_F = 1$. The plastic strain to failure, $\epsilon_D(\eta, \mu, \dot{\bar{\epsilon}})$, can be represented by a material-characteristic fracture surface locus. An example of a damage initiation locus is presented in Figure 21.

After the damage initiation criterion is met, the material is considered damaged and mechanical properties will monotonically decrease with further strain, in which experimental strain-stress relation can no longer hold. For many structural and/or mechanical applications, this criterion is sufficient to describe failure of structures and components. Nevertheless, in the case of simulation of machining processes, damage evolution must be taken into account after damage initiation in order to describe fracture phenomena during segmentation. In refs. [67] and [107], the strain to damage initiation was given in terms of the third invariant of the deviatoric tensor, represented by the Lode angle. However, damage evolution and element removal criteria were described as weak spots of the model, as it was dependent on a maximum shear criterion, leading to unrealistic strain peaks when the still stressed element was deleted.
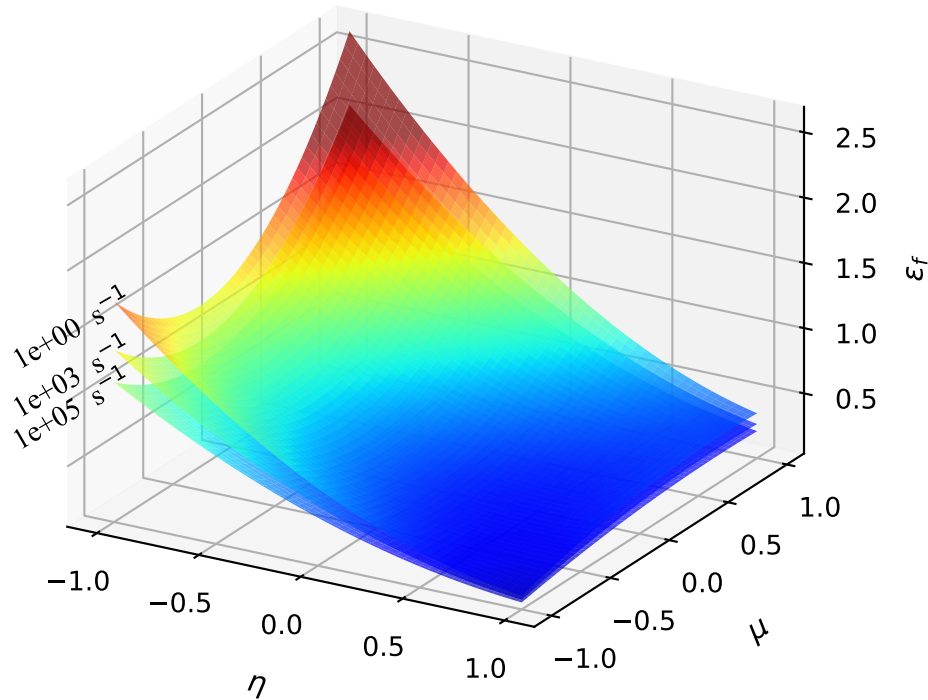
Figure 21 – Damage initiation locus for aluminium AA2024 T341, adapted from the work of Bai; Wierzbicki [47] with a Johnson; Cook [98] $D_{4(JC)}$ strain rate parameter modification

1.6.2 A new damage evolution model

In order to describe fracture in materials with limited ductility, a new damage evolution model needs to be developed in terms of the third invariant of the deviatoric stress tensor. In order to develop the model, the fracture characteristics of the metal need to be well defined, namely the $K_{\text{tiny IC}}$ and $K_{\text{tiny IIC}}$ values and the damage initiation locus. An example of a well fracture-characterized material in literature is the aluminium alloy AA2024 T341, studied extensively by Bai; Wierzbicki [47].

Damage evolution modelling through FEM is normally described by defining a maximum node displacement after the onset of failure, on which stiffness and plastic stress decrease across a certain strain path [94]. Another option was described in the previous section, on which the maximum strain to failure is defined as a function of a constant energy release, G_f, namely Hillerborg's critical energy release rate, the energy required to open a fictitious unit length of crack, as defined similarly as the Barenblatt model [108, 109]. Although this procedure is successful in some cases, these result in unrealistic approaches when there are different fracture mechanisms present in the model, such as in the case of metal cutting.

In Buchkremer; Klocke; Lung [110] work, the Bai; Wierzbicki [47] flow model and damage initiation was applied to analytically predict the chip curl and deformation fields with finite element simulation, based both on Lode angle and triaxiality. The

damage evolution, however, was given in terms of a constant fracture energy and yield strength at failure, namely E_f and σ_{y0}, not accounting for the possible deviation resulting from different fracture mechanisms.

In order to reduce mesh size dependence caused by strain localization after damage initiation, usually a node displacement-dependent variable, rather than equivalent element strain, is used [108], such as:

$$\mathrm{d}u = L \, \mathrm{d}\bar{\epsilon}. \tag{34}$$

Hence, the energy required to open a unit area of crack is:

$$G_f = \int_{\epsilon_c}^{\epsilon_f} L \, \bar{\sigma}_y \, \mathrm{d}\bar{\epsilon} = \int_0^{u_f} \bar{\sigma}_y \, \mathrm{d}u, \tag{35}$$

where L is the characteristic length of the element; ϵ_c is the element's equivalent plastic strain when the damage initiation criterion is met ($\omega_F = 1$); ϵ_f and u_f are the equivalent plastic strain and node displacement at full degradation, respectively. The variable u is calculated only after the damage initiation criterion has been reached ($\bar{\epsilon} = \epsilon_c \therefore u = 0$).1

The energy per unit area to be dissipated during the damage evolution process, G_f, is to be related to the critical stress intensity factor, $(K_C)_{\text{I,II,III}}$, under the characteristic loading mode (modes I, II and III being the tensile, sliding and tearing fracture modes, respectively). During orthogonal machining, modes I and II can be considered to act solely in chip segmentation according to Mabrouki et al. [32], such as:

$$(G)_{total} = (G_f)_{\text{I}} + (G_f)_{\text{II}} + \cancelto{0}{(G_f)_{\text{III}}}, \tag{36}$$

$$(G_f)_{\text{I,II}} = \left(\frac{1 - \nu^2}{E} \right) (K_C^2)_{\text{I,II}}. \tag{37}$$

After damage initiation criterion is met, damage evolution can be described by the variation of mechanical properties (namely stiffness and yield strength) across a displacement path [111]. The hypothesis of the authors for the damage evolution model is as following: given that stiffness decrease is caused mainly by the growth and coalescence of voids during straining [112], and as for shear damage in compression under high pressures the voids are difficult to find as these are seen extensively flattened (if even at all present),*e.g.*, [113, 114], the damage in the case of an ideal pure shear fracture could only be explained by a decrease of yield strength. This hypothesis can be supported by the works of Mogi, Robertson [115, 116] with compression tests in rocks and metals under extreme pressures such as the absence of internal flaws of normally brittle materials and invariability of the elastic modulus after high deformations; and the presence of a negative strain hardening exponent over a critical strain with shear
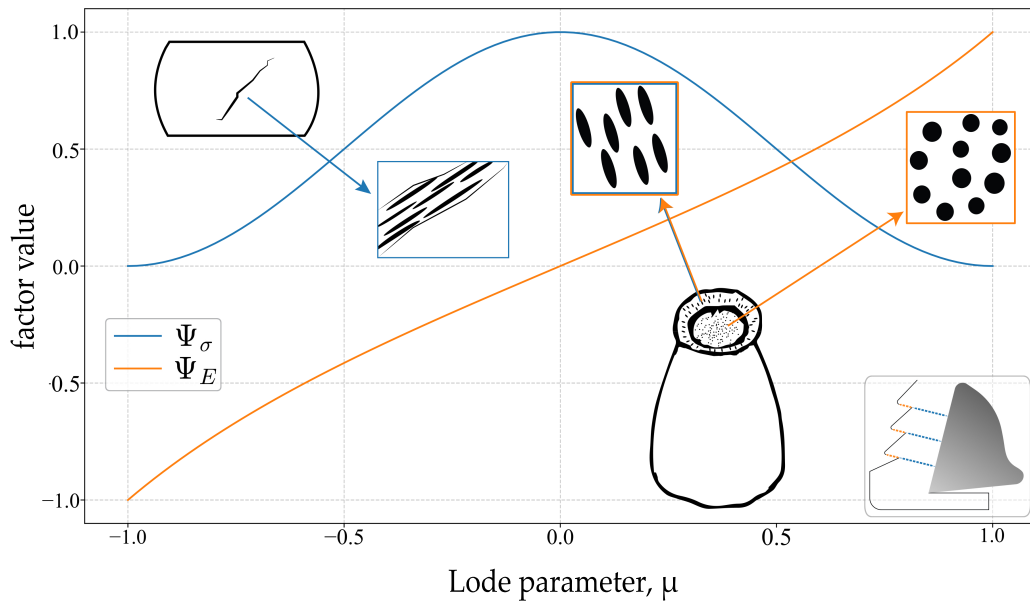
Figure 22 – Variation of the trigonometric functions Ψ_E and Ψ_σ with the Lode parameter and the corresponding ductile cracking mode. The general void shapes in the corresponding regions of a cup and cone and compression fractures are represented by ellipses

deformation tests under extreme pressures as those presented in the work of Shaw [18]. The origins of the yielding decrease can be developed by a proper physical definition of fracture: the propagation of a large discontinuity through the crystal lattice and subsequently disruption of material flow but without material separation, *i.e.*, without the creation of a new surface.

While the data for K_{IC} is sometimes available, a pure mode II testing is difficult to be obtained experimentally [117]. However, a trend on aluminium AA2204 T341 has been found such that K_{IIC} is 15% higher than of the K_{IC} [113].

The damage, therefore, is separated into two independent variables: stiffness and yielding degradation. Stiffness degradation, as considered to be caused by growth and coalescence of voids during a tensile configuration of straining, depends mainly on the Lode parameter. For such, the following modifications to the exponential damage evolution expression are proposed:

$$D_E = 1 - \exp\left(-\int_0^{u_f} \frac{\mathrm{d}u\ \bar{\sigma}_y}{(G_f)_{\text{I}}}\ \Psi_E\right), \tag{38}$$

and for yield strength degradation:

$$D_\sigma = 1 - \exp\left(-\int_0^{u_f} \frac{\mathrm{d}u\ \bar{\sigma}_y}{(G_f)_{\text{II}}}\ \Psi_\sigma\right). \tag{39}$$

These expressions guarantee that the energy dissipated during damage evolution equals $(G_f)_{I,II}$ asymptotically to $D_\sigma, D_E \to 1$.

Ψ_σ and Ψ_E are trigonometric functions describing the partition of the damage increment. They approach an unit when the deformation in the element corresponds to the loading modes I or II, according to:

$$\Psi_\sigma = \cos^2\left(\frac{\pi\mu}{2}\right), \tag{40}$$

$$\Psi_E = \tan\left(\frac{\pi\mu}{4}\right). \tag{41}$$

Equations 40 and 41 describe the factor variation using the Lode parameter based on the consideration of the final damaged shape of voids as flattened ellipsoids. Normalization with the Lode parameter μ, is obtained by considering the condition of maximum ellipsoidal triaxial anisotropy to be given in $\mu \to 0$ and the minimum when $\mu \to 1$. Figure 22 presents the variation of the proposed trigonometric factors with Lode parameter, μ. Equations 40 and 41 were developed based on considering the crack modes, in which a tensile ($\mu = 1$) or a shearing mode ($\mu = 0$) deformation, the values of the functions Ψ_E, Ψ_σ, should approach an unity in their respective characteristic conditions in order to result in a good approximation to the characteristic energy release rate $(G_f)_{I, II}$.

The degradation variables decrease the plastic stress ($\bar{\sigma}_y$) and stiffness ($\bar{E}$), both monotonically and non-monotonically, respectively, through the following equations:

$$\bar{\sigma}_y = (1 - D_\sigma)\tilde{\sigma}_y, \tag{42}$$

$$\bar{E} = (1 - D_E)\tilde{E}, \tag{43}$$

where $\tilde{\sigma}_y$ and $\tilde{E}$ are the plastic stress and the elastic modulus in the beginning of the time increment. The non monotonic nature of the elastic degradation variable is necessary both to describe the complex strain paths on materials which are being cut are presented and the very nature of stiffness degradation: the constraint of void growth and coalescence in compressive configurations. The relation between damage mechanics, void growth and coalescence and its non-monotonical effects in large plastic deformations was described by [118][*].

---

[*]More information about the damage evolution model is presented elsewhere in an article published by the present author [119]

1.7 Fe3Al-BASED IRON ALUMINIDES

1.7.1 Fe$_3$Al-based iron aluminides

In Fe-rich alloys with Al atomic weights greater than 22%, the D0$_3$ (Fe$_3$Al) is present upon cooling. This alloy is being considered for structural applications since it presents greater strength to weight ratio and greater corrosion resistance than most iron-based alloys [120]. The need for reducing the high ductile-brittle transition temperature and inherent brittleness still remains. Many solutions to this problem have been proposed, such as thermomechanical treatments in the B2-phase region [121] and alloying [81, 122, 123, 83]. From these, alloying has been the most successful in hindering atmospheric embrittlement due to hydrogen evolution during straining and increasing cleavage strength. Figure 23 illustrates the D0$_3$ structure.

The highly corrosive resistance of this material is given by its very adherent and resilient α-Al$_2$O$_3$ thin passive film formed in the surface. A bulk sample with 14-17% atomic weight of aluminium can maintain its protectivity up to $900\ °C$ [80]. Iron aluminides present high aqueous solution oxidation and sulfur resistance due to this protective film. However, as with many Al rich alloys, it presents low pitting and localized corrosion resistance, such as in concentrated Cl$^-$ aqueous solutions [124].
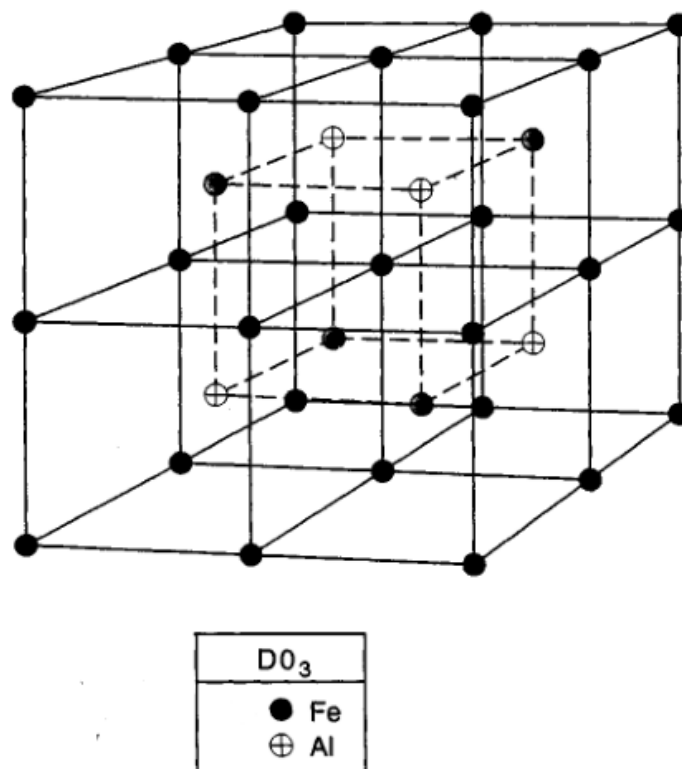
Figure 23 – The D0$_3$ structure. *Source*: adapted from [125]

Another possible important factor for the low ductility is final grain size. While a larger grain size (150 µm) exhibited an engineering ductility of 5%, a finer grain size (7µm) exhibited a 7% engineering ductility. With castings, inoculants are normally used in order to reduce the final grain size of the casting. Ramirez [126] applied a Al-5Ti-B inoculant successfully, reducing in 60% the final grain size of the casting. Grain size and shape, as reported in [121], hinders hydrogen embrittlement evolution.

Fe_3Al presents an interesting anomaly with respect to most metallic alloys – an increase in yield strength with temperature up to 700 ° [80, 89]. The reason for the anomaly is a locking of $< 111 >$ superdislocations[*] to a $< 100 >$, increasing the necessary stress for slipping. This can render difficulties in processing, since machining operations can bring the temperature to such values.

1.7.2 Production methods

Near-net shape processes are those that try to reach the final shape of the component in one single unit operation. For intermetallics, as shown in previous sections, casting is the most widely used. Casting is very technically challenging for Fe_3Al, with problems such as aluminium segregation, which causes brittle pre-cracks during cooling, and very large final grain size [125]. Optimization of castings with properties such as ductility and sulfidation resistance were made with additions of Cr, Zr and Nb.

Ramirez; Schön [86] produced a series of cast Fe_3Al alloys (Fe28Al, Fe28Al6Cr and Fe28Al6Cr1Ti), with varying grain sizes and in experimental and industrial scales. The industrial scale produced alloys with varying grain size with inoculant usage (Al-5Ti-1B), with up to 60% grain size reduction. Titanium addition acted as a greater refining agent than Al-5Ti-1B. The casting defects as shrinkage, pores and inclusions were greatly mitigated, giving good indication of the viability of the casting production method. Figure 24 presents some macrographic results from Y-blocks of the different castings.

Another problem is related to shrinkage, which can take even 20% of casting volume [86]. This can be bypassed with change in composition, heating and pouring practices. Furthermore, even when casting *near-net shape components*, machining can be a crucial part of engineering costs for the final product. In the case of *hard to machine* materials, the cost of machining can be the last straw between viability and unviability of the whole process due to material selection. Hence the need for machining parameters optimization.

Problems related to carbon contamination are also present in the experimental

---

[*]Since the D03 is an ordered structure, the movement of atom planes render further thermodynamic instability in the structure. Hence, dislocation movement is often made by a closely disposed pair of dislocations bounded by antiphase boundaries, named superdislocations.
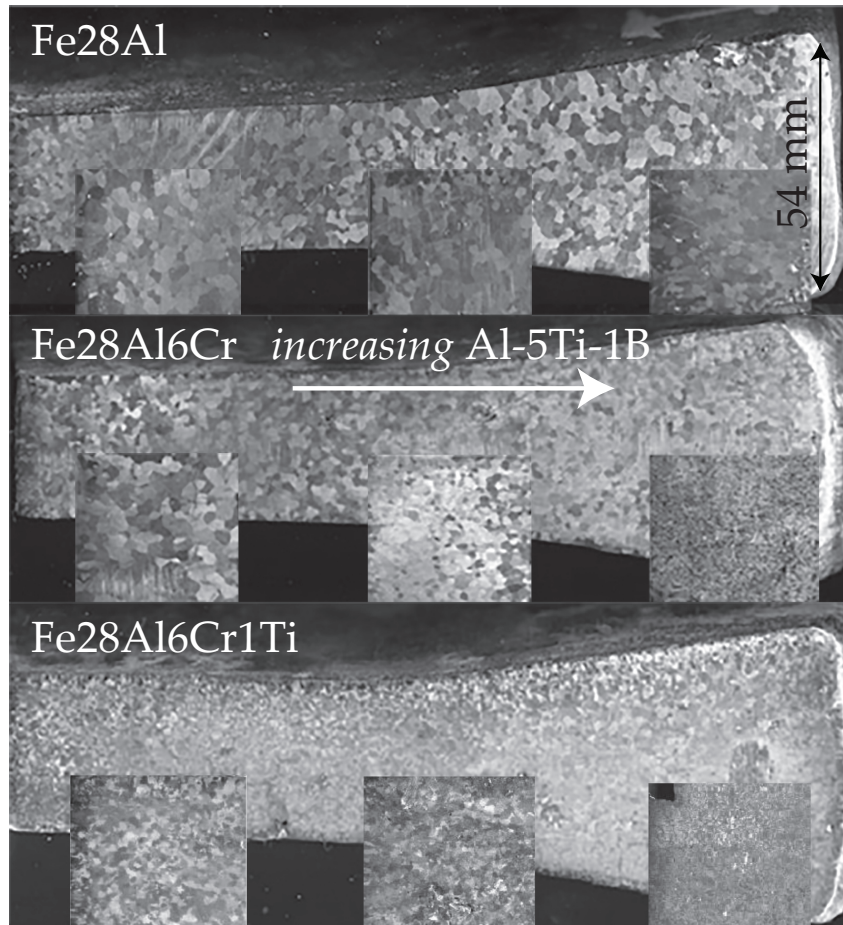
Figure 24 – Macrographs of cast Fe₃Al-*based* alloys (Fe28Al, Fe28Al6Cr and Fe28Al6Cr1Ti) with increasing inoculant content (0.0%, 0.05% and 0.10%). *Source*: adapted from [126]

scales which are not found in industrial scale melts. Whilst large scale presence of κ-carbides can affect properties related to machining, there is no evidence that low concentration of hard second phases can affect machining performance. Major problems with addition of chromium and titanium are related to melt fluidity, which can cause serious issues related to mould filling during casting, especially for the Fe28Al6Cr1Ti alloy.

The solidification and phase transformations a molten Fe3Al-*based* alloys goes through are:

$$L \xrightarrow{1490°C} L+\alpha\mathrm{Fe} \xrightarrow{1455°C} \alpha\mathrm{Fe} \xrightarrow{800 \text{ to } 1100°C} \underbrace{\mathrm{FeAl}}_{2° \text{ order}} \xrightarrow{550 \text{ to } 450°C} \underbrace{\mathrm{Fe_3Al}}_{2° \text{ order}}$$
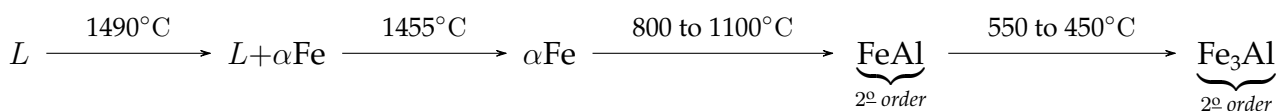
The FeAl and Fe₃Al transformations are ordered phases, hence, characterized as a product of second-order phase transformation. The second-order phase transition temperatures are represented by the hatched temperature lines in Figure 25.
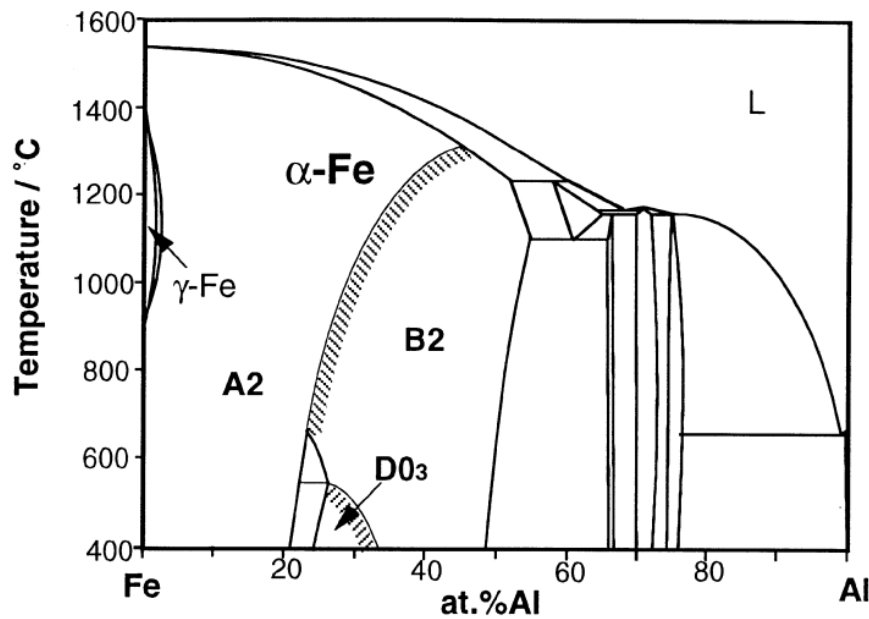
Figure 25 – Fe-Al phase diagram. *Source*: [127]

1.7.3 Machinability of intermetallic alloys

A review of machinability of titanium aluminides (Ti$_3$Al) was made by Castellanos et al. [128], a couple of studies about machinability of nickel aluminides (NiAl) Chatterjee [129] and Blau; DeVore [130]. Studies about machinability of iron aluminides, in turn, contradict themselves in a technological point of view. According to Woodyard [131], high speed steels can be used to machine iron aluminides (Fe$_{25}$Al) while Saigal; Yang [132] affirm otherwise. According to consulted literature, iron aluminides were disregarded for machining operations [133], with reasons related to low ductility and rough casting structure [131]. In 2005, low machinability was related to low ductility and high strains in the interface between tool and workpiece, indicating a high interaction between workpiece and tool in the region of the contact length [134].

Some physical properties are fundamentally important to machinability such as thermal conductivity, melting temperature and hardness [2]. Table 1 presents some physical properties of easy to machine materials (magnesium, aluminium and brass) and relatively hard to machine materials such as low alloyed and stainless steels and nickel superalloys in comparison with Fe$_3$Al.

Although Fe$_3$Al presents brittle behavior under normal conditions ($\approx$ 1-2% of extension in tensile tests), the chip formation mechanism is characteristically ductile — large shear bands and one order of magnitude strain that those presented in tensile testing. The triaxial stresses imposed have much more severe effects in intermetallic alloys than in ductile ones, as the fracture mechanisms are directly inhibited and deformation becomes readily apparent under those conditions [140, 141, 142]. Triaxiality is often defined as $\frac{\sigma h}{\sigma v}$, or the ratio between the hydrostatic components and the deviatoric

Table 1 – Physical properties (thermal conductivity, melting temperature and hardness) of easy and hard to machine materials

Material	$\lambda_t[W/mK]$	$T_{fus}[^oC]$	$HV[N/mm^2]$
AZ10A [135]	110	630	80 Mg, 300 $(Al_{12}Mg_{17})$ *
6061 [136]	180	582	85 Al, 320 $(Al_3Mg_2)^*$
Brass 70/30 [137]	120	915	184 (α)
AISI 4340 (annealed) [138]	44.5	≈ 1427	228 $(\alpha + Fe_3C)^*$
UNS S30400 [139]	16.2	≈ 1425	197 (γ)
Inconel 625	9.9	≈ 1210	≈ 350 $(\gamma + \gamma')^*$
Fe$_3$Al	14.7	≈ 1450	260-350 $(D03 + \kappa)^*$

*Hardness values of the matrix and intermetallic or interstitial phases, independently.

components of stress (represented by the mises equivalent stress, σ_v. Figure 26 presents some examples of chips formed in the machining of iron aluminides, the presence of a white superficial layer on the chip at the tool-chip interface and well-defined shear bands are evidence of great deformations. Machining and analysis of the chip formation mechanism can provide important information regarding plasticity and fracture of seemingly brittle materials under tension. The triaxiality of stress effect on cleavage fracture is a poorly addressed theme in machining studies, as there are less conventional engineering materials that present this fracture mechanism. The majority of engineering alloys fracture in a ductile manner or by disaggregation (such as cast irons).
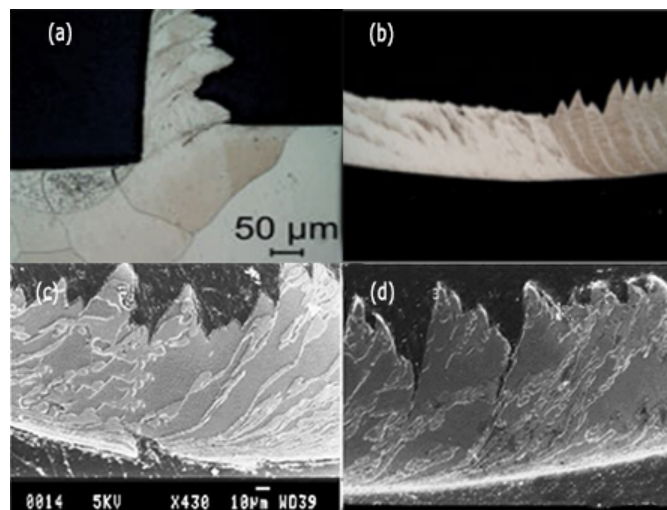
Figure 26 – Examples of transversal sections of chips formed when machining Fe$_3$Al. *Source*: adapted from [84] and [134]

Much effort has been made, recently, in the study of machinability of iron aluminides [134, 84, 143]. Figure 27 presents a turbine blade made of an Fe$_{25}$Al$_{1.5}$Ta alloy, cast and machined, extracted from the Intermetallics 2019 conference abstracts, held in Bad Staffelstein - Germany, by Heiner Michels et al., 2019 [143]. The results from this

work resumed the effect of tool geometry and coating — reporting allegedly up to 74% of reduction in tool degradation rates — variables that will also be studied in this work.

Figure 27 – Turbine blade of $Fe_{25}Al_{1.5}Ta$ alloy, cast and machined. *Source*: [143]

2 OBJECTIVES

The general objectives of this work are:

2.1   GENERAL OBJECTIVES

(1) Describe the effects of damage in the phenomenon of chip segmentation using both numerical and experimental techniques.

(2) Develop a damage evolution model to explain chip segmentation phenomena in materials with limited ductility.

(3) Conclude the role of thermal softening in chip segmentation using numerical models.

2.2   SPECIFIC OBJECTIVES

(1) Conclude the effect between the stress triaxiality and lode angle, fracture in the free surface and its effect on segmentation.

(2) Use an intermetallic alloy with anomalous yield behavior,Fe_3Alas a benchmark to the theory of chip segmentation.

(3) Compare the effects of thermal softening and damage evolution in the mechanics of chip segmentation.

(4) Calculate forces and stresses, determine the cutting ratio, deformations and fracture mode of the chips with the aid of metallography, microinde'ntation and dynamometry for different feeds, both numerically and experimentally.

(5) Evaluate the mechanism and protection capacity of different superficial tool coatings (TiN, Duratomic®) when machining cast Fe3Al.

3 MATERIALS AND METHODS

3.1 MATERIALS

3.1.1 Cast iron aluminides

Cast iron aluminides were produced by Ramirez [126], the alloys were presented in Figure 24. For this particular work, the alloys selected for the work were Fe28Al (alloy A) and Fe28Al6Cr1Ti (alloy B), bothwith no inoculant. The reason for this choice is microstructural integrity, since the alloys cast with these compositions presented the least amount of cracks, which are needed to support the stresses generated in machining without catastrophic failure of the workpiece. The composition of each alloy, measured by XRF and LECO along with its hardness, as measured by micro-indentation is presented in Table 2.

Table 2 – Composition and hardness of cast Fe_3Al alloys. *Source*: composition [126] and hardness (the author)

	Alloy A	*Alloy B*
*Fe**	70.19	63.92
*Al**	28.98	26.02
*Cr**	0.01	8.35
*Ti**	—	0.54
C[†]	0.067	0.078
S[†]	0.008	0.007
hardness[‡]	288.6 ± 12.76	293.56 ± 13.80

all composition data is in % at.
∗ measured by XRF [126]
† obtained with LECO's CS 230
‡ measured with Shimadzu's HMV-2TQDW

Figure 28 presents macrographic cross sections of the alloys A and B and the carbide morphology of each alloy. A higher grain size is observed for alloy A, with long, coarse, elongated carbides. Alloy B presents smaller grain size with spheroidal, fine, dispersed carbides.

3.1.2 Cutting tools

In the work of Ramirez [126], TiN coated tools proved to be a very difficult and challenging task, as tools presented a high level of flank wear across all cutting speeds and feeds. The hypothesis is that there is great amount of diffusional interaction
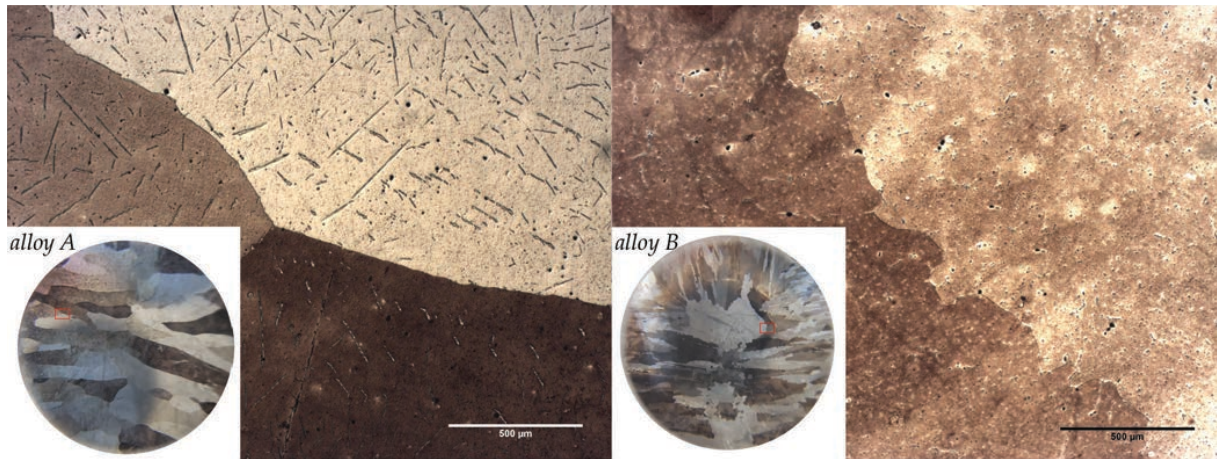
Figure 28 – Macrographic cross sections of alloys A and B and respective microstructures showing carbide particles

between tool and workpiece, along with thermal softening and abrasion, as evidenced by the works of SASAKI; YAKOU [144] and Chowdhuri et al. [134]. For this work, two cutting tools were used for this material, tool 1 (T1): TNMG160412-MF5, TP1501 inserts, provided by SECO Tools, with the Duratomic™coating, an Al_2O_3+TiCN (top to bottom) coating with controlled texture, the top Al_2O_3 will try to fix the issues related to adhesion in TiN and tool tip thermal softening. The tool 2 (T2) is CNMG 12 04 08-WF 4015, from Sandvik Coromant, with TiN+AL_2O_3+TiCN (top to bottom) coating. Figure 29 presents the fractured cross sections of the tools' coating.

Figure 30 presents the cutting tool geometry used for the cutting forces measurement. Table 3 presents overall information about the cutting tools.
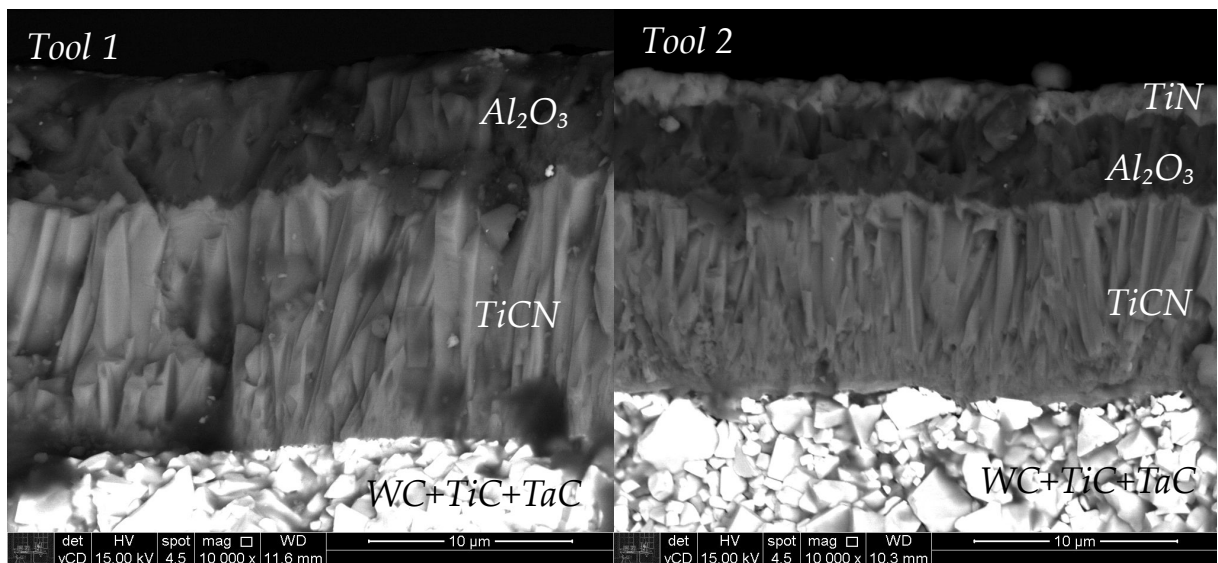
Figure 29 – Fractured cross sections of tools' coating
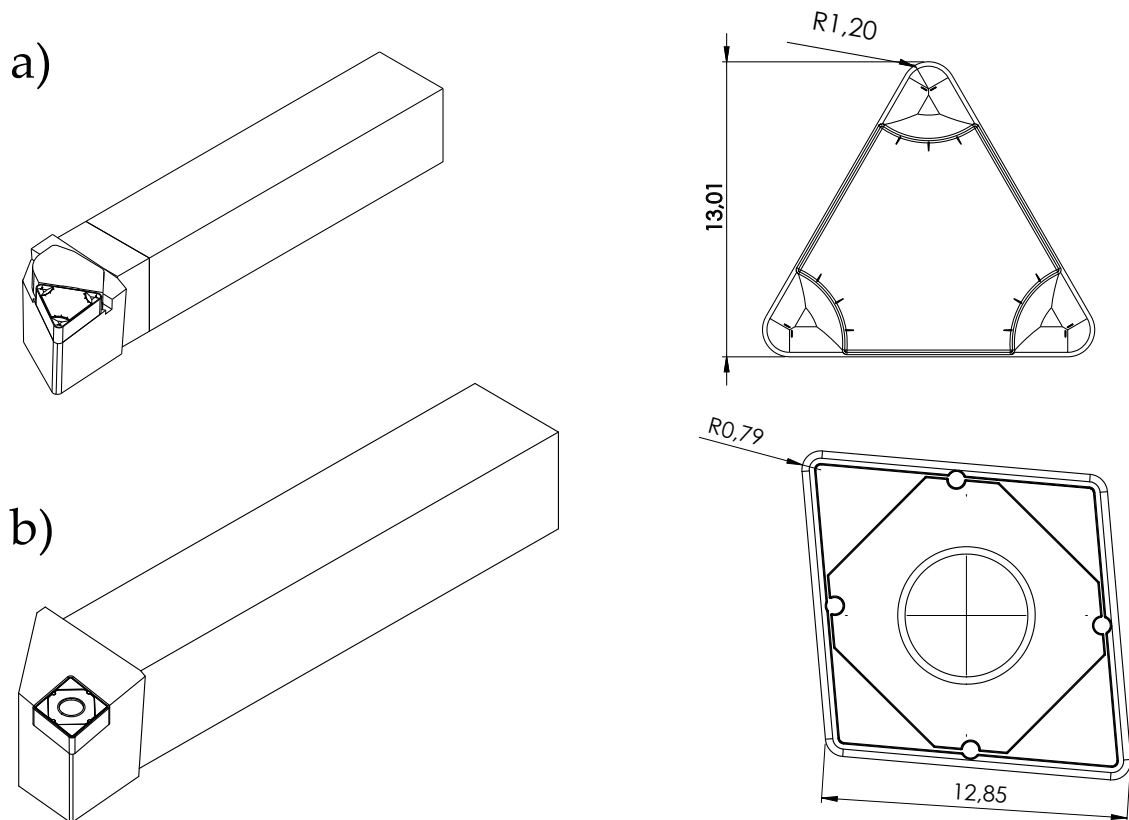
Figure 30 – (a) tool 1, (b) tool 2 cutting tool geometry

Table 3 – Information and data of the cutting tools used.
Source: the author

	T1	*T2*
*effective rake angle**	$-5°$	$-2°$
oblique angle	$3°$	$6°$
clearance angle	$5°$	$6°$
cutting edge radius	1.20 mm	0.794 mm

* *effective rake angle* is measured as *tool-holder rake angle + insert rake angle*

3.1.3 Specimen preparation

The as-cast square stocks extracted from the Y-blocks were circularized to round bars with a 22 mm diameter using a lathe and tungsten carbide tools. The extraction of the round stock from the Y-block casting and an example macrograph of an etched cross-section of a sample are presented in Figure 31.
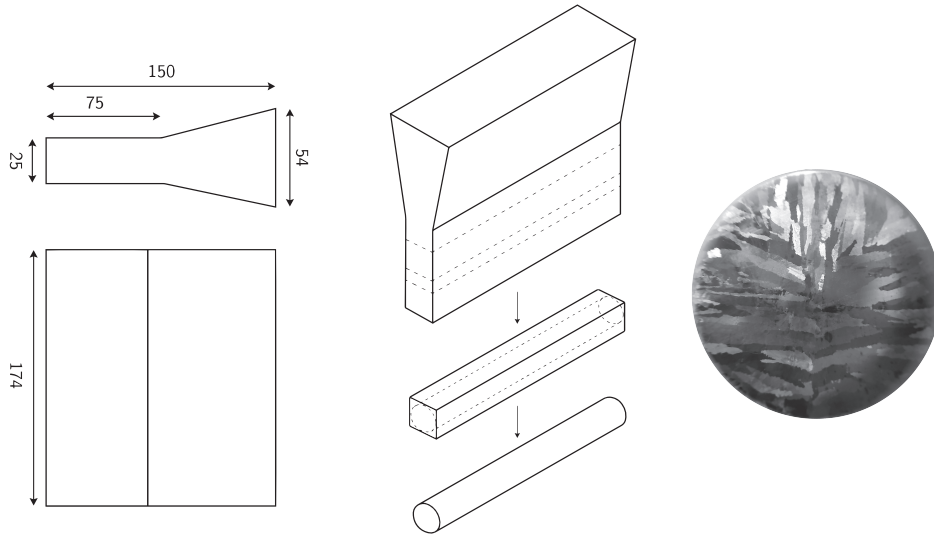
Figure 31 – Example of the extraction of a round stock sample from the Y-block casting and an etched macrograph of the cross-section of the $Fe_{28}Al_6Cr_1Ti$ alloy casting. Dimensions are in mm. The round bar diameter is 22 mm.

3.2 METHODS

3.2.1 Cutting force measurements

Cutting force measurements were made with a piezoelectric dynamometer, 9265B/9441B, with a 5070A 11100 signal conditioner and DynoWare 2825A1-2 signal analyzer, from Kistler. The dynamometer captures the force components in the 3 principal directions, namely F_y, F_x and F_z, with limits of ± 15 kN for F_y and F_x and ± 30kN for F_z. Sensitivity of the piezoelectric snsor is of ≈ -8 pC N^{-1} for the x and y directions and ≈ 3.7 pC N^{-1} for the z direction. Figure 32 presents the *set-up* for the measurement of cutting forces.
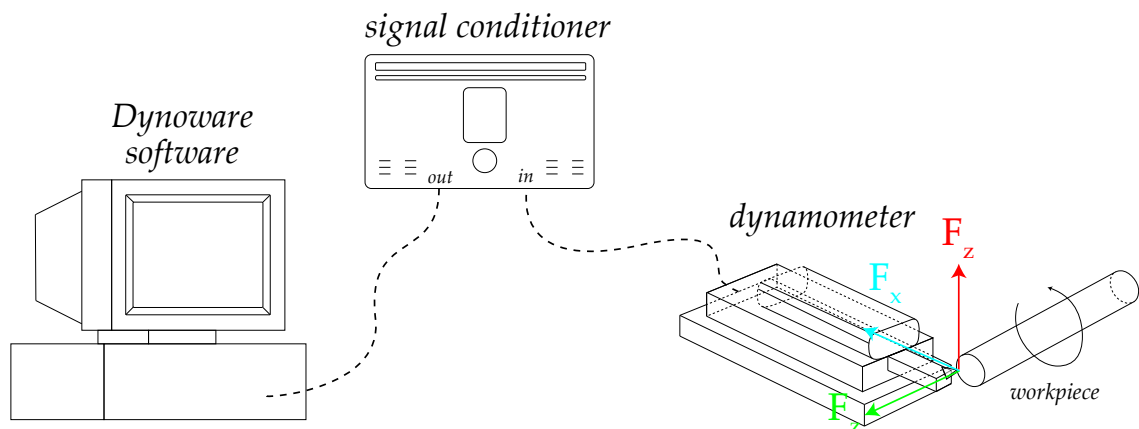
Figure 32 – Dynamometer *set-up* for the measurement of cutting forces. *Source: the author*

The cutting forces were measured for tools with different geometries and coatings, TiN and Al_2O_3, provided by SECO Tools™. Table 4 presents the tool force

Table 4 – Tool force measurements

tool	alloy	feed
T_1	A	0.327
		0.205
T_2	B	0.327
		0.205

measurements. Cutting forces were measured after 3 second contact between tool and workpiece, to ensure a constant cutting regime in order to determine mean cutting forces.

3.2.2 Metallographic inspection

Metallographic inspection for the Fe$_3$Al alloy follows regular mounting with pressure thermosetting bakelite, grinding with subsequent finer grit sandpaper, up to 1600 ANSI grit, and final polishing with synthetic diamond suspension of 3 µm and 1 µm. For chip mounting, metal clips were used to set the chip on its side for inspection of the transverse longitudinal section. The etchant used for metallographic feature inspection was 25 mL acetic acid, 15 mL HNO$_3$, 15 mL HCl and 5 mL H$_2$O for 10 seconds [126], this etchant reveals grain boundaries but also deformation shear bands in Fe$_3$Al.

3.2.3 Orthogonal FEM model and damage evolution model implementation

A complete stress characterized and asymmetrical locus damage initiation criterion, was proposed by Bai; Wierzbicki [47]. Here, this criterion is modified in the strain rate dependence, adopting the approach of Johnson; Cook [98]:

$$\epsilon_D(\eta\,,\mu\,,\dot{\bar{\epsilon}}) = \left\langle \left[\frac{1}{2}\left(\epsilon_D^{(+)} + \epsilon_D^{(-)}\right) - \epsilon_D^{(\circ)}\right]\mu^2 + \frac{1}{2}\left(\epsilon_D^{(+)} - \epsilon_D^{(-)}\right)\mu + \epsilon_D^{(\circ)}\right\rangle \left(1 - D_{4(JC)}\ \ln\frac{\dot{\bar{\epsilon}}}{\dot{\epsilon}^{\circ}}\right). \tag{1}$$

The superscripts in $\epsilon_D^{(+),(\circ),(-)}$ represent the maximum strain at the characteristic loading condition, such as $(+)$, $(\circ)$ and $(-)$ are the characteristic axial symmetry strain in deviatoric tension ($\mu = 1$), pure shear or generalized plane strain ($\mu = 0$) and axial symmetry strain in deviatoric compression ($\mu = -1$) loading conditions, respectively.

Furthermore, Bai; Wierzbicki [47] use an exponential relation for the inclusion of the effect of stress triaxiality, based on the theory of McClintock [145] and Rice; Tracey [102],

$$\epsilon_D^{(+)} = D_1 e^{(-D_2 \eta)},$$
$$\epsilon_D^{(\circ)} = D_3 e^{(-D_4 \eta)} \text{ and}$$
$$\epsilon_D^{(-)} = D_5 e^{(-D_6 \eta)},$$

where D_1 to D_6 are the six model parameters that were calibrated, the parameters extracted from [47] are presented in Table 5.

Strain rate dependence on damage initiation is not included in the original model of Bai; Wierzbicki [47]. So the strain rate parameter of the Johnson-Cook damage model parameter $D_{4(\text{JC})}$ [98] is used here to modify the surface with respect to strain rate, as presented in Figure 21.

To investigate the ability of the model in describing the chip formation mechanism, the software Abaqus ™(version 6.14) in its numerical explicit formulation was used. The simulation was set as a common 2D, non-thermally coupled model. The choice of not including thermal effects in the analysis is justified by the fact that the inelastic heat generation was overestimated in early tests with the current model. It is reasonable to think that the continuum definition of a damage in the plastic properties would also incur in alteration in the thermal properties, especially the inelastic energy heat fraction of the continuum itself as it is currently known that a constant inelastic heat fraction is a highly simplistic consideration [146]. As thermal inelastic heat generation is currently defined in terms of plastic strain in Abaqus [94] ™, it is considered as a possible source of error in the present work. A more robust implementation of the model with thermal coupling using the VUMAT subroutine of the software with a better physical relationship of the damage process with inelastic heat source is needed.

A FORTRAN code was written for Abaqus ™ under subroutines UHARD and VUSDFLD. UHARD subroutine was used to define a Johnson-Cook strain hardening law [98]. With subroutine VUSDFLD the state variables such as the Lode parameter, strain rate, the stress tensor and its corresponding invariants were calculated. The previous step plastic yield stress $\tilde{\sigma}_y$ is exchanged between both subroutines, in order to integrate the values of D_E and D_σ and update the new $\bar{\sigma}_y$ and $\bar{E}$.

A simple explicit tensile model for the visualization of the damage variable partition was built with the same material models as previously stated in order to attest the visual accuracy of the post-processing integration. The objective of the explicit tensile model is to attest the partition of the damage variables across the specimen's cross section.

Figure 33 illustrates the calculation process given by the code using VUSDFLD and utility subroutine VGETVRM for a material point. The damage initiation criterion

ϵ_D and the $\bar{\sigma}_y$ and $\bar{E}$ value update method used are optional. In this work, the Bai; Wierzbicki [47] criterion, VUSDFLD and UHARD subroutines were used for damage initiation criterion, $\bar{E}$ and $\bar{\sigma}_y$ value update, respectively.
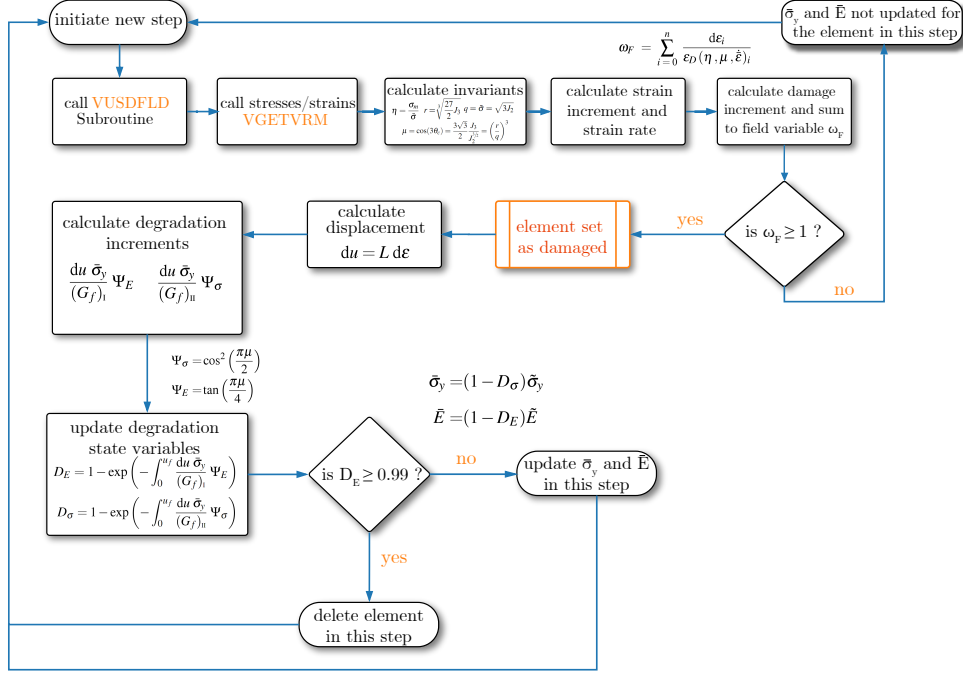
Figure 33 – Flowchart illustrating the calculation process for damage damage initiation and evolution in a finite element by the current model in a given simulation step

Figure 34 presents the machining simulation boundary conditions, parts and dimensions. Part 2 is a thin layer that promotes chip separation from the bulk (Part 3), and is subjected to a maximum strain criterion to full degradation ($\epsilon_f = 2$). Part 1 is the uncut chip, with variable thickness f. The variable tool speed, v, is set as one of the boundary conditions for the model, while the rest are fixations. The last variable is rake angle φ. The physical properties and Johnson-Cook's parameters of the AA2024 T341 alloy were extracted from [87], and are presented in Table 1. All elements are CPE4R quadrilateral, plane strain, hourglass control with reduced integration, assigned in an homogeneous section with plane stress and strain ratio thickness equal to the respective depth of cuts.

Interaction between tool, defined as an analytic undeformable solid, and workpiece has been defined as a surface-to-surface contact with tangential penalty behavior with a constant friction coefficient ($\mu_f = 0.2$), until maximum shear friction stress τ_{max} is reached, which in turn is defined as the initial yield stress (σ_y). Therefore, the frictional shear stress (τ_f) is defined as:

$$\tau_f = \begin{cases} \mu_f\, p & \text{for } \tau \leq \tau_{max} \\ \tau_{max} & \text{for } \tau > \tau_{max} \end{cases}. \tag{2}$$

Table 5 – Material properties used in the simulations

	Material property [unit]	Al AA2024 T341
Johnson-Cook parameters	A [MPa]	265
	B [MPa]	426
	n	0.41
	C	0.01
	$D_{4(JC)}$	0.011
	Density, ρ [kg m^{-2}]	2770
	Elastic modulus, E [GPa]	73
	Poisson's ratio, ν	0.265
	$K_{(IC, IIC)}$ [MPa m$^{1/2}$]	28.0, 32.2 *
Bai and Wierzbicki parameters	D_1	0.5862
	D_2	1.3576
	D_3	0.2170
	D_4	0.0400
	D_5	0.4859
	D_6	0.7000

* The value of 32.2 is obtained by a trend of $K_{IIC} = 1.15 K_{IC}$, following the work of Jones; Chisholm [113].
[87] (Johnson-Cook viscoplastic parameters)
[136] (fracture toughness values)
[47] (damage initiation locus parameters)
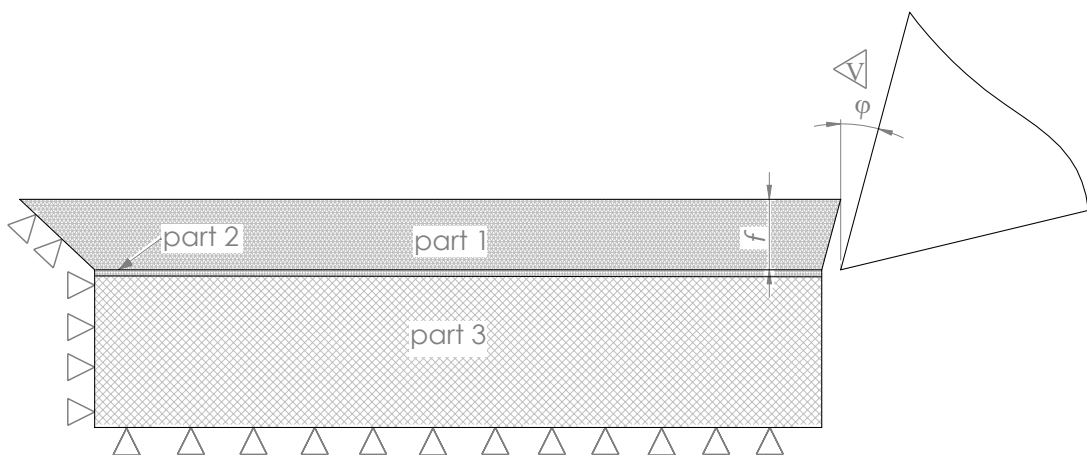
Figure 34 – Machining simulation boundary conditions, dimensions, and parts
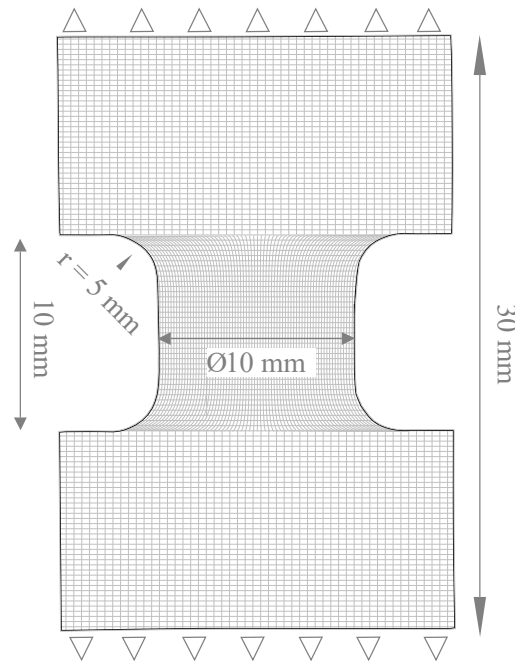
Figure 35 – Tensile simulation boundary conditions and dimensions

For the evaluation of chip morphology and cutting forces, the built-up edge is a major related variable in multiple feeds and speeds. The built-up edge is the sticking of a hardened material at the tip of the tool, giving rise to a sharp edge that reduces cutting forces by reducing the straining of the chip.

In order to realistically determine the accuracy of the model, the built-up edge phenomenon is taken into account by incorporating it into the solid rigid tool geometry. The built-up edge geometry to be incorporated to the tool edge, was taken from the high speed photographs taken in [69], whenever present.

Figure 35 presents the tensile test finite element model boundary conditions and part dimensions. The velocity of the edges are set to $1\,\mathrm{mm\,s^{-1}}$, each. The physical properties for the material are the same as the machining model, already presented in Table 1. All elements are set in an homogeneous solid section with C3D8R elements. The simulation is ended when the total material separation is achieved.

For the obsevation of dynamic damage evolution in the chips, a Fe$_3$Al machining model was derived from this orthogonal model. Since the cutting forces are not a major interest for this particular simulation, the flow properties were roughly derived from literature. The flow properties were derived from the data in [147] with a strain rate parameter derived from [148]. The chips were subsequently collected and mounted with its cross-section prepared (grinding/polishing) for etching and metallographic inspection. Etching was conducted using a $5\,\mathrm{mL}$ H$_2$O, $15\,\mathrm{mL}$ HNO$_3$, $15\,\mathrm{ml}$ HCl, and 25 mL acetic acid solution for 10s to reveal shear bands and cracks [126].

3.2.4   Coupling thermal effects

In order to couple thermal effects, the damage initiation and the newly developed damage and damage evolution models were implemented into a modified and adapted robust coupled-temperature VUMAT subroutine framework, firstly developed by Ming; Pantalé [149]*. The code uses the methodology of inelastic heat generation presented in Section 1.5.3 and is presented in Appendix A.

---

*The original code (without damage) by Ming; Pantalé [149] is available at github.com/pantale/abaqusVumat

4 RESULTS AND DISCUSSION

4.1 DAMAGE EVOLUTION MODEL

4.1.1 Effect of element characteristic size

The effect of element characteristic size, L, in the results of machining simulation is well known [150]. To investigate these effects, simulations with different element characteristic sizes were produced, *i.e.*, 15, 22, 30 and 40µm. The effects of element size in the morphology of the chip is presented in Figure 36
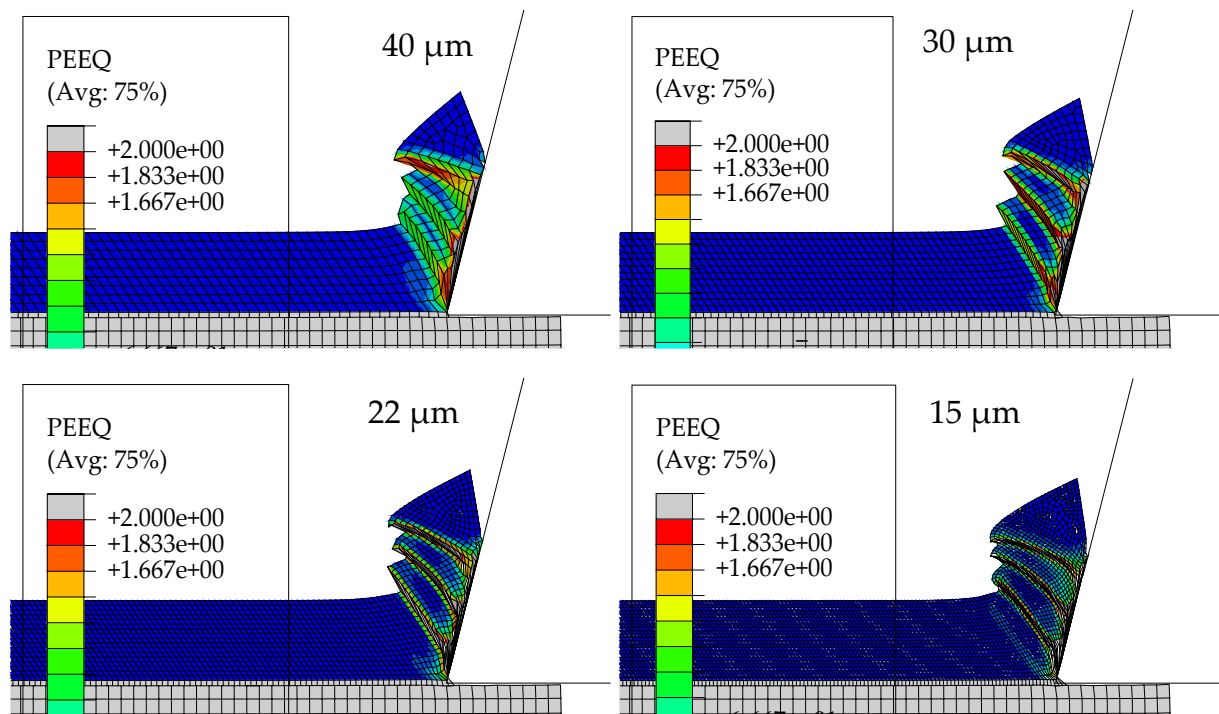
Figure 36 – Chip morphology and equivalent plastic strain for different characteristic element size, L

As presented in Figure 36, chip morphology, in terms of segmentation frequency and plastic deformation barely changes with L, the most important change associated with the reduction of L is the primary shear angle, which slightly increases with reducing element size. This has the effect of slightly increasing the cutting forces, as presented in Figure 37. The difference is minimal, related to the initial contact of the tool and reduces with the progress of the tool and we can assume that the current damage evolution model correctly predicts the size effect within the scale of element size studied (22µm).

Small element sizes in the FEM is related to high computational costs. A good
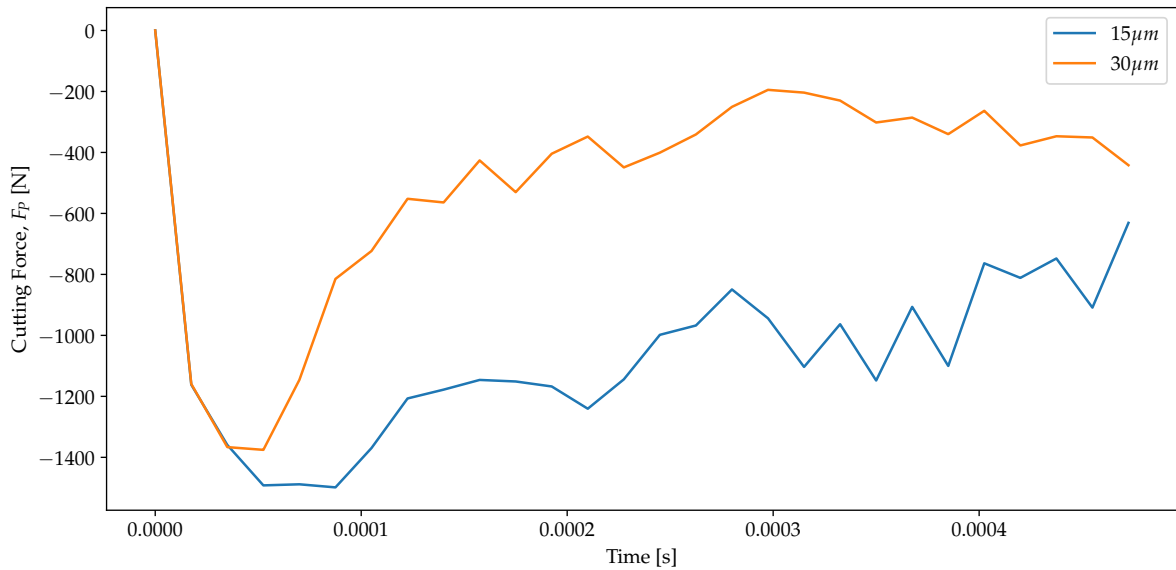
Figure 37 – Cutting force, F_P for different characteristic element size, L

balance between computational time for solution and solution accuracy was in the order of 22μm, and was the L used for this work.

The results from the simple tensile test at the onset of separation are presented in Figure 38, the partition of damage variables seem to accurately describe the cup and cone fracture, as illustrated in Figure 22.

The presence of a D_σ variable, indicates the tendency towards elongated shear-like dimples, which is present on the edges of the cup fracture, whilst the equiaxial dimples are present in the region on which D_E is the highest: in the center of the specimen. This association, however, is product of an approximation of voids as ellipsoids and the true meaning require further investigation, which is outside of the scope of the present work.

When the D_E value reaches its highest, the material is fully damaged with regards to its stiffness, due to the exponential growth and coalescence of voids. Hence, we can define the D_E value as a measure of material separation, or the creation of new surfaces, which is the most recognizable aspect of fracture phenomena. As to the D_σ variable, it is the harder to observe the phenomenon with regular experimental techniques, as no true surface is created when it is the only variable present – as the damage represents plastic disruption due to shear bands and similar large plastic discontinuities. Furthermore, with the pressures and temperatures present in the process, it is unlikely that the resultant microstructure would express such phenomena due to diffusion and annealing in the flow disruption. The way we can attest its existence is due to the shape of the voids, where the shearing angle of 45° with regards to the main stress produces an elongated dimple-like structure whenever the yielding is
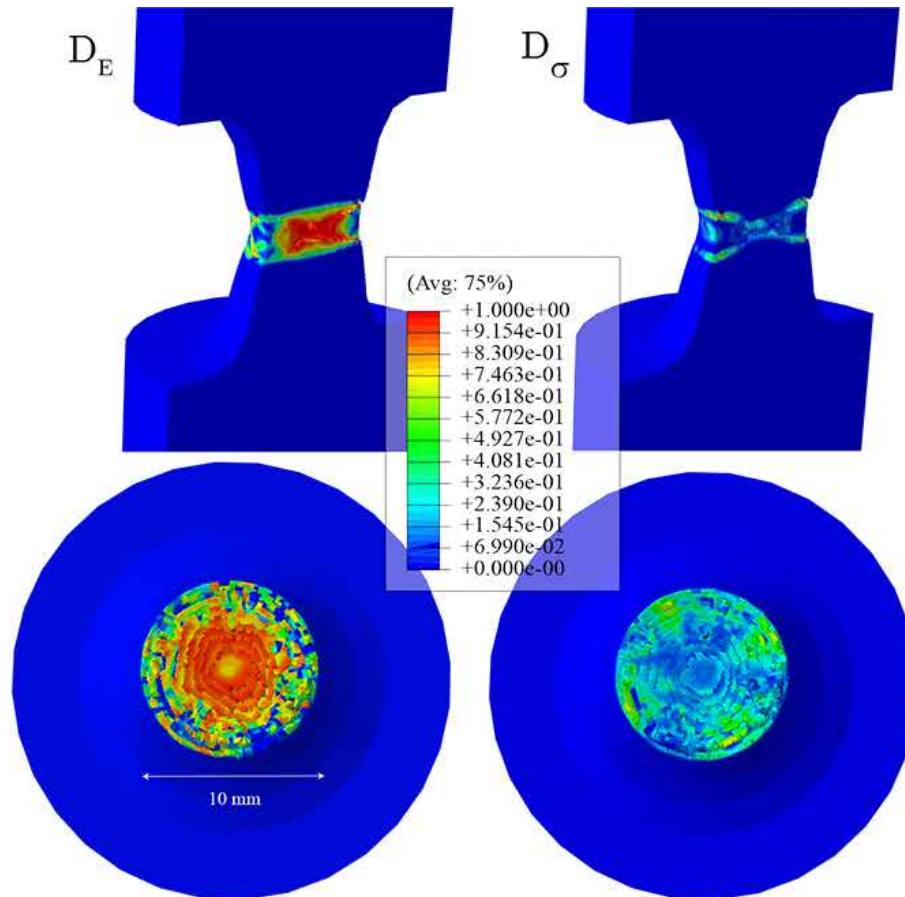
Figure 38 – Node averaged D_E (top and bottom left) and D_σ (top and bottom right) variables at the onset of material separation due to damage evolution under tensile strain in the cup and cone region of the fracture after complete separation. The elements are deleted when $D_E = 0.99$

characterized as to being produced by a shearing stress ($\mu = 0$), and presence of large plastic discontinuities and shear bands.

Experimentally, in the chips' regions of greatest D_σ, the damage is not firstly seen because of the friction and rewelding induced by very high pressures and temperatures imposed in the newly created flow disruption, the flow disruption expresses itself as shear bands and large plastic discontinuities. Hence, an important lexical definition of fracture must be made with respect to the nature of a mixed mode fracture at very high triaxial stresses: if we define fracture as the creation of new surfaces through imposed strain, then the D_E parameter should be the only factor inducing fracture and D_σ should be neglected. If so, the reason for the definition of the D_σ variable, which is based on the same fracture mechanics assumptions as D_E, can provide satisfactory results on chip morphology and fractographic features with the given model would remain unknown. However, if fracture is instead defined as a rapid plastic flow disruption caused by a critical strain, then the effects of both D_σ and D_E successfully describe fracture at very high triaxial stresses.

In the works of Bridgman [50] and Shaw [18], the flow properties of ductile and brittle solids under high compressive stresses were severely different from those under regular conditions, with the common feature of increased ductility. Brittle specimens such as a single crystal of Al_2O_3, tested in compression under a pressure of 2688 MPa, presented an extensive apparent deformation by slipping, although with irregular fracture surfaces across the shear cleavages, this apparent increased ductility phenomenon was repeatedly present on many other brittle materials as cemented carbides, which presented a shortening of 10% of sample size under similar conditions, without strain-hardening [50]. The effects of triaxial stresses on flow properties of solids were first extensively studied in geological processes, considering the extreme pressures and temperatures on which these materials are subjected [115, 116]. Ductile specimens (low carbon steel) presented an apparent negative strain hardening index above a critical strain when tested in simple shear with a normal stress imposed on the shear plane [18]. These are strong arguments that ductile fracture ought to occur even when no apparent surface is being created.

4.1.2 Validation of the model with respect to chip morphology

The present section will deal with the numerical results obtained by simulation of metal cutting with the present model. The chip morphology was evaluated according to segmentation frequency and contact length with different rake angles and speeds.

Resultant chip morphology and the D_E and D_σ variables are presented in Figure 39, numerical and experimental cutting force results are presented in Table 6. The simulation is in overall good agreement with experimental results obtained by Kouadri et al. [69], regarding chip morphology and fracture characteristics with varying feed and rake angle. In the 0.3 mm feed simulations, a gross crack is formed in the surface where the stiffness degradation parameter D_E is the largest, which is in agreement with the hypothesis of Shaw [5] that the fracture (as defined by material separation due to cracking) is expected to initiate in the region where hydrostatic stresses are the minimum, *i.e.*, in the free region of the chip.

Table 6 – Experimental [69] and numerical results (mean cutting force and contact length) obtained with a constant cutting speed of 60 m s^{-1}, depth of cut of 4 mm and variable rake angle and feed

feed [mm]	rake angle [°]	Cutting force [N]		Contact length [mm]	
		Exp. [69]	Num.	Exp.[69]	Num.
0.1	0	430	650	0.16	0.30
	15	–	390	0.12	0.22
0.3	0	1200	1428	0.60	0.52
	15	1200	1346	0.60	0.60
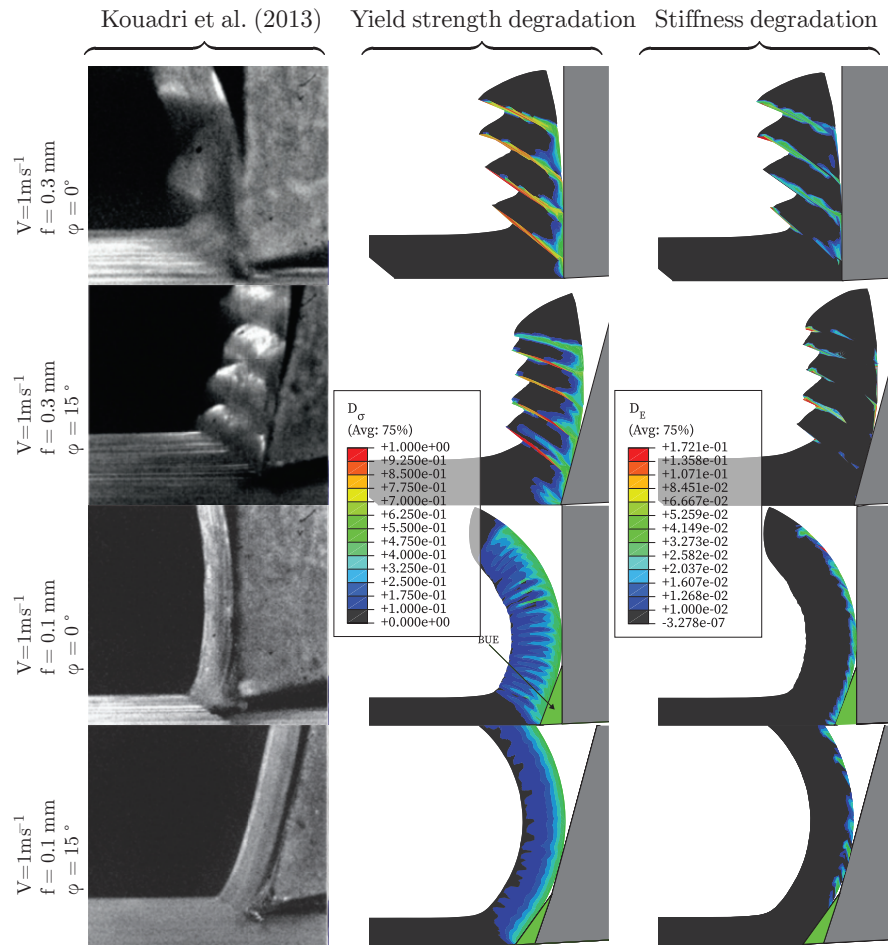
Figure 39 – High speed photographs of orthogonal machining sections with cutting speed of 60 m min^{-1} obtained by Kouadri et al. [69] (reproduced with permission of Elsevier) and resulting simulations with the present model

As previously stated, the D_E variable is related to the phenomenon of material separation. In the continuous chips, as produced with $f = 0.1$ mm, the maximum value of D_E is given in the bottom region of the chip, where the separation of the chip and the bulk material is given. Nevertheless, the D_σ variable and strain localization is always present in the cutting process, even for the continuous chips.

As previously stated, finite element machining models based purely on flow modification previously failed to explain the presence of surface roughness on the chip free surface. As shown in Figure 40, the surface contains a roughness related to both the D_E and D_σ variables, reducing the shear plane length, and thus concentrating strain and damage in its extension. This is in agreement with the results of Guo; Compton; Chandrasekar [33] with regards to the phenomenon of strain localization in apparently continuous chips.
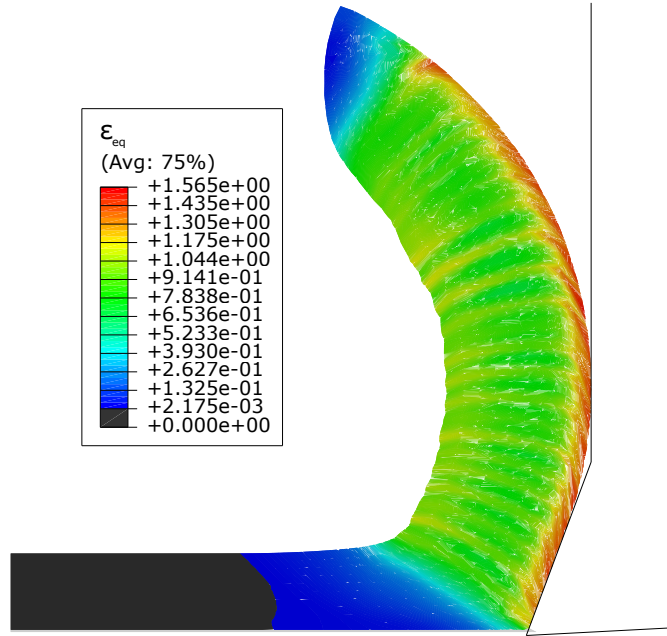
Figure 40 – Numerically calculated plastic deformation at nodes produced by orthogonal cutting at 1 m s^{-1}, zero rake angle with built-up edge and $f = 0.1$ mm with a resultant surface roughness. The variable ϵ_{eq} is defined as $\epsilon_{eq} = (1 - D_\sigma)\bar{\epsilon}$

4.1.3 Cutting speed

It is known that the increase in cutting speed increases segmentation frequencies and reduces cutting forces, numerical results for these variables are illustrated in Figure 41. The segmentation frequency, as calculated with respect to cutting force fluctuation, is in overall agreement with experimental results obtained by [32]. However, this agreement seems to hold off slightly in the high cutting speed range, which is probably related with the thermal effect neglection of the model.

The resultant degradation variables expressed at averaging nodes for the resultant chip is shown in Figure 42. Chip morphology was closely reproduced for both velocities when compared to the results of [32], as shown in Figure 42. However, segmentation intensities seem to be lower in cutting speeds of 200 m min^{-1} in contrast to numerically obtained for the same speed. This can either be attributed to the neglection of thermal properties in the current model or the presence of a BUE in the speeds present in the speed range of $0 - 150 \text{ m min}^{-1}$.

Another important result obtained by the simulations shown in in 39 and 42 is that the effective equivalent plastic strain ($\epsilon_{eq} = (1 - D_\sigma)\bar{\epsilon}$), is always the same at the region of segmentation, which is consistent with the experimental results obtained by Guo; Compton; Chandrasekar [33], giving further support to the critical strain to fracture theory.

The numerically (mean cutting force) and experimentally results obtained by
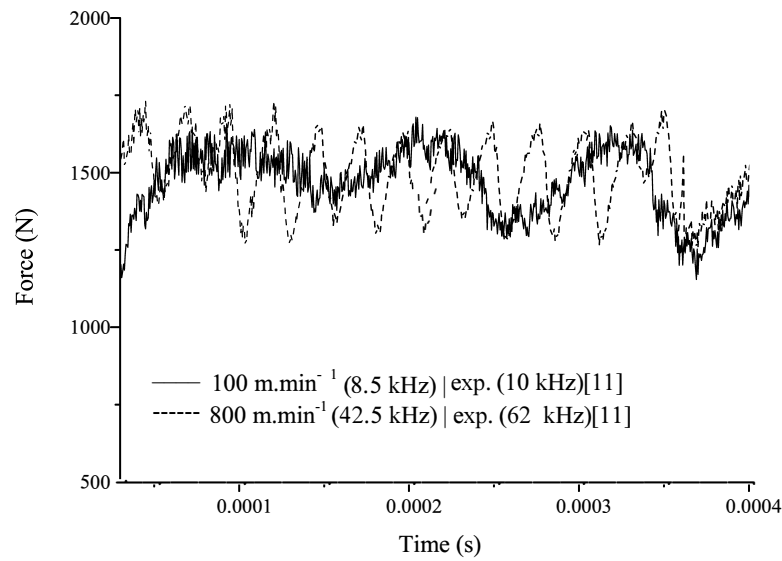
Figure 41 – Numerical obtained mean tool forces with $f = 0.4$ mm and variable cutting speeds

Table 7 – Experimental and numerical results obtained with a constant feed of 0.4 mm, depth of cut of 4 mm and variable cutting speed

feed [mm]	cutting speed [$\mathrm{m\,min^{-1}}$]	cutting force [N]	
		exp. [32]	num.
0.4	60	1150	1475
0.4	800	975	1470

Kouadri et al. [69] are presented in Table 7. As in the segmentation frequency, the cutting forces are also in overall agreement with experimental results in the low cutting speed range, where overall thermal effects are minimized.

While the segmentation frequency presented the same appreciable variation across different cutting speeds, the cutting force remained the same, which contradicts the results obtained by Mabrouki et al. [32] and Kouadri et al. [69] with the same speeds and feeds. This is an expected result and attributed to the neglection of thermal effects on flow properties, as previously described. The cutting speed effect in the thermal softening and further discussions will be made in Section 4.1.4

4.1.4   Cutting speed with coupled thermal behavior

It is known that by increasing cutting speed there is a reduction in cutting forces, mainly due to the reduction of strength with temperature. With varying cutting speed, the magnitude of variables that define the cutting forces are many, the strain rate is responsible for increase in strength, while thermal softening due to adiabatic effects reduce it. In order to illustrate the effects of cutting speed in the thermal softening, two simulations with varying cutting speed were executed, similarly as shown in Figure
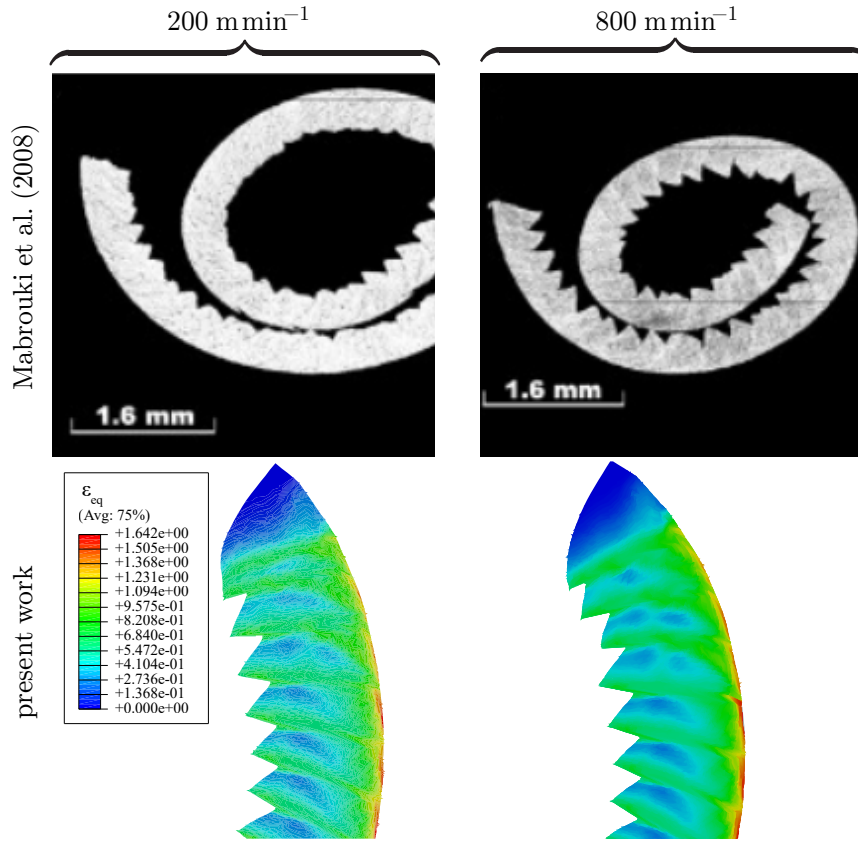
Figure 42 – Chip morphology obtained with variable cutting speed obtained by Mabrouki et al. [32] (reproduced with permission of Elsevier). The variable ϵ_{eq} is defined as $\epsilon_{eq} = (1 - D_\sigma)\bar{\epsilon}$

42, but this time with thermal coupling. By analyzing in terms of the Johnson-Cook softening parameter, θ_m and the damage evolution softening paramter, D_σ, which vary from 0 to 1, we can compare the magnitude of thermal softening with regards to damage, as shown in Figure 43

In this case, when comparing to the experimental results presented in Figure 42, the chip morphology is now accurately described in terms of segment length and shear angle extent. The simulation predicts that thermal softening behavior only aids the localization of strain along the shear plane, but it is not the responsible for the formation of the segment, as shown in the $60\mathrm{m\,min}^{-1}$ speed. It is observed that even for the $800\mathrm{m\,min}^{-1}$ speed, the θ_m parameter reaches a maximum of 0.4 of reductionof strength, while the damage variable reaches 0.9. Shaw [151] conclusion on the rootcause of segmentation is confirmed by the numerical results presented in this work.

4.1.5 Further considerations of thermal effects

In the cases studied in this work, *i.e.,* in materials with limited ductility [119], such as Al 2024-T351 and Fe$_3$Al, the effects of damage are the most important aspects of chip segmentation, on which damage mechanics alone can explain the phenomena accurately,
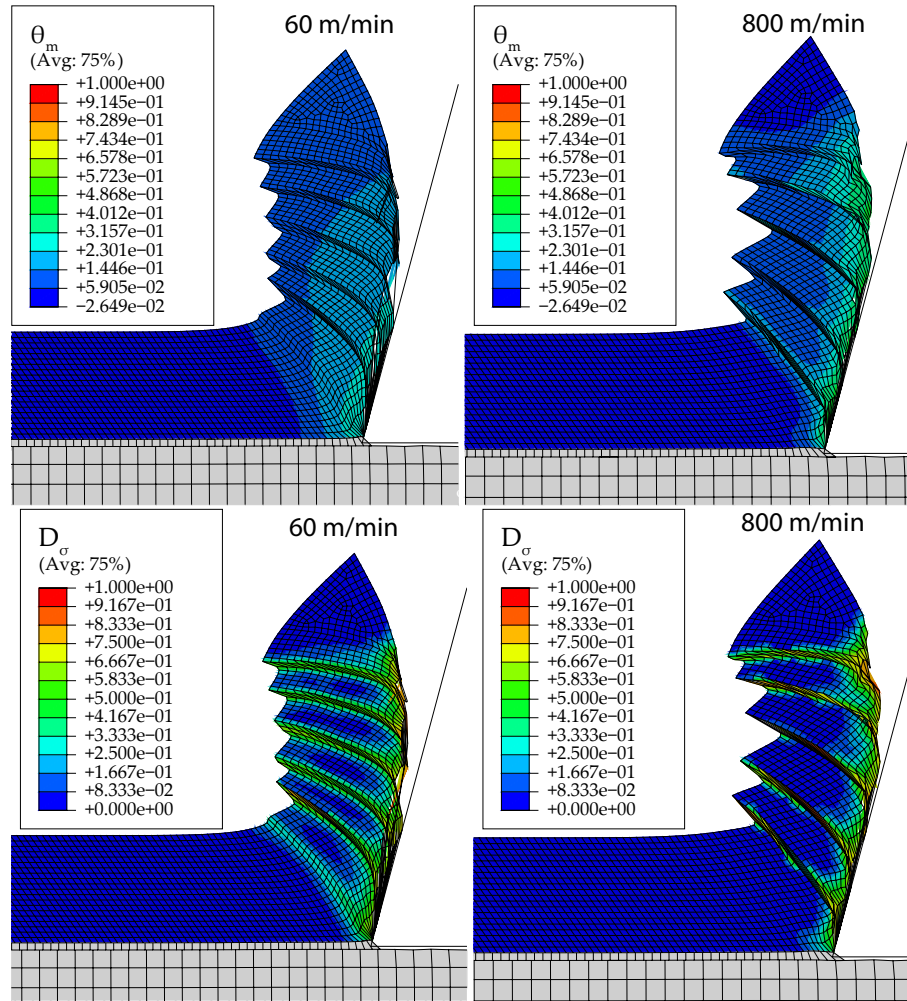
Figure 43 – Scalar damage variables for thermal, θ_m and plastic D_σ, with varying cutting speed, 0.3mm feed

without thermal assumptions. In materials with high fracture energy this assumption may be proven invalid, specially in materials with lower thermal conductivity, such as austenitic stainless steels. In this case, the same simulations presented in Sections 4.1.3 and 4.1.4 was conducted with an austenitic stainless steel, with Johnson-Cook plastic and damage models extracted from [152] and the current damage evolution model, with a fracture energy of 150kJ m^{-2}, extracted from [153]. The cutting speed was set to 120m min^{-1}. The results are presented in Figure 44.

It can be observed that the D_σ field variable has strong correlation with the θ_m, from which the segmentation mechanism is needed. The segmentation phenomenon could not be reproduced without the thermal coupling as presented in Annex A. While the model itself needs more robustness in order to describe accurately cutting forces and morphology, the current simulation is only to illustrate the thermal effects to the mechanics of chip segmentation. In materials with high ductility and high melting point, the segmentation can only be explained with thermal assumptions.
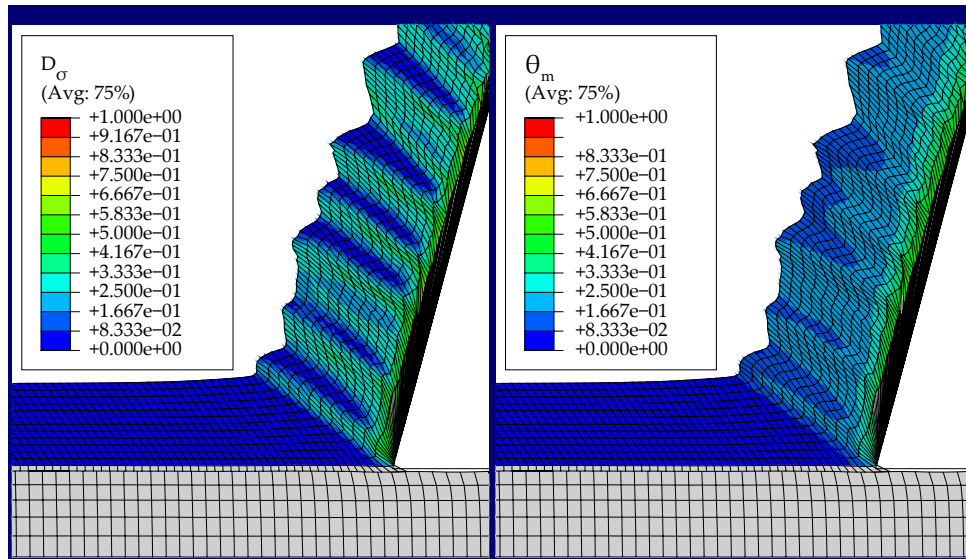
Figure 44 – Simulation of chip formation of an austenitic stainless steel (AISI 304), cutting speed of $120\mathrm{m\,min^{-1}}$. There is a strong correlation of D_σ and θ_m in the mechanics of chip segmentation for the simulation of this material with the given model.

4.2 DYNAMIC DAMAGE EVOLUTION UNDER HIGH TRIAXIAL STRESSES IN Fe$_3$Al

The work of Shaw [18] presents an hypothesis of the very high strain capacity although with negative apparent strain hardening of materials subjected to very high triaxial stresses. The hypothesis is that the role of micro cracking is fundamentally responsible for such strains, providing further displacement after a crack is initiated and propagated to the region opposite to the shearing direction. The following mechanism was proposed:

- damage initiates with the formation of microcracks under critical strains,

- the microextrusion leads to the establishment of pressure welds.

The formation of microcracks, as a surface formation phenomenon, should by definition be accompanied by an increase of the D_E variable: defined previously as the creation of new surfaces due to tensile deviatoric configurations of strains. Furthermore, the microcracks should move to the direction opposite of the shearing direction, *i.e.*, to the free surface region. Figure 45 presents an example of the formation of such microcrack in the segmentation of chips formed by metal cutting. Furthermore, the D_E variable is reduced due to straining under high triaxial stresses and negative lode parameter.

As the present phenomenon is very difficult to attest experimentally with the available techniques, it is impossible to observe microcracks dynamically formed in
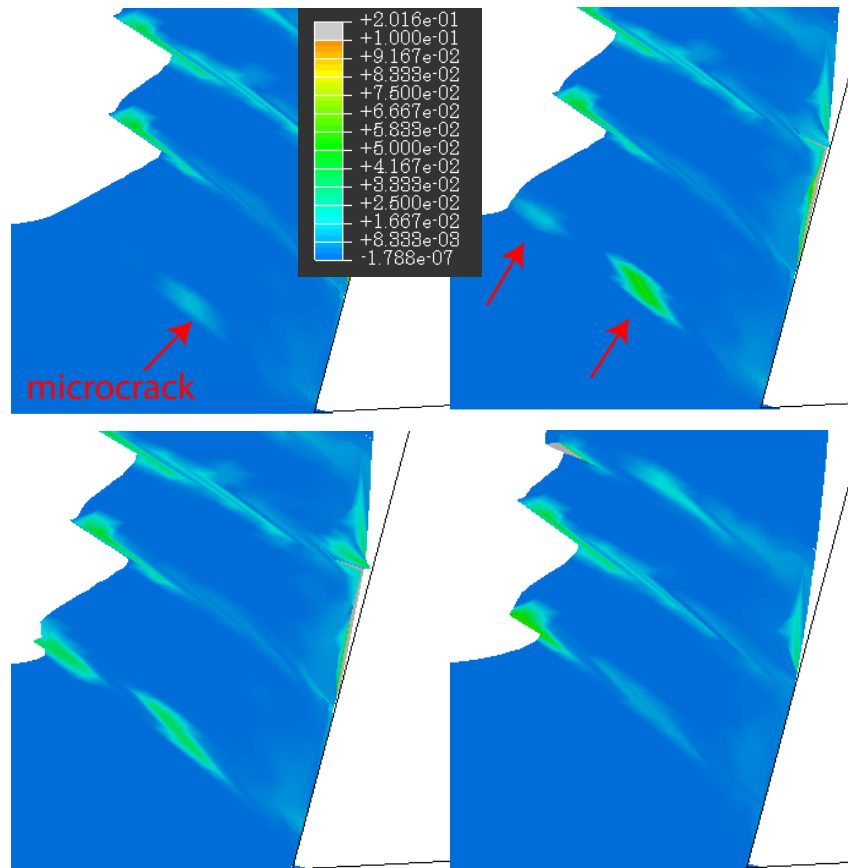
Figure 45 – Numerically obtained results of the evolution of a microcrack, represented by the D_E variable (color scale), across the shear plane of a chip. Fe$_3$Al with 50 m/s cutting speed and 0.327 feed rate

intermediate regions of the chip and closed due to compression after deformation in the shear plane in ductile materials. However, with materials with very limited ductility, such as Fe$_3$Al, some tensile cracks aren't fully welded and become enclosed inside the shear band. Figure 46 presents photographic evidence of this mechanism. The etching reveals the extension of the shear band and carbides, while also revealing microcracks enclosed inside the material across the shear bands.

These microcracks formed at intermediate regions of the chip propagate towards the shearing direction, and further, due to the non-monotonical nature of the D_E variable evolution, is constricted and "rewelded"due to compressive stresses. The ability of the model to simulate an event like this attests the complexity of the metal cutting process, on which the non monotonical nature of the elastoplastic degradation takes a fundamental part.
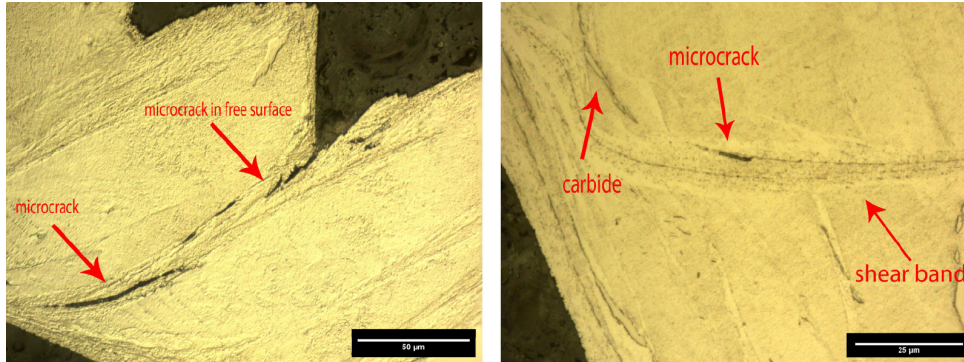
Figure 46 – Micrograph of enclosed cracks inside shear bands of Fe$_3$Al chips as predicted by the mechanism proposed by Shaw [18] in metal cutting and exemplified in Figure 45. Cutting speed is 50 m/min, 0.327 mm feed rate. Alloy A.

4.3 CUTTING FORCES IN Fe$_3$Al

4.3.1 Comparison between different compositions

The effects of alloy and tool geometry can be compared with respect to cutting forces. The comparison between cutting forces between tool T1 and T2 as the results of the cutting forces are illustrated in Figure 47. The results for both tools with different feeds are presented in Table 8.

Table 8 – Mean cutting forces, F_P, F_Q and F_x, and standard deviation of F_P forces for Tool T1 with alloys A and B. Cutting speed is 49.8 m min^{-1}

workpiece	feed	F_P	F_Q	F_x	F_P STD
A	0.205	33.532	35.370	19.215	3.921
B	0.205	27.920	25.807	14.519	14.613
A	0.327	44.149	43.007	20.462	8.727
B	0.327	36.328	35.459	18.266	19.425

*feeds in mm and forces in N.

From Table 8, for both feeds, and increase in F_P cutting forces when machining from Alloy A to alloy B. This is expected as the yield strength reduces with increase in ductility with the addition of Cr [81]. However, the effects of yield strength reduction cannot be attributed solely as the agent of cutting force reduction. An important feature, that made machining of alloy B nearly impossible, was that of high temperature. Tool breakage in 10 seconds or less in contact was present even during roughing operations. From the values of the standard deviation of the cutting force values in Table 8 and Figure 47, we can see that tool-workpiece-machining operations for Alloy B induced very high vibrations in the tool, which could be the cause, alongside tool tip softening, for tool breakage due to the brittleness of Co-WC-TiC tools. Figure 48 presents a photograph of the chip formation when cutting alloy B – from the radiating color, temperature

tool = T1, *feed* = 0.205 mm
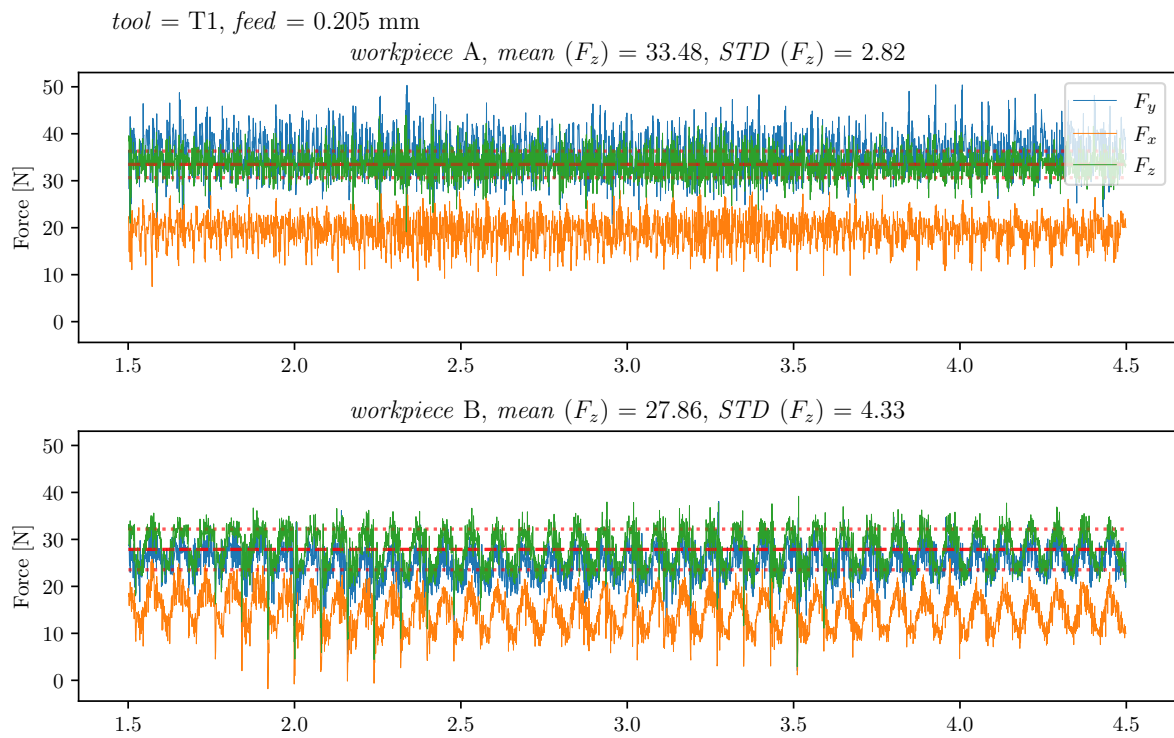
Figure 47 – Cutting forces, F_P, F_Q and F_x for A and B alloys with 0.205 mm feed

when cutting is very high, considering the low speed cutting regime and hardness, $(20 \, \mathrm{m\,s^{-1}})$ in this case.
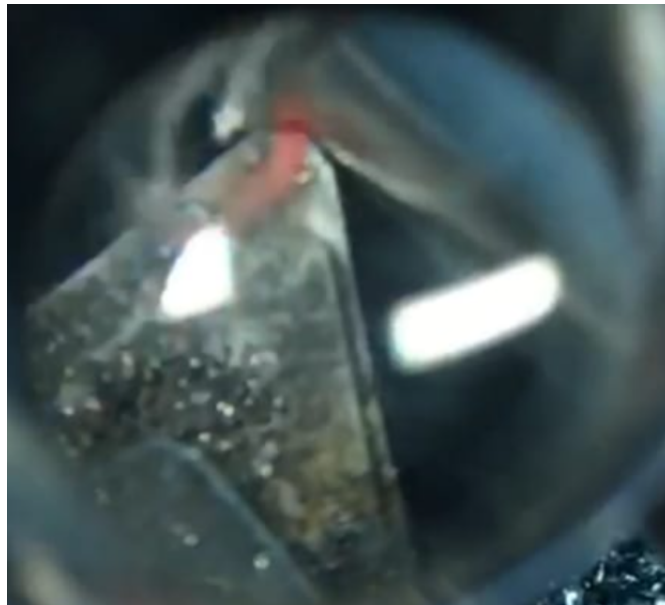
Figure 48 – High chip exit temperature when cutting Fe_3Al, $20 \, \mathrm{m\,s^{-1}}$, alloy B, 0.2mm feed, 1mm depth of cut

4.3.2 Comparison between different tools

The differences in tool geometry and rake angles were presented in subsection 3.1.2. This section will provide information regarding the different cutting tool geometries and resulting cutting forces. Table 9 and 9 presents the values of F_P, F_Q and F_x for T1 and T2 used for turning alloys A and B. As expected, F_x forces were higher for T2 in both cases, due to the higher oblique angle. While forces remanained somewhat constant for alloy A between T1 and T2 across both feeds, alloy B presented a high difference between both tools, with T2 being much higher, this can be attributed to the high wear rate of the TiN coated tool in this feed within the 3 seconds of tool contact. Furthermore, it is possible to observe a monotonic increase in cutting forces with cutting time, wich gives support to the "*instantaneous*" damage caused in the tool hypothesis, as shown in Figure 49

Table 9 – Cutting forces with tools T1 and T1, alloy A, *cutting speed*: 49.8 m min^{-1}

tool	feed	F_P	F_Q	F_x	F_P STD
T1	0.205	33.533	35.381	19.221	2.896
T2	0.205	33.992	33.784	19.816	2.736
T1	0.327	44.139	43.007	20.459	3.885
T2	0.327	45.590	40.962	23.253	4.225

*feeds in mm and forces in N

Table 10 – Cutting forces with tools T1 and T1, alloy B, *cutting speed*: 49.8 m min^{-1}

tool	feed	F_P	F_Q	F_x	F_P STD
T1	0.205	27.919	25.809	14.517	4.110
T2	0.205	43.473	39.136	40.573	2.964
T1	0.327	36.315	35.451	18.257	6.516
T2	0.327	43.103	44.360	31.354	3.922

*feeds in mm and forces in N.

In order to visualize the tool damage within the 3 second tool contact, a SEM photograph of the tool tip was analyzed. Figure 50 presents the results of tool damage in backscattered electrons (BSE) acquisition mode, in order to observe the limits between tool coating and substrate. The red arrow indicates an intense, $\approx 500 \text{ mm}$ wide, region of plastic deformation in T1 after 3 second contact in this feed, it is probable that, due the high temperatures achieved, tool tip softening with deformation and breakage occurs in very low contact time, leading to high cutting forces due to an unsharp broken tool.
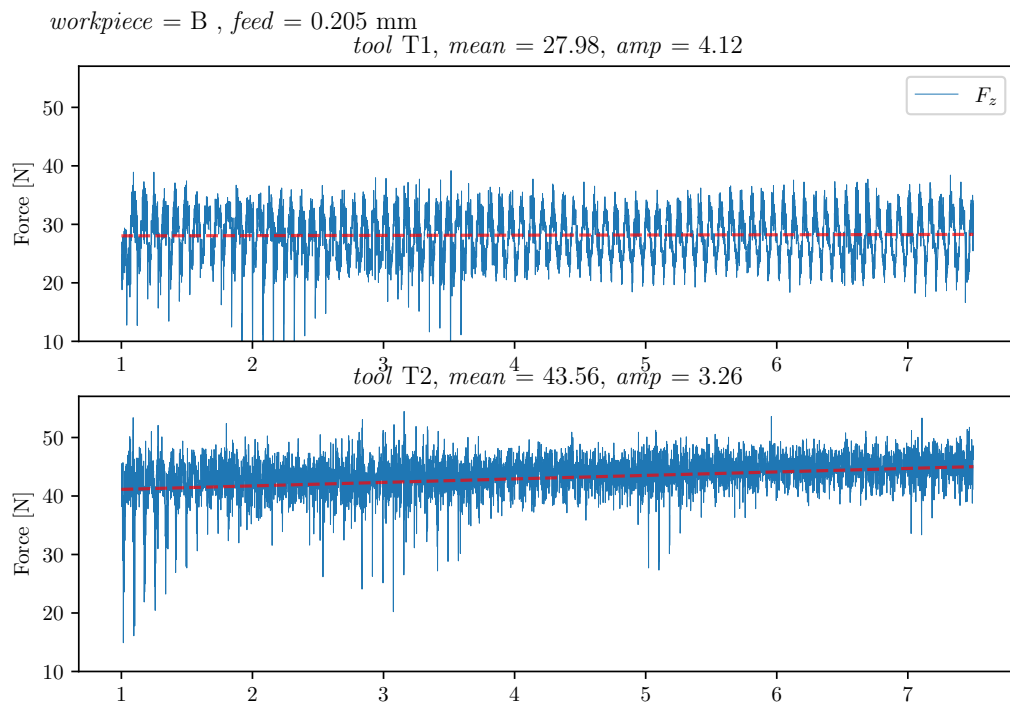
Figure 49 – Monotonically increasing forces after 2 seconds cutting time in T2 after contact. $0.327\,\mathrm{mm}$ **feed**, $49.8\,\mathrm{m\,min^{-1}}$ cutting speed
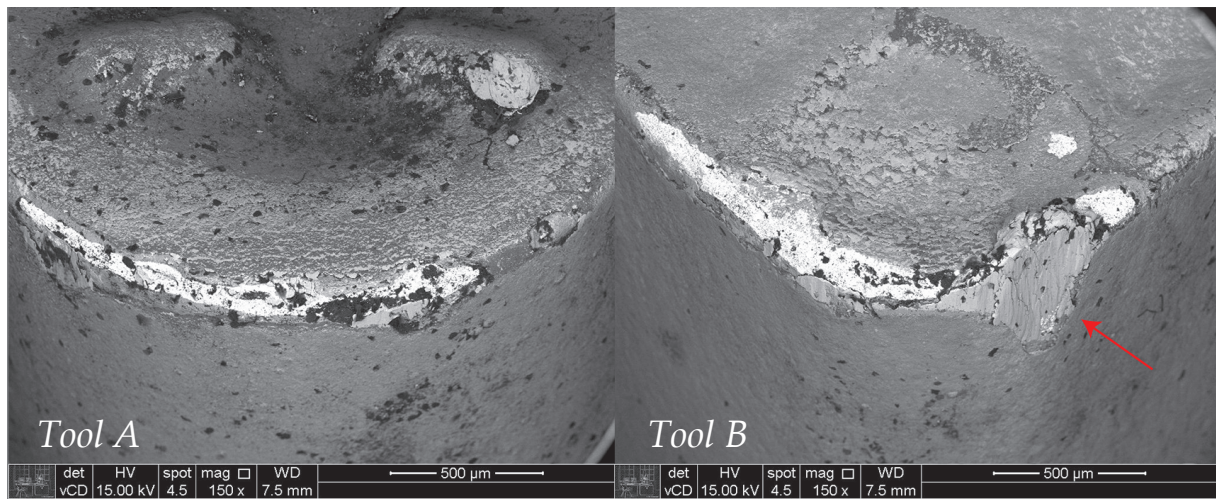
Figure 50 – T1 and T2 tool tip after 3 second contact in $0.205\,\mathrm{mm}$ **feed**, $49.76\,\mathrm{m\,min^{-1}}$ cutting speed, alloy B

4.4   CHIP FORMATION MECHANISM IN Fe₃Al

Chip formation in both alloys were studied according to chip morphology, hardness, micrographic chip root analysis with SEM and optical microscopy *via* metallography.

A transverse view of a chip was already presented in Figure 46, chips from both alloys are characterized by trapezoidal segments separated by long shear bands

containing cracks and, in alloy A, long carbides.

Chip roots characterized by metallographic inspection, produced with tool T1 are presented in Figure 51. For alloy A, chip formation involves the formation of long segments with alignment of carbides across the shear band, as shown in the region indicated by the arrow. Second phase particles, even hard ones, are known to provide crack initiation and strain localization sites in alloys [154, 155, 156, 20]. The hypothesis of the author is that the carbides provide means for the chip formation mechanism to avoid plastic deformation, which involves the production of high stresses and temperatures, and hence, high work associated to the chip formation. The carbides service most of the surface area in order to initiate cracks and sliding of the structure. If this is true, difference in shear band properties as length and/or hardness in microindentation tests in the shear band regions of boths alloys chips segments should provide evidence for this mechanism. The problem of shear band properties analysis arises from the fact that chip final hardness in the shear band region depends on the final temperature of the chip. In the case of alloy B, chip temperature was visually much higher than alloy A, which could cause annealing in the shear band region. Hence, special care should be taken when analyzing microindentation hardness in the shear band. Table 11 presents the mean values of chip segment length (h_s) and hardness in the shear band region as measures by microindentation.

Table 11 – Values of shear band hardness by microidentation, chip segment length, cutting ratio R_C and shear stress acting on the shear plane according to Piispanen's theory, for alloys A and B with tool T1

alloy	feed [mm]	hardness [HV]	segment length [µm]	R_C	τ_Z * [MPa]
A	0.205	448.9 ± 16.6	133.2 ± 63.4	0.70 ± 0.06	105.54
	0.327	448.6 ± 26.8	96.5 ± 32.5	0.76 ± 0.06	90.00
B	0.205	480.2 ± 24.0	64.5 ± 42.9	0.85 ± 0.02	137.84
	0.327	551.4 ± 38.8	32.9 ± 30.1	0.97 ± 0.01	112.51

indentation load HV0.1 (0.9807 N)

* τ_Z is an approximation *via* the orthogonal model, without the consideration of an F_x, the tool radius and the effects of second surface creation originated forces. Hence, the qualitative comparison between stresses must be kept in between the same feeds for both alloys.

An important evidence should consider the effects of chip segment length, if the chip formation mechanism involves the facilitation of shear band "*sliding*" due to second-phase particle strain localization, the chip segments should be longer in the case of the long-carbide-containing alloy A when comparing to the spheroidal carbide containing B, considering the same cutting regime. Segment length, as shown in Table 11 and the corresponding standard deviations, indicate that the average segment length is greater for the elongated carbide containing alloy A. The lower relative SD for the
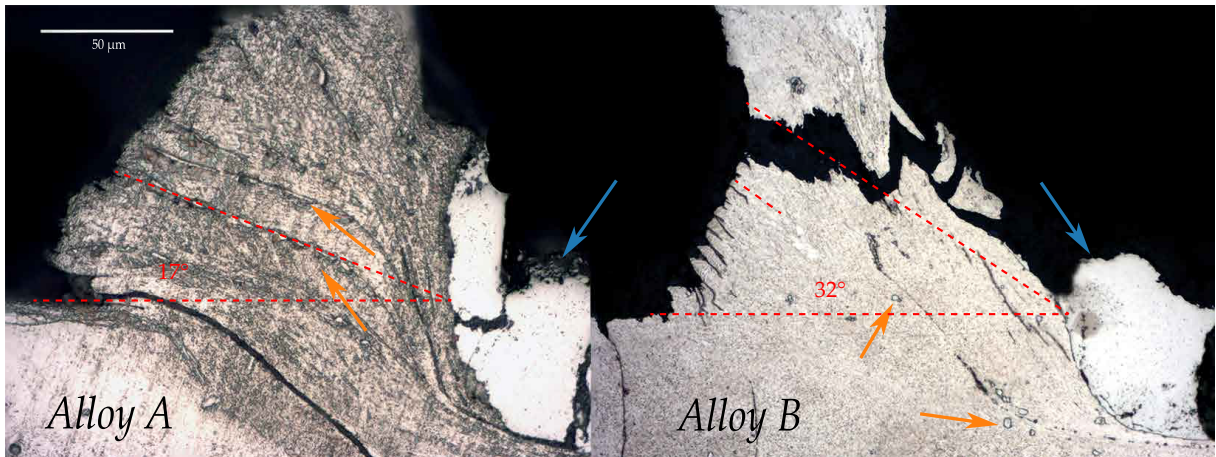
Figure 51 – Photomicrograph of chip roots produce by the *quick-stop* mechanism. Orange arrows indicate carbide particles, blue arrows indicate the tool tip

values of segment length in alloy A indicates a more grain orientation-indepedent chip formation mechanism, which is according to the given hypothesis of carbide-facilitated shear band. If long carbide particles facilitate the formation of shear bands, the grain orientation would be less determinant for the average chip formation mechanism. The orientation-dependence on the chip formation mechanism is shown in Figure 52, a much smoother transition and a more regular segment length is observed for alloy A.
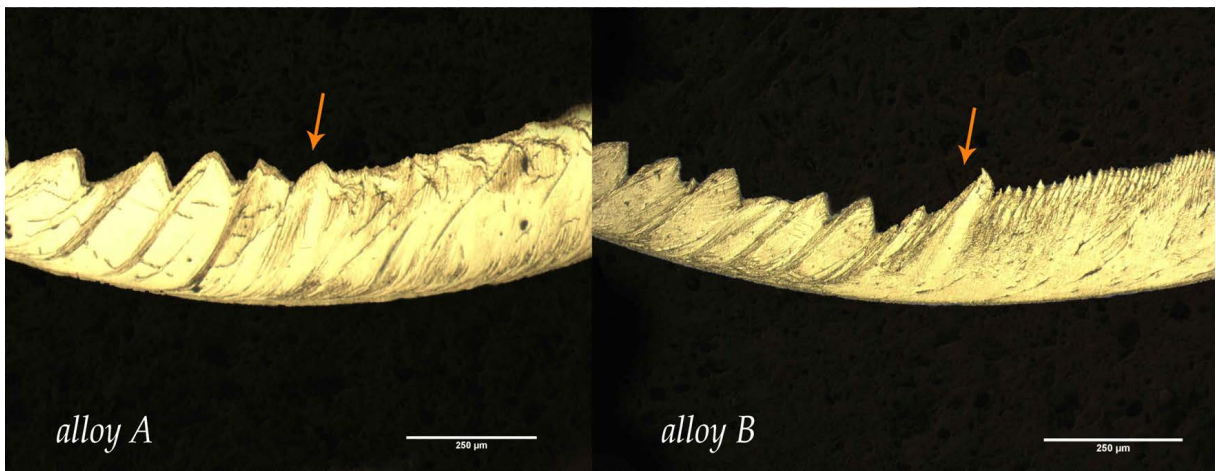
Figure 52 – Grain transition effect in chip formation mechanism for alloys A and B. 0.327 mm feed

The shear band microhardness of the chips of alloy A didn't show variation with feed. However, there was a high increase of hardness for alloy B. This can be explained by the change of chip cutting ratio, R_C. R_C indicates, along with chip root micrographs obtained *via* the *quick-stop* mechanism, the shear plane angle ϕ, that dictates the magnitude of shear deformation along the shear band, and hence, the final hardness of the deformed region. In the case of alloy A, chip R_C and *quick-stop* specimens indicate that shear remains constant with feed rate, while with alloy B, ϕ increases with feed rate. According to Morris; Dadras; Morris [157], addition of Cr actually reduces the work-

hardening magnitude of the alloy, which would bring a contradiction of interpretation of the results of higher hardness of alloy B's chips, with higher α and, hence, lower shear strain, according to the classical orthogonal machining model. Considering lower α, lower cutting temperatures and lower final chip hardness in alloy A, this further supports the hypothesis that the chip formation is facilitated by carbides with higher shape factor r_f.

The chip formation mechanism for alloys A and B are illustrated in Figure 53
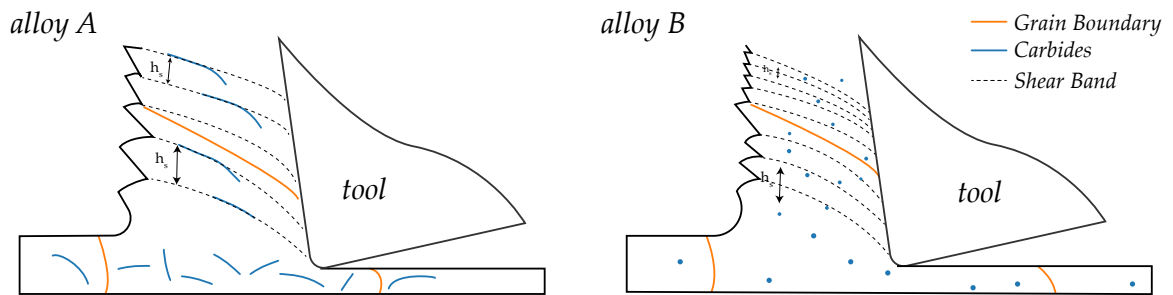
Figure 53 – Illustration of formation mechanisms for alloys A and B and the influence of carbide morphology in segment length

For alloy B, chip formation involves the formation of a higher ϕ shear band, with shorter segments and higher deformations and stresses. This is evident when comparing the τ_Z calculated in Table 11 in alloy A and B for the same feeds. The compositional effect of hardening are ruled out as indicated by the results of Yoshimi; Terashima; Hanada [158], which demonstrates the reduction of work-hardening for Fe$_3$Al alloys with additions of chromium. The result from the higher stresses when cutting alloy B is the high exit temperature produced when machining, which could be causing the premature failure of tools with fracture due to thermal softening.

5 CONCLUSION

The model presented in this work was successful in explaining the origin of chip segmentation and tensile ductile fracture of aluminium AA2024 T341 (a well fracture-characterized material) with only fracture mechanics considerations. A "thermal softening" factor, in this case, should only be used as an extension to the real root cause for segmentation in chip formation. The model is dependent of two independent variables: the Lode parameter and the triaxiality. The triaxiality and Lode parameter define the damage initiation of the material, as proposed on the work of [47], which can be defined as the critical strain on which the macro elastoplastic properties ($\bar{\sigma}_y$ and E) of the material begin to be affected by dimples or plastic flow disruptions. Furthermore, the Lode parameter defines the damage evolution across a certain stress-strain path, non monotonically with the D_E variable, and monotonically with the D_σ variable.

For instance, in the case of materials with very high ductilty, and specially high melting temperature, the thermal effects are needed to describe chip segmentation. The author used the example of the simulation of an austenitic stainless steel, AISI 304, which without thermal assumptions, the segmentation is absent. In this case, the thermal parameter in the Johnson-Cook model, θ_m, is strongly correlated to the advancement of the damage parameter of the current model, D_σ, and thermal softening aids the formation of the segment.

As previously stated, the D_E variable represents the elastic degradation imposed by a ductile tensile mode deformation, on which the growth and coalescence of voids gives origin to a new surface, and can be easily represented by characteristic dimples present in fractographies of ductile samples, such as those presented at Figure 22. Direct evidence of the D_E damage variable, which is associated with material separation and microcracking in chip formation mechanisms, were presented in Figures 45 and 46. Generally, D_σ variable is not easily observed, as the mechanism cannot be attested with most characterization techniques. However, the postulated mechanism is supported by the current work, both numerically and experimentally, and the results of Shaw Shaw [151] and Bridgman [50], regarding negative or negligible strain hardening exponents in very high strain regimes and the formation of shear bands in brittle materials, respectively, under high triaxial stresses. In addition, further supporting evidence is given by the presence of elongated dimples in conditions of shear strain in the corners of the cone of a ductile fracture as those schematically presented in Figure 22, and the distribution of the D_σ and DE variables across a cone fracture of a simple numerically obtained tensile test with the present model, such as presented in Figure 36. In addition, the results obtained by Courbon [118], regarding the correlation of material damage

with density, further adds support to the non-monotonic evolution of the D_E variable. Hence, the D_σ variable represents damage associated to the propagation of large flow disruptions manifested by long shear bands and material discontinuities. Direct photographic evidence from the outcome of the developed damage evolution model – the microcracking and rewelding in the shear plane, as predicted by the works of Shaw [151], associated with the D_E variable presented in our model – was presented in the case of a segmented chip formation of a Fe$_3$Alalloy in Figures 45 and 46.

Additionally, the results obtained by Guo; Compton; Chandrasekar [33] on the constant plastic strain at fracture in the segmentation region, which gives further support to the critical strain theory, is coherent with all the present simulations. In this case, the plastic strain at the onset of chip segmentation was approximately 0.93 in all cases where it's present, as shown in Figure 40.

The chip formation mechanism for alloys A and B are very characteristic and intrisically related to the carbide shapes. This was supported by the inspection of chip roots obtained by quick-stop mechanism, by the cutting ratio R_C and chip metallography. The assumption of carbide disposition in the alloy is also supported by modern literature for a mechanism of plastic localization and chip segmentation theory [30, 31, 156, 154]

5.1   Future works

An important step will be the simulation of the semi-orthogonal (turning) process of Fe$_3$Al with the newly developed damage evolution model. The forces measured with dynamometry must be approximate to the solution via FEM. The effect of carbide particles will be accounted in order to understand the underlying difference betweenvthe mechanisms envolving chip formation in both Fe$_3$Al alloys. The damage evolution parameters can be directly obtained directly via plane strain fracture tests, due to the low fracture toughness of the material.

Further study on the machinability of Fe$_3$Al in this work will focus on carbide shape control by heat-treatments by solubilization and slow cooling, in order to precipitate carbide in the matrix with the requiered shape factor. This can become a challenge due to the high stability of these transition metal carbides. Tool life testing along metallographic inspection will be an important part of the second part of this work, in order to provide a method for facilitating the machining of these alloys based on a pre-machining heat-treatment, which is present in many alloys, such as spheroidized high-carbon steels or the "solutionized" Inconel.

REFERENCES

[1]   MERCHANT, M. E. An Interpretive Look at the 20th Century on Modeling of Machining. **Machining Science and Technology**, v. 2, n. 2, p. 157–163, dez. 1998. ISSN 1091-0344, 1532-2483. DOI: `10.1080/10940349808945666`.

[2]   TRENT, Edward; WRIGHT, Paul. **Metal Cutting**. 4. ed. USA: Butterworth-Heinemann, 2000. ISBN 0-7506-7069-X.

[3]   ZHU, Dahu; ZHANG, Xiaoming; DING, Han. Tool Wear Characteristics in Machining of Nickel-Based Superalloys. **International Journal of Machine Tools and Manufacture**, v. 64, p. 60–77, jan. 2013. ISSN 08906955. DOI: `10.1016/j.ijmachtools.2012.08.001`.

[4]   HILL, R. The Mechanics of Machining: A New Approach. **Journal of the Mechanics and Physics of Solids**, v. 3, n. 1, p. 47–53, 1954.

[5]   SHAW, Milton C. **Metal Cutting Principles**. 2. ed. USA: Oxford University Press, 2005. ISBN 0-471-35929-7. DOI: `10.1037/023990`.

[6]   ASHBY, M. F. **Materials Selection in Mechanical Design**. 3rd ed. Amsterdam ; Boston: Butterworth-Heinemann, 2005. ISBN 978-0-7506-6168-3.

[7]   PIISPANEN, Väinö. Theory of Formation of Metal Chips. **Journal of Applied Physics**, v. 19, n. 10, p. 876–881, out. 1948. ISSN 0021-8979, 1089-7550.

[8]   MALLOCK, A. The Action of Cutting Tools. **Proceedings of the Royal Society of London**, v. 33, p. 127–139, 1882.

[9]   CHILDS, Thomas; MAEKAWA, Toshiyuki; OBIKAWA, Toshiyuki. **Metal Machining: Theory and Applications**. Grã-bretanha: Arnold, 2000.

[10] MACHADO, Alisson Rocha et al. Força e Potência de Usinagem. In: TEORIA da Usinagem dos Metais. 1. ed. São Paulo - SP: Edgar Blücher, 2009. P. 80.

[11] MERCHANT, M. Eugene. Mechanics of the Metal Cutting Process. I. Orthogonal Cutting and a Type 2 Chip. **Journal of Applied Physics**, v. 16, n. 5, p. 267–275, mai. 1945. ISSN 0021-8979, 1089-7550. DOI: `10.1063/1.1707586`.

[12] HASTINGS, W. F.; MATHEW, P.; OXLEY, P. L. B. A Machining Theory for Predicting Chip Geometry, Cutting Forces Etc. From Work Material Properties and Cutting Conditions. **Proceedings of the Royal Society A: Mathematical, Physical and Engineering Sciences**, v. 371, n. 1747, p. 569–587, ago. 1980. ISSN 1364-5021, 1471-2946. DOI: `10.1098/rspa.1980.0097`.

[13] SULAIMAN, S; ROSHAN, A; ARIFFIN, M K A. Finite Element Modelling of the Effect of Tool Rake Angle on Tool Temperature and Cutting Force during High Speed Machining of AISI 4340 Steel. **IOP Conference Series: Materials Science and Engineering**, v. 50, p. 012040, dez. 2013.

[14] HOLLOMON, H John. Tensile Deformation. **AMERICAN INSTITUTE OF MINING AND METALLURGICAL ENGINEERS**, 1879.

[15] LUDWIK, P. **Elemente der technologischen Mechanik.** Berlin: Springer, 1909.

[16] HIRTH, J. P. A Brief History of Dislocation Theory. **Metallurgical Transactions A**, v. 16, n. 12, p. 2085–2090, dez. 1985. ISSN 0360-2133, 1543-1940. DOI: 10.1007/BF02670413.

[17] FENTON, RG; OXLEY, PLB. Mechanics of Orthogonal Machining: Allowing for the Effects of Strain Rate and Temperature on Tool-Chip Friction. **Proceedings of the Institution of Mechanical Engineers**, SAGE Publications Sage UK: London, England, v. 183, n. 1, p. 417–438, 1968.

[18] SHAW, Milton C. A New Mechanism of Plastic Flow. **International Journal of Mechanical Sciences**, v. 22, n. 11, p. 673–686, jan. 1980. ISSN 00207403. DOI: 10.1016/0020-7403(80)90070-3. Disponível em: <https://linkinghub.elsevier.com/retrieve/pii/0020740380900703>. Acesso em: 2020-02-29.

[19] KOBAYASHI, S. et al. A Critical Comparison of Metal-Cutting Theories With New Experimental Data. **Journal of Engineering for Industry**, v. 82, n. 4, p. 333, 1960. ISSN 00220817. DOI: 10.1115/1.3664241.

[20] KOMANDURI, R.; BROWN, R. H. On the Mechanics of Chip Segmentation In Machining. **Journal of Engineering for Industry**, v. 103, n. 1, p. 33–33, 1981. DOI: 10.1115/1.3184458.

[21] PAWADE, R. S.; JOSHI, Suhas S. MECHANISM OF CHIP FORMATION IN HIGH-SPEED TURNING OF INCONEL 718. **Machining Science and Technology**, v. 15, n. 1, p. 132–152, abr. 2011. ISSN 1091-0344, 1532-2483. DOI: 10.1080/10910344.2011.557974.

[22] ITO, Satoshi et al. Machinability of Ni3AI-Based Intermetallic Compounds Materials Processing Technology. **Journal of Materials Processing Technology**, v. 63, n. 96, p. 181–186, 1997.

[23] KLOCKE, Fritz et al. High Performance Cutting of Gamma Titanium Aluminides: Influence of Lubricoolant Strategy on Tool Wear and Surface Integrity. **Wear**, v. 302, n. 1-2, p. 1136–1144, 2013. DOI: 10.1016/j.wear.2012.12.035.

[24] CALAMAZ, Madalina; COUPARD, Dominique; GIROT, Franck. A New Material Model for 2D Numerical Simulation of Serrated Chip Formation When Machining Titanium Alloy Ti–6Al–4V. **International Journal of Machine Tools and Manufacture**, v. 48, n. 3, p. 275–288, 2008. ISSN 0890-6955. DOI: `10.1016/j.ijmachtools.2007.10.014`. Disponível em: <`http://www.sciencedirect.com/science/article/pii/S0890695507002283`>. Acesso em: 2020-02-29.

[25] ANDRADE, U. et al. Dynamic Recrystallization in High-Strain, High-Strain-Rate Plastic Deformation of Copper. **Acta Metallurgica et Materialia**, v. 42, n. 9, p. 3183–3195, set. 1994. ISSN 0956-7151. DOI: `10.1016/0956-7151(94)90417-0`. Disponível em: <`http://www.sciencedirect.com/science/article/pii/0956715194904170`>. Acesso em: 2020-02-29.

[26] KOMANDURI, R.; SCHROEDER, T. A. On Shear Instability in Machining a Nickel-Iron Base Superalloy. **Journal of Engineering for Industry**, v. 108, n. 2, p. 93–100, mai. 1986. ISSN 0022-1817. DOI: `10.1115/1.3187056`. Disponível em: <`https://doi.org/10.1115/1.3187056`>. Acesso em: 2020-02-29.

[27] SHAW, M.C.; VYAS, A. Chip Formation in the Machining of Hardened Steel. **CIRP Annals - Manufacturing Technology**, v. 42, n. 1, p. 29–33, jan. 1993. ISSN 00078506. DOI: `10.1016/S0007-8506(07)62385-3`. Disponível em: <`https://linkinghub.elsevier.com/retrieve/pii/S0007850607623853`>. Acesso em: 2020-02-29.

[28] UEDA, Kanji; IWATA, Kazuaki; NAKAYAMA, Kazuo. Chip Formation Mechanism in Single Crystal Cutting of β-Brass. **CIRP Annals**, v. 29, n. 1, p. 41–46, jan. 1980. ISSN 0007-8506. DOI: `10.1016/S0007-8506(07)61292-X`. Disponível em: <`http://www.sciencedirect.com/science/article/pii/S000785060761292X`>. Acesso em: 2020-03-04.

[29] COOK, NH. Chip Formation in Machining Titanium. In: PROCEEDINGS of the Symposium on Machine Grind. Titanium, Watertown Arsenal, MA. 1953. P. 1–7.

[30] KOMANDURI, R.; VON TURKOVICH, B.F. New Observations on the Mechanism of Chip Formation When Machining Titanium Alloys. **Wear**, v. 69, n. 2, p. 179–188, jun. 1981. ISSN 00431648. DOI: `10.1016/0043-1648(81)90242-8`. Disponível em: <`https://linkinghub.elsevier.com/retrieve/pii/0043164881902428`>. Acesso em: 2020-02-29.

[31] VYAS, A.; SHAW, M. C. Mechanics of Saw-Tooth Chip Formation in Metal Cutting. **Journal of Manufacturing Science and Engineering**, v. 121, n. 2, p. 163–172, mai. 1999. ISSN 1087-1357. DOI: `10.1115/1.2831200`. Disponível em: <`https://asmedigitalcollection.asme.org/manufacturingscience/article/121/2/163/420796/Mechanics-of-Saw-Tooth-Chip-Formation-in-Metal`>. Acesso em: 2020-06-20.

[32] MABROUKI, Tarek et al. Numerical and Experimental Study of Dry Cutting for an Aeronautic Aluminium Alloy (A2024-T351). **International Journal of Machine Tools and Manufacture**, v. 48, n. 11, p. 1187–1197, 2008. ISSN 0890-6955. DOI: `10.1016/j.ijmachtools.2008.03.013`. Disponível em: <`http://www.sciencedirect.com/science/article/pii/S0890695508000631`>. Acesso em: 2020-06-01.

[33] GUO, Yang; COMPTON, W. Dale; CHANDRASEKAR, Srinivasan. In Situ Analysis of Flow Dynamics and Deformation Fields in Cutting and Sliding of Metals. **Proceedings of the Royal Society A: Mathematical, Physical and Engineering Sciences**, v. 471, n. 2178, p. 20150194, jun. 2015. ISSN 1364-5021, 1471-2946. DOI: `10.1098/rspa.2015.0194`. Disponível em: <`https://royalsocietypublishing.org/doi/10.1098/rspa.2015.0194`>. Acesso em: 2020-02-05.

[34] CHAGAS, G.M.P.; MACHADO, I.F. Numerical Model of Machining Considering the Effect of MnS Inclusions in an Austenitic Stainless Steel. **Procedia CIRP**, v. 31, p. 533–538, 2015. ISSN 22128271. DOI: `10.1016/j.procir.2015.04.093`.

[35] ARGYRIS, J. H; KELSEY, S. **Energy Theorems and Structural Analysis: A Generalised Discourse with Applications on Energy Principles of Structural Analysis Including the Effects of Temperature and Non-Linear Stress-Strain Relations**. Edição: Butterworth. New York, US, 1960. ISBN 978-1-4899-5850-1.

[36] CASSEL, Kevin W. **Variational Methods with Applications in Science and Engineering**. Edição: Cambridge University Press. Cambridge, 2013.

[37] FUHRER, R. S.; ROMANYK, D. L.; CAREY, J. P. A Comparative Finite Element Analysis of Maxillary Expansion with and without Midpalatal Suture Viscoelasticity Using a Representative Skeletal Geometry. **Scientific Reports**, v. 9, n. 1, p. 8476, dez. 2019. ISSN 2045-2322.

[38] KENNAWAY, Richard; COEN, Enrico. Volumetric Finite-Element Modelling of Biological Growth. **Open Biology**, v. 9, n. 5, p. 190057, mai. 2019. ISSN 2046-2441, 2046-2441. DOI: `10.1098/rsob.190057`.

[39] DOUGLAS, A. Finite Elements for Geological Modelling. **Nature**, v. 226, p. 630–631, mai. 1970.

[40] ZIENKIEWICZ, Olgierd C.; TAYLOR, Robert L.; ZHU, Jianzhong. The Structural Element and the Structural System. In: THE Finite Element Method. Vol. 1: Its Basis and Fundamentals. 6. ed., repr. Amsterdam: Elsevier Butterworth-Heinemann, 2010. P. 3–5. ISBN 978-0-7506-6320-5.

[41] ARRAZOLA, P. J. et al. Serrated Chip Prediction in Finite Element Modeling of the Chip Formation Process. **Machining Science and Technology**, v. 11, n. 3, p. 367–390, set. 2007. ISSN 1091-0344. DOI: `10.1080/10910340701539882`. Disponível em: <`https://www.tandfonline.com/doi/abs/10.1080/10910340701539882`>. Acesso em: 28 nov. 2022.

[42] DUTT, R. P.; BREWER, R. C. ON THE THEORETICAL DETERMINATION OF THE TEMPERATURE FIELD IN ORTHOGONAL MACHINING. **International Journal of Production Research**, v. 4, n. 2, p. 91–114, jan. 1965. ISSN 0020-7543, 1366-588X. DOI: `10.1080/00207546508919968`.

[43] BAO, H.; STEVENSON, M.G. An Investigation of Built-up Edge Formation in the Machining of Aluminium. **International Journal of Machine Tool Design and Research**, v. 16, n. 3, p. 165–178, jan. 1976. ISSN 00207357. DOI: `10.1016/0020-7357(76)90002-0`.

[44] ROTH, R. N.; OXLEY, P. L. B. Slip-Line Field Analysis for Orthogonal Machining Based upon Experimental Flow Fields. **Journal of Mechanical Engineering Science**, v. 14, n. 2, p. 85–97, abr. 1972. ISSN 0022-2542, 2058-3389. DOI: `10.1243/JMES_JOUR_1972_014_015_02`.

[45] IRGENS, Fridtjov. **Continuum Mechanics**. Norway: Springer Science & Business Media, 2008.

[46] BONSACK, François. Invariance as a Criterion of Reality. **Dialectica**, v. 31, n. 3-4, p. 313–331, 1977.

[47] BAI, Yuanli; WIERZBICKI, Tomasz. A New Model of Metal Plasticity and Fracture with Pressure and Lode Dependence. **International Journal of Plasticity**, v. 24, n. 6, p. 1071–1096, 2008. ISSN 0749-6419. DOI: `10.1016/j.ijplas.2007.09.004`. Disponível em: <`http://www.sciencedirect.com/science/article/pii/S0749641907001246`>. Acesso em: 2020-03-04.

[48] TRESCA, Henri. **Complément au Mémoire sur l'écoulement des corps solides**. Imprimerie nationale, 1869.

[49] MISES, R v. Mechanik Der Festen Körper Im Plastisch-Deformablen Zustand. **Nachrichten von der Gesellschaft der Wissenschaften zu Göttingen, Mathematisch-Physikalische Klasse**, v. 1913, p. 582–592, 1913.

[50] BRIDGMAN, Percy Williams. **Studies in large plastic flow and fracture**. Cambridge, Massachusetts: Harvard University Press, 1964.

[51] HAIGH, Bernard Parker. The strain energy function and the elastic limit. **Engineering**, v. 109, p. 158–160, 1920.

[52] CHAWLA, K. K.; MEYERS, Marc. **Mechanical Behavior of Materials**. Edição: Cambridge University Press. 2. ed. Cambridge, 2009. ISBN 978-0-521-86675-0.

[53] THOMPSON, Joseph O. Hooke's Law. **Science**, American Association for the Advancement of Science, v. 64, n. 1656, p. 298–299, 1926.

[54] CENTORE, F F. **The Mechanics of Terrestrial Local Motions**. The Hague, Netherlands: Springer Netherlands, 1970.

[55] SLAUGHTER, William S. Constitutive Equations. In: THE Linearized Theory of Elasticity. 2013. P. 193. ISBN 978-1-4612-6608-2.

[56] SCHMID, E; BOAS, W. Elasticity of Crystals. In: PLASTICITY of Crystals - With Special Reference to Metals. 1. ed.: F. A. Hughes & CO. Limited, 1935. P. 14. DOI: 10.1038/1351076b0.

[57] ALKAN, S.; WU, Y.; SEHITOGLU, H. Giant Non-Schmid Effect in NiTi. **Extreme Mechanics Letters**, v. 15, p. 38–43, set. 2017. ISSN 2352-4316. DOI: 10.1016/j.eml.2017.05.003.

[58] FRENKEL, JA. Zur Theorie Der Elastizitätsgrenze Und Der Festigkeit Kristallinischer Körper. **Zeitschrift für Physik**, v. 37, n. 7-8, p. 572–609, 1926.

[59] EWING, James Alfred; ROSENHAIN, Walter. The Crystalline Structure of Metals. **Proceedings of the Royal Society of London**, v. 65, n. 413-422, p. 172–177, 1900.

[60] _____. The Crystalline Structure of Metals II. **Philosophical Transactions of the Royal Society of London. Series A, Containing Papers of a Mathematical or Physical Character**, v. 195, n. 262-273, p. 279–301, 1900.

[61] CEDERGREN, S.; PETTI, G.; SJÖBERG, G. On the Influence of Work Material Microstructure on Chip Formation, Cutting Forces and Acoustic Emission When Machining Ti-6Al-4V. **Procedia CIRP**, v. 12, p. 55–60, jan. 2013. ISSN 2212-8271. DOI: 10.1016/j.procir.2013.09.011. Disponível em: <http://www.sciencedirect.com/science/article/pii/S2212827113006525>. Acesso em: 2020-03-08.

[62] ANTOLOVICH, Stephen D; ARMSTRONG, Ronald W. Plastic Strain Localization in Metals: Origins and Consequences. **Progress in Materials Science**, v. 59, p. 1–160, 2014.

[63] DODD, Bradley; BAI, Yilong. **Adiabatic Shear Localization: Frontiers and Advances**. Elsevier, 2012.

[64] PURSCHE, F; MEYER, LW. Correlation between Dynamic Material Behavior and Adiabatic Shear Phenomenon for Quenched and Tempered Steels. **Engineering transactions**, v. 59, n. 2, p. 67–84, 2011.

[65] MEDYANIK, S; LIU, W; LI, S. On Criteria for Dynamic Adiabatic Shear Band Propagation. **Journal of the Mechanics and Physics of Solids**, v. 55, n. 7, p. 1439–1461, jul. 2007. ISSN 00225096. DOI: 10.1016/j.jmps.2006.12.006.

[66] SCHOENFELD, S. E.; WRIGHT, T. W. A Failure Criterion Based on Material Instability. **International Journal of Solids and Structures**, v. 40, n. 12, p. 3021–3037, jun. 2003. ISSN 0020-7683. DOI: 10.1016/S0020-7683(03)00059-3.

[67] HARZALLAH, Mahmoud et al. Numerical and Experimental Investigations of Ti-6Al-4V Chip Generation and Thermo-Mechanical Couplings in Orthogonal Cutting. **International Journal of Mechanical Sciences**, v. 134, p. 189–202, dez. 2017. ISSN 00207403. DOI: 10.1016/j.ijmecsci.2017.10.017. Disponível em: <https://linkinghub.elsevier.com/retrieve/pii/S0020740317308913>. Acesso em: 2020-08-03.

[68] HOU, Zhen Bing; KOMANDURI, Ranga. Modeling of Thermomechanical Shear Instability in Machining. **International Journal of Mechanical Sciences**, v. 39, n. 11, p. 1273–1314, nov. 1997. ISSN 00207403. DOI: 10.1016/S0020-7403(97)00017-9. Disponível em: <https://linkinghub.elsevier.com/retrieve/pii/S0020740397000179>. Acesso em: 2020-02-29.

[69] KOUADRI, S. et al. Quantification of the Chip Segmentation in Metal Machining: Application to Machining the Aeronautical Aluminium Alloy AA2024-T351 with Cemented Carbide Tools WC-Co. **International Journal of Machine Tools and Manufacture**, v. 64, p. 102–113, jan. 2013. ISSN 0890-6955. DOI: 10.1016/j.ijmachtools.2012.08.006. Disponível em: <http://www.sciencedirect.com/science/article/pii/S0890695512001708>. Acesso em: 2020-06-01.

[70] RAZANICA, S et al. FE Modeling and Simulation of Machining Alloy 718 Based on Ductile Continuum Damage. **International Journal of Mechanical Sciences**, v. 171, p. 105375, abr. 2020. ISSN 00207403. DOI: 10.1016/j.ijmecsci.2019.105375.

[71] COCKCROFT, MG; LATHAM, DJ et al. Ductility and the Workability of Metals. **J Inst Metals**, v. 96, n. 1, p. 33–39, 1968.

[72] THOMASON, P F. **Ductile fracture of metals**. Pergamon Press, 1990. P. 219.

[73] LEMAITRE, Jean. Coupled Elasto-Plasticity and Damage Constitutive Equations. **Computer methods in applied mechanics and engineering**, v. 51, n. 1-3, p. 31–49, 1985.

[74] _____._____. **Computer Methods in Applied Mechanics and Engineering**, v. 51, n. 1, p. 31–49, set. 1985. ISSN 0045-7825. DOI: 10.1016/0045-7825(85)90026-X.

[75] SOWERBY, R.; CHANDRASEKARAN, N. A Proposal for the Onset of Chip Segmentation in Machining. **Materials Science and Engineering: A**, v. 119, p. 219–229, nov. 1989. ISSN 0921-5093. DOI: 10.1016/0921-5093(89)90541-8. Disponível em: <http://www.sciencedirect.com/science/article/pii/0921509389905418>. Acesso em: 2020-08-09.

[76] STOLOFF, N. S.; LIU, C. T.; DEEVI, S. C. Emerging Applications of Intermetallics. **Intermetallics**, v. 8, n. 9-11, p. 1313–1320, 2000. DOI: 10.1016/S0966-9795(00)00077-7.

[77] LIU, CT; LEE, EH; MCKAMEY, CG. An Environmental Effect as the Major Cause for Room-Temperature Embrittlement in FeAl. **Scripta metallurgica**, Elsevier, v. 23, n. 6, p. 875–880, 1989.

[78] CT, Liu et al. Environmental Embrittlement in FeAl Aluminides. **Isij International**, The Iron and Steel Institute of Japan, v. 31, n. 10, p. 1192–1200, 1991.

[79] YOO, M H; FU, C L. Cleavage Fracture of Ordered Intermetallic Alloys, p. 9.

[80] ZAMANZADE, Mohammad; BARNOUSH, Afrooz; MOTZ, Christian. A Review on the Properties of Iron Aluminide Intermetallics. **Crystals**, v. 6, n. 1, p. 10, 2016. DOI: 10.3390/cryst6010010.

[81] MCKAMEY, C. G.; HORTON, J. A.; LIU, C. T. Effect of Chromium on Properties of Fe3Al. **Journal of Materials Research**, Cambridge University Press, v. 4, n. 5, p. 1156–1163, out. 1989. ISSN 2044-5326, 0884-2914. DOI: 10.1557/JMR.1989.1156.

[82] STOLOFF, No S; LIU, CT. Environmental Embrittlement of Iron Aluminides. **Intermetallics**, Elsevier, v. 2, n. 2, p. 75–87, 1994.

[83] ALVEN, D. A; STOLOFF, N. S. The Influence of Composition on the Environmental Embrittlement of Fe3Al Alloys. **Materials Science and Engineering: A**, v. 239–240, p. 362–368, dez. 1997. ISSN 0921-5093. DOI: 10.1016/S0921-5093(97)00604-7.

[84] DENKENA, B. et al. Chip Formation and Modeling of Dynamic Force Behavior in Machining Polycrystalline Iron-Aluminum. **Production Engineering**, v. 8, n. 3, p. 273–282, 2014. ISSN 1174001305200. DOI: 10.1007/s11740-013-0520-0.

[85] VILLAGOMEZ-GALINDO, M. et al. Casting Fe–Al-based Intermetallics Alloyed with Li and Ag. **Journal of Materials Research**, v. 31, n. 16, p. 2473–2481, ago. 2016. ISSN 0884-2914, 2044-5326. DOI: 10.1557/jmr.2016.249.

[86] RAMIREZ, Bruna N.; SCHÖN, Cláudio G. Casting of Iron Aluminides. **Journal of Phase Equilibria and Diffusion**, v. 38, n. 3, p. 288–297, 2017. ISSN 15477037. DOI: 10.1007/s11669-017-0539-6.

[87] JOHNSON, Gordon R; COOK, William H. A Constitutive Model and Data for Metals Subjected to Large Strains, High Strain Rates and High Temperatures. In: PROCEEDINGS of the 7th International Symposium on Ballistics. 1983. v. 21, p. 541–547.

[88] MIRZAIE, Tina; MIRZADEH, Hamed; CABRERA, Jose-Maria. A simple Zerilli–Armstrong constitutive equation for modeling and prediction of hot deformation flow stress of steels. en. **Mechanics of Materials**, v. 94, p. 38–45, mar. 2016. ISSN 0167-6636. DOI: 10.1016/j.mechmat.2015.11.013. Disponível em: <https://www.sciencedirect.com/science/article/pii/S0167663615002550>. Acesso em: 22 nov. 2022.

[89] MORRIS, D. G.; PEGUIRON, D.; NAZMY, M. Yield Stress and Stress Anomaly in an Fe3Al Alloy. **Philosophical Magazine A**, Taylor & Francis, v. 71, n. 2, p. 441–463, fev. 1995. ISSN 0141-8610. DOI: 10.1080/01418619508244368.

[90] LEAMY, H. J.; KAYSER, F. X. The Compressive Deformation Behavior of Long Range Ordered Polycrystalline Iron—Aluminum Alloys. **physica status solidi (b)**, v. 34, n. 2, p. 765–780, 1969. ISSN 1521-3951. DOI: 10.1002/pssb.19690340240.

[91] DENKENA, Berend et al. Chip Formation in Monocrystalline Iron-Aluminum. **CIRP Journal of Manufacturing Science and Technology**, v. 7, n. 2, p. 71–82, 2014. ISSN 17555817. DOI: 10.1016/j.cirpj.2014.01.004.

[92] REDDY, J N. Introduction. In: AN Introduction to the Finite Element Method. 3. ed.: McGraw-Hill Education, 2005. P. 13.

[93] _____. **An Introduction to the Finite Element Method**. 3. ed.: McGraw-Hill Education, 2005.

[94] SYSTÈMES, Dassault. ABAQUS 6.14 Analysis User's Manual. **Dassault Systems Inc Waltham, USA**, 2014.

[95] ARRAZOLA, Pedro J.; ÖZEL, Tugrul. Investigations on the Effects of Friction Modeling in Finite Element Simulation of Machining. **International Journal of Mechanical Sciences**, v. 52, n. 1, p. 31–42, jan. 2010. ISSN 0020-7403. DOI: `10.1016/j.ijmecsci.2009.10.001`.

[96] ÖZEL, Tugrul. The Influence of Friction Models on Finite Element Simulations of Machining. **International Journal of Machine Tools and Manufacture**, v. 46, n. 5, p. 518–530, abr. 2006. ISSN 0890-6955. DOI: `10.1016/j.ijmachtools.2005.07.001`. Disponível em: <`http://www.sciencedirect.com/science/article/pii/S0890695505001550`>. Acesso em: 2020-06-06.

[97] HOLLOMON, John H. Tensile Deformation. **Aime Trans**, v. 12, n. 4, p. 1–22, 1945.

[98] JOHNSON, Gordon R.; COOK, William H. Fracture Characteristics of Three Metals Subjected to Various Strains, Strain Rates, Temperatures and Pressures. **Engineering Fracture Mechanics**, v. 21, n. 1, p. 31–48, jan. 1985. ISSN 00137944. DOI: `10.1016/0013-7944(85)90052-9`. Disponível em: <`https://linkinghub.elsevier.com/retrieve/pii/0013794485900529`>. Acesso em: 2020-02-28.

[99] FARREN, William Scott; TAYLOR, Geoffrey Ingram. The heat developed during plastic extension of metals. **Proceedings of the Royal Society of London. Series A, Containing Papers of a Mathematical and Physical Character**, v. 107, n. 743, p. 422–451, mar. 1925. DOI: `10.1098/rspa.1925.0034`. Disponível em: <`https://royalsocietypublishing.org/doi/10.1098/rspa.1925.0034`>. Acesso em: 22 nov. 2022.

[100] TAYLOR, Geoffrey Ingram; QUINNEY, H. The latent energy remaining in a metal after cold working. **Proceedings of the Royal Society of London. Series A, Containing Papers of a Mathematical and Physical Character**, v. 143, n. 849, p. 307–326, jan. 1934. DOI: `10.1098/rspa.1934.0004`. Disponível em: <`https:`

//royalsocietypublishing.org/doi/10.1098/rspa.1934.0004>.
Acesso em: 22 nov. 2022.

[101] WILKINS, M.L.; STREIT, R.D.; REAUGH, J.E. **Cumulative-Strain-Damage Model of Ductile Fracture: Simulation and Prediction of Engineering Fracture Tests**. Out. 1980. ucrl–53058, 6628920. DOI: 10.2172/6628920. Disponível em: <http://www.osti.gov/servlets/purl/6628920-KUgBmG/>. Acesso em: 2020-03-04.

[102] RICE, J. R.; TRACEY, D. M. On the Ductile Enlargement of Voids in Triaxial Stress Fields. **Journal of the Mechanics and Physics of Solids**, v. 17, n. 3, p. 201–217, jun. 1969. ISSN 0022-5096. DOI: 10.1016/0022-5096(69)90033-7. Disponível em: <http://www.sciencedirect.com/science/article/pii/0022509669900337>. Acesso em: 2020-03-08.

[103] ZHU, Yazhi; ENGELHARDT, Michael D.; KIRAN, Ravi. Combined Effects of Triaxiality, Lode Parameter and Shear Stress on Void Growth and Coalescence. **Engineering Fracture Mechanics**, v. 199, p. 410–437, ago. 2018. ISSN 0013-7944. DOI: 10.1016/j.engfracmech.2018.06.008.

[104] BARSOUM, Imad; FALESKOG, Jonas. Micromechanical Analysis on the Influence of the Lode Parameter on Void Growth and Coalescence. **International Journal of Solids and Structures**, v. 48, n. 6, p. 925–938, mar. 2011. ISSN 0020-7683. DOI: 10.1016/j.ijsolstr.2010.11.028.

[105] NIELSEN, Chris V; MARTINS, Paulo AF. **Metal Forming: Formability, Simulation, and Tool Design**. Academic Press, 2021.

[106] SRIVASTAVA, A.; NEEDLEMAN, A. Void Growth versus Void Collapse in a Creeping Single Crystal. **Journal of the Mechanics and Physics of Solids**, v. 61, n. 5, p. 1169–1184, mai. 2013. ISSN 0022-5096. DOI: 10.1016/j.jmps.2013.01.006.

[107] HARZALLAH, M. et al. Thermomechanical Coupling Investigation in Ti-6Al-4V Orthogonal Cutting: Experimental and Numerical Confrontation. **International Journal of Mechanical Sciences**, v. 169, p. 105322, mar. 2020. ISSN 00207403. DOI: 10.1016/j.ijmecsci.2019.105322. Disponível em: <https://linkinghub.elsevier.com/retrieve/pii/S0020740319305909>. Acesso em: 2020-08-03.

[108] HILLERBORG, Arne; MODÉER, Mats; PETERSSON, P-E. Analysis of Crack Formation and Crack Growth in Concrete by Means of Fracture Mechanics and Finite Elements. **Cement and concrete research**, v. 6, n. 6, p. 773–781, 1976.

[109] BARENBLATT, Grigory Isaakovich et al. The Mathematical Theory of Equilibrium Cracks in Brittle Fracture. **Advances in applied mechanics**, v. 7, n. 1, p. 55–129, 1962.

[110] BUCHKREMER, S; KLOCKE, F; LUNG, D. Analytical Study on the Relationship between Chip Geometry and Equivalent Strain Distribution on the Free Surface of Chips in Metal Cutting. **International Journal of Mechanical Sciences**, v. 85, p. 88–103, ago. 2014. ISSN 00207403. DOI: 10.1016/j.ijmecsci.2014.05.005. Disponível em: <https://linkinghub.elsevier.com/retrieve/pii/S0020740314001775>. Acesso em: 2020-08-03.

[111] LEMAITRE, Jean. **A Course on Damage Mechanics**. Springer Science & Business Media, 2012.

[112] YEH, Hung-Yang; CHENG, Jung-Ho. NDE of Metal Damage: Ultrasonics with a Damage Mechanics Model. **International Journal of Solids and Structures**, v. 40, n. 26, p. 7285–7298, 2003.

[113] JONES, D. L.; CHISHOLM, D. B. An Investigation of the Edge-Sliding Mode in Fracture Mechanics. **Engineering Fracture Mechanics**, v. 7, n. 2, p. 261–270, jun. 1975. ISSN 0013-7944. DOI: 10.1016/0013-7944(75)90007-7. Disponível em: <http://www.sciencedirect.com/science/article/pii/0013794475900077>. Acesso em: 2020-06-03.

[114] SHI, Y. W.; ZHOU, N. N.; ZHANG, J. X. Comparison of Mode I and Mode II Elastic-Plastic Fracture Toughness for Two Low Alloyed High Strength Steels. **International Journal of Fracture**, v. 68, n. 1, p. 89–97, 1994. ISSN 0376-9429, 1573-2673. DOI: 10.1007/BF00032328. Disponível em: <http://link.springer.com/10.1007/BF00032328>. Acesso em: 2020-06-04.

[115] MOGI, Kiyoo. Fracture and Flow of Rocks under High Triaxial Compression. **Journal of Geophysical Research**, v. 76, n. 5, p. 1255–1269, fev. 1971. ISSN 01480227. DOI: 10.1029/JB076i005p01255. Disponível em: <http://doi.wiley.com/10.1029/JB076i005p01255>. Acesso em: 2020-08-10.

[116] ROBERTSON, Eugene C. Experimental Study of the Strength of Rocks. **GSA Bulletin**, v. 66, n. 10, p. 1275–1314, out. 1955. ISSN 0016-7606. DOI: 10.1130/0016-7606(1955)66[1275:ESOTSO]2.0.CO;2. Disponível em: <https://pubs.geoscienceworld.org/gsa/gsabulletin/article/66/10/1275/4665/EXPERIMENTAL-STUDY-OF-THE-STRENGTH-OF-ROCKS>. Acesso em: 2020-08-10.

[117] BROBERG, KB. On Crack Paths. **Engineering Fracture Mechanics**, v. 28, n. 5-6, p. 663–679, 1987.

[118] COURBON, Joël. Damage evolution in a compressive forming process: ironing of beverage cans. en. **Scripta Materialia**, v. 48, n. 11, p. 1519–1524, jun. 2003. ISSN 1359-6462. DOI: 10.1016/S1359-6462(03)00131-3. Disponível em: <https://www.sciencedirect.com/science/article/pii/S1359646203001313>. Acesso em: 22 nov. 2022.

[119] MISCIONE, Juan Manuel Costa; RAMIREZ, Bruna Niccoli; SCHÖN, Claudio Geraldo. A ductile damage evolution model for the simulation of machining processes in materials with limited ductility. en. **Engineering Fracture Mechanics**, v. 271, p. 108602, ago. 2022. ISSN 0013-7944. DOI: 10.1016/j.engfracmech.2022.108602. Disponível em: <https://www.sciencedirect.com/science/article/pii/S0013794422003332>. Acesso em: 22 nov. 2022.

[120] SAUTHOFF, Gerhard. Historical Remarks. In: INTERMETALLICS. 1. ed. Weinheim, Alemanha: VCH Verlagsgesellschaft, 1995. P. 2–5. ISBN 3-527-26820-0.

[121] HUANG, Y. D et al. On the Effect of the B2 Thermomechanical Treatment in Improving the Room Temperature Ductility of Fe3Al-based Alloys. **Intermetallics**, v. 9, n. 4, p. 331–340, abr. 2001. ISSN 0966-9795. DOI: 10.1016/S0966-9795(01)00007-3.

[122] ZHU, Su-Ming et al. Effects of Titanium Addition on the Microstructure and Mechanical Behavior of Iron Aluminide Fe_3Al. **Materials Transactions**, v. 42, n. 3, p. 484–490, 2001. DOI: 10.2320/matertrans.42.484.

[123] YANGSHAN, Sun et al. Mechanical Properties of Fe3Al-based Alloys with Cerium Addition. **Scripta Metallurgica et Materialia**, v. 33, n. 5, p. 811–817, set. 1995. ISSN 0956-716X. DOI: 10.1016/0956-716X(95)00282-Z.

[124] RAO, V. Shankar. A Review of the Electrochemical Corrosion Behaviour of Iron Aluminides. **Electrochimica Acta**, v. 49, n. 26, p. 4533–4542, out. 2004. ISSN 0013-4686. DOI: 10.1016/j.electacta.2004.05.033.

[125] WESTBROOK, JH; FLEISCHER, RL. **Structural Applications of Intermetallic Compounds**. John Wiley & Sons, 2000. v. 3. ISBN 0-471-61242-1.

[126] RAMIREZ, Bruna Niccoli. **Estudo Da Fundição Em Aluminetos de Ferro**. 2016. PhD Thesis.

[127] OHNUMA, I. et al. Ordering and Phase Separation in the b.c.c. Phase of the Fe–Al–Ti System. **Acta Materialia**, v. 46, n. 6, p. 2083–2094, mar. 1998. ISSN 1359-6454. DOI: 10.1016/S1359-6454(97)00376-5.

[128] CASTELLANOS, S. D. et al. Machinability of Titanium Aluminides: A Review. **Proceedings of the Institution of Mechanical Engineers, Part L: Journal of Materials: Design and Applications**, v. 233, n. 3, p. 426–451, 2019. ISSN 1464420718. DOI: 10.1177/1464420718809386.

[129] CHATTERJEE, S. Machinability of a Nickel Aluminide Intermetallic Alloy. **Journal of Materials Engineering and Performance**, v. 2, n. 1, p. 101–105, fev. 1993. ISSN 1059-9495, 1544-1024. DOI: 10.1007/BF02649681.

[130] BLAU, Peter J; DEVORE, E. Machining and Wear Relationships in an Ordered Intermetallic Alloy. Elsevier, p. 14, 1991.

[131] WOODYARD, J. Machining of Fe3Al Intermetallics, 1992.

[132] SAIGAL, Anil; YANG, Weiguo. Analysis of Milling of Iron Aluminides. **Journal of Materials Processing Technology**, v. 132, n. 1-3, p. 149–156, 2003. ISSN 09240136. DOI: 10.1016/S0924-0136(02)00843-9.

[133] KRATOCHVÍL, Petr. The History of the Search and Use of Heat Resistant Pyroferal© Alloys Based on FeAl. **Intermetallics**, v. 16, n. 4, p. 587–591, 2008. DOI: 10.1016/j.intermet.2008.01.008.

[134] CHOWDHURI, Sandipan et al. Machining Aspects of a High Carbon Fe3Al Alloy. **Journal of Materials Processing Technology**, v. 147, n. 1, p. 131–138, 2004. DOI: 10.1016/j.jmatprotec.2003.12.007.

[135] Selection and Application of Magnesium and Magnesium Alloys. In: INTERNATIONAL, ASM (Ed.). **ASM Handbook Volume 2 - Porperties and Selection: Irons, Steels and High Performance Alloys**. Material Park, OH, US, 2001. v. 2. P. 1424.

[136] Properties of Wrought Aluminium and Aluminium Alloys. In: INTERNATIONAL, ASM (Ed.). **ASM Handbook Volume 2 - Properties and Selection: Nonferrous Alloys and Special-Purpose Materials**. Material Park, OH, US, 2001. v. 2. P. 222.

[137] Introduction to Aluminum Alloys and Tempers. In: INTERNATIONAL, ASM (Ed.). **ASM Handbook Volume 2 - Properties and Selection: Nonferrous Alloys and Special-Purpose Materials**. Material Park, OH, US, 2001. v. 2. P. 205. DOI: 10.1007/s004310050884.

[138] Physical Properties of Carbon and Low-Alloy Steels. In: INTERNATIONAL, ASM (Ed.). **ASM Handbook Volume 1 - Properties and Selection: Irons, Steels, and High-Performance Alloys**. Material Park, OH, US. P. 517, 545.

[139]   Physical Properties of Wrought Stainless Steels. In: INTERNATIONAL, ASM (Ed.). **ASM Handbook Volume 1 - Properties and Selection: Irons, Steels, and High-Performance Alloys**. Material Park, OH, US. P. 2102–2107.

[140]   MA, Hang. The Effect of Stress Triaxiality on the Local Cleavage Fracture Stress in a Granular Bainitic Weld Metal, p. 16.

[141]   SINGH, Rajwinder; MAHAJAN, Dhiraj K. Role of Stress Triaxiality on Ductile versus Brittle Fracture in Pre-Cracked FCC Single Crystals: An Atomistic Study. **Modelling and Simulation in Materials Science and Engineering**, v. 27, n. 5, p. 055007, jul. 2019.

[142]   RAMALINGAM, S.; HAZRA, J. Dynamic Shear Stress—Analysis of Single Crystal Machining Studies. **Journal of Engineering for Industry**, v. 95, n. 4, p. 939, 1973. ISSN 00220817.

[143]   PROGRAMME and Abstracts. In: INTERMETALLICS. Educational Center Kloster Banz, Bad Staffelstein: Karlsruhe Institute of Technology, 2019. P. 126. Disponível em: <https://www.intermetallics-conference.de/fileadmin/congress/media/im2019/pdf/Intermetallic_Proceedings_2019.pdf>.

[144]   SASAKI, Tomohiro; YAKOU, Takao. Machinability of Intermetallic Compound Fe3Al from the Viewpoint of Tool Wear. **JSME International Journal Series C**, v. 49, n. 2, p. 334–339, 2006. DOI: 10.1299/jsmec.49.334.

[145]   MCCLINTOCK, Frank A. A criterion for ductile fracture by the growth of holes. **Journal of Applied Mechanics**, 35(2), p. 363–371, 1968.

[146]   VAZ JR, M; MUÑOZ-ROJAS, PA; LANGE, MR. Damage Evolution and Thermal Coupled Effects in Inelastic Solids. **International Journal of Mechanical Sciences**, v. 53, n. 5, p. 387–398, 2011.

[147]   KREIN, R. et al. Microstructure and Mechanical Properties of Fe3Al-based Alloys with Strengthening Boride Precipitates. **Intermetallics**, v. 15, n. 9, p. 1172–1182, set. 2007. ISSN 09669795. DOI: 10.1016/j.intermet.2007.02.005.

[148]   LIU, Yanxiong; XIA, Yuanming. Study of Dynamic Mechanical Behavior of Fe3Al under Tensile Impact. **Journal of Materials Science Letters**, v. 18, p. 1611–1613, 1999.

[149]   MING, Lu; PANTALÉ, Olivier. An efficient and robust VUMAT implementation of elastoplastic constitutive laws in Abaqus/Explicit finite element code. en. **Mechanics & Industry**, v. 19, n. 3, p. 308, 2018. ISSN 2257-7777, 2257-7750. DOI: 10.1051/meca/2018021. Disponível em:

<https://www.mechanics-industry.org/articles/meca/abs/2018/03/mi170114/mi170114.html>. Acesso em: 23 nov. 2022.

[150] FISCHER, Chris. Runtime and accuracy issues in three-dimensional finite element simulation of machining. **International Journal of Machining and Machinability of Materials**, v. 6, n. 1-2, p. 35–42, jan. 2009. ISSN 1748-5711. DOI: 10.1504/IJMMM.2009.026925. Disponível em: <https://www.inderscienceonline.com/doi/abs/10.1504/IJMMM.2009.026925>. Acesso em: 24 nov. 2022.

[151] SHAW, Milton C. Adiabatic Shear Theory. In: METAL cutting principles. 2. ed. USA: Oxford University Press, 2005. P. 554–558. ISBN 0-471-35929-7. DOI: 10.1037/023990.

[152] DONG, Yuanzhe et al. Investigation of Notch-Induced Precise Splitting of Different Bar Materials under High-Speed Load. en. **Materials**, v. 13, n. 11, p. 2461, jan. 2020. ISSN 1996-1944. DOI: 10.3390/ma13112461. Disponível em: <https://www.mdpi.com/1996-1944/13/11/2461>. Acesso em: 24 nov. 2022.

[153] MILLS, W. J. Fracture Toughness of Austenitic Stainless Steels and Their Welds. en, jan. 1996. DOI: 10.31399/asm.hb.v19.a0002404. Disponível em: <https://dl.asminternational.org/handbooks/edited-volume/34/chapter/452390/Fracture-Toughness-of-Austenitic-Stainless-Steels>. Acesso em: 24 nov. 2022.

[154] CYPRYCH, D. et al. Strain Localization in Polycrystalline Material with Second Phase Particles: Numerical Modeling with Application to Ice Mixtures. **Geochemistry, Geophysics, Geosystems**, v. 17, n. 9, p. 3608–3628, set. 2016. ISSN 1525-2027, 1525-2027. DOI: 10.1002/2016GC006471.

[155] INAL, Kaan; SIMHA, Hari M.; MISHRA, Raja K. Numerical Modeling of Second-Phase Particle Effects on Localized Deformation. **Journal of Engineering Materials and Technology**, v. 130, n. 2, mar. 2008. ISSN 0094-4289. DOI: 10.1115/1.2840960.

[156] PIERRI, J; WANG, X C. Finite Element Modelling Of Strain Localisation In Shear Bands During A Cutting Process. **WIT Transactions on Engineering Sciences**, v. 6, p. 7, 1994.

[157] MORRIS, D.G.; DADRAS, M.M.; MORRIS, M.A. Strength and Ductility of Fe3Al with Addition of Cr. **MRS Proceedings**, v. 288, p. 623, jan. 1992. ISSN 1946-4274. DOI: 10.1557/PROC-288-623.

[158] YOSHIMI, K.; TERASHIMA, H.; HANADA, S. Effect of APB Type on Tensile Properties of Cr Added Fe3Al with D03 Structure. **Materials Science and Engineering: A**, v. 194, n. 1, p. 53–61, abr. 1995. ISSN 09215093. DOI: 10.1016/0921-5093(94)09659-7.

APPENDIX A – Newton-Raphton VUMAT subroutine

This annex contains the VUMAT subroutine for the Abaqus Explicit Software used to execute the damage evolution model presented in this work. It was produced *via* modifications and adaptations from the robust VUMAT implementation of Johnson-Cook plasticity model by Ming; Pantalé [149]. The contents of the VUMAT are divided in A.1, which comprises the radial return/Newton-Raphson solver and the main variables, A.2, which comprises the main core of the Johnson-Cook model, and A.3 which comprises the license of the presented code.

A.1   contents of VUMAT-NR.f

```fortran
      include 'JohnsonCook.f'
C ********************************************************************
      subroutine vumat(
C Read only -
     1   nblock, ndir, nshr, nstatev, nfieldv, nprops, lanneal,
     2   stepTime, totalTime, dt, cmname, coordMp, charLength,
     3   props, density, strainInc, relSpinInc,
     4   tempOld, stretchOld, defgradOld, fieldOld,
     5   stressOld, stateOld, enerInternOld, enerInelasOld,
     6   tempNew, stretchNew, defgradNew, fieldNew,
C Write only -
     7   stressNew, stateNew, enerInternNew, enerInelasNew )
C
      include 'vaba_param.inc'
C
      dimension props(nprops), density(nblock), coordMp(nblock,*),
     1   charLength(nblock), strainInc(nblock,ndir+nshr),
     2   relSpinInc(nblock,nshr), tempOld(nblock),
     3   stretchOld(nblock,ndir+nshr),
     4   defgradOld(nblock,ndir+nshr+nshr),
     5   fieldOld(nblock,nfieldv), stressOld(nblock,ndir+nshr),
     6   stateOld(nblock,nstatev), enerInternOld(nblock),
     7   enerInelasOld(nblock), tempNew(nblock),
     8   stretchNew(nblock,ndir+nshr),
     9   defgradNew(nblock,ndir+nshr+nshr),
     1   fieldNew(nblock,nfieldv),
     2   stressNew(nblock,ndir+nshr), stateNew(nblock,nstatev),
     3   enerInternNew(nblock), enerInelasNew(nblock)
C
      character*80 cmname

      real*8 D1, D2, D3, D4, D5, D6, GfI, GfII, Dmax,
     1 trs, j2, j3, lode, eta, r, pi, criteqps, aCompressiveInc,
     2 aTensiveInc, devS2(6), devS3(6), DE, Ds, einc
C
      parameter (
     1   itMax = 250,
     2   TolNRSP = 1.0e-4,
```

```fortran
     3    TolNRDP = 1.0e-8,
     4    neednprops = 23,
     5    neednstatev = 15,
     6    gammaInitial = 1.0e-8,
     7    sqrt23 = 0.816496580927726032732428024901 96,
     8    sqrt32 = 1.224744871391589049098642037352 9,
     9    pi = 3.14159265359)
C **********************************************************************
C **********************************************************************
      Young     = props(1)
      xnu       = props(2)
      parA      = props(3)
      parB      = props(4)
      parn      = props(5)
      parC      = props(6)
      parm      = props(7)
      pardepsp0 = props(8)
      parT0     = props(9)
      parTm     = props(10)
      taylorQ   = props(11)
      density0  = props(12)
      heatCap   = props(13)
      mCoupled  = props(14)
      D1 = props(15)        ! Bai-Wierzbicki Parameters
      D2 = props(16)
      D3 = props(17)
      D4 = props(18)
      D5 = props(19)
      D6 = props(20)
      GfI = props(21)       ! Energy Release Rate mode I
      GfII = props(22)      ! ''      ''   ''   '' II
      Dmax = props(23)              ! maximum damage
C **********************************************************************
C      twoG = Young / (1.0 + xnu)
C      twoG32 = sqrt32 * twoG
C      alamda = xnu * twoG / (1.0 - 2.0 * xnu)
C      bulk = Young / (3.0 * (1.0 - 2.0 * xnu))
C      heatFr = taylorQ / (density0 * heatCap)
C **********************************************************************
C precision
      TolNR = TolNRSP
      if (j_sys_Dimension .eq. 2) TolNR = TolNRDP
C **********************************************************************
C If first increment, only compute the elastic part of the
C constitutive law.
C This is mainly for internal use of the Abaqus software when
C package is running
C Check number of material properties
      if (stepTime .eq. 0.0) then
        if (nprops .ne. neednprops) then
          write (*,*) "Vumat subroutine needs ",
     1      neednprops," material propreties"
          write (*,*) "While ",
     1      nprops," are declared in the .inp file"
          call exit (-1)
        end if
C Check number of state variables
```

```fortran
        if (nstatev .ne. neednstatev) then
          write (*,*) "Vumat subroutine needs ",
     1      neednstatev ," state variables"
          write (*,*) "While ",
     1      nstatev ," are declared in the .inp file"
          call exit (-1)
        end if
C Printout material proprerties for debug analysis
        ! write (*,*)"Summary of the parameters for the constitutive law"
        ! write (*,*) "Elastic properties"
        ! write (*,*) "E=", Young
        ! write (*,*) "nu=", xnu
        ! write (*,*) "Johnson-Cook parameters"
        ! write (*,*) "A=", parA
        ! write (*,*) "B=", parB
        ! write (*,*) "C=", parC
        ! write (*,*) "n=", parn
        ! write (*,*) "m=", parm
        ! write (*,*) "D1=", D1
        ! write (*,*) "D2=", D2
        ! write (*,*) "D3=", D3
        ! write (*,*) "D4=", D4
        ! write (*,*) "D5=", D5
        ! write (*,*) "D6=", D6
        ! write (*,*) "GFI=", GfI
        ! write (*,*) "GFII=", GfII
        ! write (*,*) "Dmax=", Dmax
        ! write (*,*) "deps0=", pardepsp0
        ! write (*,*) "T0=", parT0
        ! write (*,*) "Tm=", parTm
        ! write (*,*) "tq=", taylorQ
        ! write (*,*) "p0=", density0
        ! write (*,*) "heatCap=", heatCap
        ! write (*,*) "coupled=", mCoupled
        ! write (*,*) "State dependent variables"
        ! write (*,*) "SDV1", stateOld (1,1)
        ! write (*,*) "SDV2", stateOld (1,2)
        ! write (*,*) "SDV3", stateOld (1,3)
        ! write (*,*) "SDV4", stateOld (1,4)
        ! write (*,*) "SDV5", stateOld (1,5)
        ! write (*,*) "SDV6", stateOld (1,6)
        ! write (*,*) "SDV7", stateOld (1,7)
        ! write (*,*) "General parameters"
        ! write (*,*) "Precision NR=",TolNR
C Check that Newton-Raphson tolerance is OK
        if (epsilon(TolNR) > TolNR) then
          ! write (*,*) "Precision requested for Newton-Raphson"
          ! write (*,*) "is better than machine precision"
          ! write (*,*) "Please change precision definition in parameters"
          ! write (*,*) "subroutine aborded ..."
          call exit (-1)
        end if
        do k = 1, nblock
          stateNew (k,8) = Young
          twoG = Young / (1.0 + xnu)
          twoG32 = sqrt32 * twoG
          alamda = xnu * twoG / (1.0 - 2.0 * xnu)
```

```fortran
            bulk = Young / (3.0 * (1.0 - 2.0 * xnu))
            heatFr = taylorQ / (density0 * heatCap)
C Trace of the strain increment tensor
            deps3 = strainInc(k,1) + strainInc(k,2) + strainInc(k,3)
C New stress tensor due to elastic behaviour
            stressNew(k,1) = stressOld(k,1)
     1        + twoG * strainInc(k,1) + alamda * deps3
            stressNew(k,2) = stressOld(k,2)
     1        + twoG * strainInc(k,2) + alamda * deps3
            stressNew(k,3) = stressOld(k,3)
     1        + twoG * strainInc(k,3) + alamda * deps3
            stressNew(k,4) = stressOld(k,4) + twoG * strainInc(k,4)
            if (nshr .gt. 1) then
              stressNew(k,5) = stressOld(k,5) + twoG * strainInc(k,5)
              stressNew(k,6) = stressOld(k,6) + twoG * strainInc(k,6)
            end if
          end do
C ********************************************************************
C end of first increment special case
        else
C ********************************************************************
C Main block of constitutive equation
C Based on the Radial return algorithm
        do k = 1, nblock
            stateNew(k,8) = stateOld(k,8)
            twoG = stateNew(k,8) / (1.0 + xnu)
            twoG32 = sqrt32 * twoG
            alamda = xnu * twoG / (1.0 - 2.0 * xnu)
            bulk = stateNew(k,8) / (3.0 * (1.0 - 2.0 * xnu))
            heatFr = taylorQ / (density0 * heatCap)
C Trace of the strain increment tensor
            deps = strainInc(k,1) + strainInc(k,2) + strainInc(k,3)
C Compute pressure and deviatoric part of the current stress tensor
            p0 = (stressOld(k,1) + stressOld(k,2) + stressOld(k,3)) / 3.0
            s11 = stressOld(k,1) - p0
            s22 = stressOld(k,2) - p0
            s33 = stressOld(k,3) - p0
            s12 = stressOld(k,4)
            if (nshr .gt. 1) then
              s23 = stressOld(k,5)
              s31 = stressOld(k,6)
            end if

C Compute s^2, s^3 and invariants
            devS2(1) = s11**2 + s12**2 + s31**2
            devS2(2) = s12**2 + s22**2 + s23**2
            devS2(3) = s31**2 + s23**2 + s33**2
            devS2(4) = s11*s12 + s12*s22 + s31*s23
            devS2(5) = s12*s31 + s22*s23 + s23*s33
            devS2(6) = s11*s31 + s12*s23 + s31*s33

            devS3(1) = devS2(1)*s11 + devS2(4)*s12 + devS2(6)*s31
            devS3(2) = devS2(4)*s12 + devS2(2)*s22 + devS2(5)*s23
            devS3(3) = devS2(6)*s31 + devS2(5)*s23 + devS2(3)*s33
            devS3(4) = devS2(1)*s12 + devS2(4)*s22 + devS2(6)*s23
            devS3(5) = devS2(4)*s31 + devS2(2)*s23 + devS2(5)*s33
            devS3(6) = devS2(1)*s31 + devS2(4)*s23 + devS2(6)*s33
```

```fortran
      sigeqv = sqrt(3./2. *(s11**2. + s22**2. +
1     s33**2. + 2.*s12**2. + 2.*s23**2. +
2     2.*s31**2. ))
      if (sigeqv .eq. 0.) then
          sigeqv = 0.1
      end if

      trs = devS3(1)+devS3(2)+devS3(3)
      j3 = trs/3.
      r = sign(abs((27./2.)*j3)**(1./3.), j3)

      eta = (p0/sigeqv)
      lode = (r/sigeqv)**3.
C Damage to initiation
      criteqps = (1/2*(D1*exp(-D2*eta)+D5*exp(-D6*eta)-D3 *
2     exp(-D4*eta)))*lode**2 + 1/2*(D1*exp(-D2*eta)-D5 *
3     exp(-D6*eta))*lode + D3*exp(-D4*eta)
C Compute initial stress norm
      if (nshr .eq. 1) then
        Snorm0 = sqrt(s11*s11 + s22*s22 + s33*s33 +
1         2.0 * s12*s12)
      else
        Snorm0 = sqrt(s11*s11 + s22*s22 + s33*s33 +
1         2.0 * (s12*s12 + s23*s23 + s31*s31))
      end if
C Compute the new pressure from the strain increment
      p1 = p0 + bulk*deps
C Prediction of the stress deviator
      s11 = s11 + twoG * (strainInc(k,1) - deps/3.0)
      s22 = s22 + twoG * (strainInc(k,2) - deps/3.0)
      s33 = s33 + twoG * (strainInc(k,3) - deps/3.0)
      s12 = s12 + twoG * strainInc(k,4)
      if (nshr .gt. 1) then
        s23 = s23 + twoG * strainInc(k,5)
        s31 = s31 + twoG * strainInc(k,6)
      end if
C Compute stress norm
      if (nshr .eq. 1) then
        Snorm = sqrt(s11*s11 + s22*s22 + s33*s33 +
1         2.0 * s12*s12)
      else
        Snorm = sqrt(s11*s11 + s22*s22 + s33*s33 +
1         2.0 * (s12*s12 + s23*s23 + s31*s31))
      end if
C Compute J2 equivalent stress
      Strial = sqrt32 * Snorm
C ********************************************************************
C Compute the Constitutive law equivalent stress due to plastic flow
C ********************************************************************
C Get the current temperature at the beginning of the increment
      if (mCoupled .eq. 0) then
        tempInit = stateOld(k,5)
      else
        tempInit = tempOld(k)
      end if
      temp = tempInit
```

```fortran
C Get the previous values of plastic strain and plastic strain increment
          epsp = stateOld(k,1)
          depsp = stateOld(k,2)
C Initialize gamma value to zero
          gamma = 0.0
C Get the previously stored yield stress of the material
          yield = stateOld(k,4)
C If the yield stress is zero
C compute the first yield stress thank's to the constitutive law
C using the default initial value of gamma
          if (yield .eq. 0.0) then
            yield = yieldStress(gammaInitial, gammaInitial/dt, temp,
     1        parA, parB, parC, parn, parm, pardepsp0, parT0, parTm)
     2        * (1. - stateOld(k,13))
          end if
C Initialize the iterate counter
          iterate = 0
          iBissection = 0
C **********************************************************************
C Plasticity criterion test and begin of plastic corrector
C **********************************************************************
          if (Strial > yield) then
C Minimum value of Gamma
            gammaMin = 0.0
C Maximum value of Gamma
            gammaMax = Strial / twoG32
C Initialize gamma to the last value except if epsp = 0.0
            gamma = stateOld(k,3)
C If epsp=0 set gamma to the default initial value of gamma
            if (epsp .eq. 0.0) gamma = sqrt32 * gammaInitial
C Update the values of epsp, depsp and temp for next loop
            depsp = sqrt23 * gamma / dt
            epsp = stateOld(k,1) + sqrt23 * gamma
            temp = tempInit + 0.5 * gamma * heatFr *
     1        (sqrt23 * yield + Snorm0)
C Initialisations for the Newton-Raphson routine
            irun = 1
C Main loop for the Newton-Raphson procedure
            do while (irun .eq. 1)
C Compute yield stress and hardening parameter
              yield = yieldStress(epsp, depsp, temp,
     1          parA, parB, parC, parn, parm, pardepsp0, parT0, parTm)
     2          * (1. - stateOld(k,13))
C Compute the radial return equation for isotropic case
              fun = Strial - gamma*twoG32 - yield
C Reduce the range of solution depending on the sign of fun
              if (fun < 0.0) then
                gammaMax = gamma
              else
                gammaMin = gamma
              endif
C Compute three hardening parameters
              hardEpsp = yieldHardEpsp(epsp, depsp, temp,
     1          parA, parB, parC, parn, parm, pardepsp0, parT0, parTm)
              hardDepsp = yieldHardDepsp(epsp, depsp, temp,
     1          parA, parB, parC, parn, parm, pardepsp0, parT0, parTm)
              hardTemp = yieldHardTemp(epsp, depsp, temp,
```

```fortran
     1               parA, parB, parC, parn, parm, pardepsp0, parT0, parTm)
C Compute the hardening coefficient
                hard = hardEpsp + hardDepsp/dt + heatFr * yield * hardTemp
C Compute derivative of the radial return equation for isotropic case
                dfun = twoG32 + sqrt23 * hard
C Compute the increment of the gamma parameter
                dgamma = fun/dfun
C Increment on the gamma value for Newton-Raphson
                gamma = gamma + dgamma
C If solution is outside of the brackets do one bisection step
                if ((gammaMax - gamma) * (gamma - gammaMin) < 0.0) then
                  dgamma = 0.5 * (gammaMax - gammaMin)
                  gamma = gammaMin + dgamma
                  iBissection = iBissection + 1
                end if
C Algorithm converged, end of computations
                if (abs(dgamma) < tolNR) irun = 0
C Update the values of epsp, depsp and temp for next loop
                depsp = sqrt23 * gamma / dt
                epsp = stateOld(k,1) + sqrt23 * gamma
                temp = tempInit + 0.5 * gamma * heatFr *
     1              (sqrt23 * yield + Snorm0)
C Increase the number of iterations
                iterate = iterate + 1
                if (iterate > itMax) then
C Break with no convergence !!
                    write (*,*) "NO CONVERGENCE in Newton-Raphson"
                    write (*,*) "After", iterate, "iterations"
                    write (*,*) "Time", stepTime, dt
                    write (*,*) "Precision", abs(fun/yield)
                    write (*,*) "Strial", Strial
                    write (*,*) "Gamma0", stateOld(k,3)
                    write (*,*) "Gamma", gamma
                    write (*,*) "Gamma M", gammaMin, gammaMax
                    write (*,*) "DGamma", dgamma
                    write (*,*) "epsp0", stateOld(k,1)+sqrt23*stateOld(k,3)
                    write (*,*) "depsp0", sqrt23*stateOld(k,3)/dt
                    write (*,*) "epsp", epsp
                    write (*,*) "depsp", depsp
                    write (*,*) "temp", temp
                    write (*,*) "hardEpsp", hardEpsp
                    write (*,*) "hardDepsp", hardDepsp
                    write (*,*) "hardTemp", hardTemp
                    write (*,*) "old sdv1", stateOld(k,1)
                    write (*,*) "old sdv2", stateOld(k,2)
                    write (*,*) "old sdv3", stateOld(k,3)
                    write (*,*) "old sdv4", stateOld(k,4)
                    write (*,*) "old sdv5", stateOld(k,5)
                    call EXIT(-1)
                end if
             end do
C ****************************************************************
C End of Newton-Raphson procedure
C ****************************************************************
C Compute the new stress tensor
             xcor = (1.0 - twoG * gamma / Snorm)
             s11 = s11 * xcor
```

```fortran
            s22 = s22 * xcor
            s33 = s33 * xcor
            s12 = s12 * xcor
            if (nshr .gt. 1) then
              s23 = s23 * xcor
              s31 = s31 * xcor
            end if
          end if
C *********************************************************************
C End of Plastic correction algorithm
C *********************************************************************


C *********************************************************************
C Damage initiation and evolution
C *********************************************************************
          einc = abs(gamma)

          damageInc = einc/criteqps

          stateNew(k,9) = stateOld(k,9) + damageInc
          if (isnan(stateNew(k,9))) then
            stateNew(k,9) = 1.0
          end if

          if (stateNew(k,9) .ge. 1.0) then
              stateNew(k,9) = 1.0
          end if
c Damage evolution
          if (stateNew(k,9) .ge. 1.0) then
c Tensive damage increase
            aTensiveInc = yield * einc
     1        * tan(lode * pi / 4.0)
     2        * charLength(k) / GfI
c Compressive damage increase
            aCompressiveInc = yield * einc
     1        * cos(lode * pi / 2.0)**2
     2        * charLength(k) / GfII

            compressiveDamageOld = stateOld(k,10)
            if (compressiveDamageNew .lt. 0.0 .and.
     1          aCompressiveInc .lt. 0.0) then
                compressiveDamageNew = compressiveDamageOld
            else
                compressiveDamageNew = compressiveDamageOld
     1          + aCompressiveInc
            end if
            stateNew(k,10) = compressiveDamageNew


c           Tensive damage stateVariable
            atensiveDamageOld = stateOld(k,11)
            if ((atensiveDamageOld .lt. 0.0) .and.
     1      (atensiveDamageNew .lt. 0.0)) then
                atensiveDamageNew = atensiveDamageOld
            else if (atensiveDamageNew .lt. 0.0) then
                aTensiveInc = 0.
            else
                atensiveDamageNew = atensiveDamageOld
```

```fortran
     1                  + aTensiveInc
              end if
              stateNew(k,11) = atensiveDamageNew
c Damage variables
              stateNew(k,12) = 1. - exp( - atensiveDamageNew)
              stateNew(k,13) = 1. - exp( - compressiveDamageNew)
c element deletion

              if ( stateNew(k,12) .ge. Dmax
     1        .or. stateNew(k,13) .ge. Dmax
     2        .or. stateNew(k,1) .ge. 8.) then
                stateNew(k,15) = 0.
              end if
            end if
C ********************************************************************
C End of damage initiation and evolution
C ********************************************************************
C Store the new plastic strain and plastic strain rate
          stateNew(k,1) = epsp
          stateNew(k,2) = depsp
C Store the value of gamma for next plastic step
          stateNew(k,3) = gamma
C Store the new yield stress of the material
          stateNew(k,4) = yield * (1. - stateNew(k,13))
C Store the number of Newton-Raphson iterations
          stateNew(k,6) = stateOld(k,6) + iterate
C Store the number of Bissection steps
          stateNew(k,7) = stateOld(k,7) + iBissection
C Store the new stress tensor
          stressNew(k,1) = s11 + p1
          stressNew(k,2) = s22 + p1
          stressNew(k,3) = s33 + p1
          stressNew(k,4) = s12
          if (nshr .gt. 1) then
            stressNew(k,5) = s23
            stressNew(k,6) = s31
          end if
C Compute the new specific internal energy
          if (nshr .eq. 1) then
            stressPower = 0.5 * (
     1        (stressOld(k,1) + stressNew(k,1)) * strainInc(k,1)
     2        + (stressOld(k,2) + stressNew(k,2)) * strainInc(k,2)
     3        + (stressOld(k,3) + stressNew(k,3)) * strainInc(k,3)
     4        + 2.0*(stressOld(k,4) + stressNew(k,4)) * strainInc(k,4))
          else
            stressPower = 0.5 * (
     1        (stressOld(k,1) + stressNew(k,1)) * strainInc(k,1)
     2        + (stressOld(k,2) + stressNew(k,2)) * strainInc(k,2)
     3        + (stressOld(k,3) + stressNew(k,3)) * strainInc(k,3)
     4        + 2.0*(stressOld(k,4) + stressNew(k,4)) * strainInc(k,4)
     5        + 2.0*(stressOld(k,5) + stressNew(k,5)) * strainInc(k,5)
     6        + 2.0*(stressOld(k,6) + stressNew(k,6)) * strainInc(k,6))
          end if
C Store the new specific internal energy
          enerInternNew(k) = enerInternOld(k) + stressPower / density(k)
C Compute the new dissipated inelastic specific energy
          if (gamma .eq. 0.0) then
```

```fortran
C Transfer the old value of the inelastic specific energy
              enerInelasNew(k) = enerInelasOld(k)
C Transfer the old value of the temperature
              stateNew(k,5) = tempInit
            else
              if (nshr .eq. 1) then
                plWorkInc = abs(0.5 * gamma*(sqrt(s11*s11 + s22*s22 + s33*s33
     1            + 2.0*s12*s12) + Snorm0))
              else
                plWorkInc = abs(0.5 * gamma*(sqrt(s11*s11 + s22*s22 + s33*s33
     1            + 2.0*(s12*s12 + s23*s23 + s31*s31)) + Snorm0))
              end if
C Store the new dissipated inelastic specific energy
              enerInelasNew(k) = enerInelasOld(k) + plWorkInc / density(k)
C Store the new temperature
              stateNew(k,5) = tempInit + heatFr * plWorkInc
              ! tempNew(k) = stateNew(k,5)
            end if
            stateNew(k,8) = Young * (1. - stateNew(k,12))
            stateNew(k,14) = ((stateNew(k,5) - parT0) / (parTm - parT0)) ** parm
            ! stateNew(k,14) = coordMp(k,1)-coordMp(k,2)
            ! if (stateNew(k,14) .gt. 0.95) then
            !   stateNew(k,15) = 0.d0
            ! end if
            ! stateNew(k,16) = heatFr
            ! stateNew(k,17) = plWorkInc
          end do
        end if
        return
        end
```

A.2   Contents of JohnsonCook.f

```fortran
C **********************************************************************
C Function to compute the Johnson-Cook yield stress
C **********************************************************************
      function yieldStress (
C Parameters
     1 epsp, depsp, temp,
C Constants of the constitutive law
     2 parA, parB, parC, parn, parm, pardepsp0, parT0, parTm )
      include 'vaba_param.inc'
C Hardening part of the Johnson-Cook law
      hardPart = parA + parB * epsp**parn
C Dependence to the deformation rate
      if (depsp .gt. pardepsp0) then
        viscPart = 1.0 + parC * log (depsp/pardepsp0)
      else
        viscPart = 1.0
      end if
C Dependence to the temperature if parT0 < temp < parTm
      tempPart = 1.0
      if (temp > parT0) then
        if (temp < parTm) then
          tempPart = 1.0 - ((temp - parT0) / (parTm - parT0))**parm
        else
```

```fortran
            tempPart = 0.0
         end if
       end if
C Compute and return the yield stress
       yieldStress = hardPart * viscPart * tempPart
       return
       end


C *********************************************************************
C Function to compute the Johnson-Cook hardening / epsp
C *********************************************************************
       function yieldHardEpsp (
C Parameters
     1 epsp , depsp , temp ,
C Constants of the constitutive law
     2 parA , parB , parC , parn , parm , pardepsp0 , parT0 , parTm)
       include 'vaba_param.inc'
C Hardening part of the Johnson-Cook law
       hardPart = parn * parB * (epsp**(parn - 1.0))
C Dependence to the deformation rate
       if (depsp .gt. pardepsp0) then
         hardPart = hardPart * (1.0 + parC * log (depsp/pardepsp0))
       end if
C Dependence to the temperature if parT0 < temp < parTm
       tempPart = 1.0
       if (temp > parT0) then
         if (temp < parTm) then
           tempPart = 1.0 - ((temp - parT0) / (parTm - parT0))**parm
         else
           tempPart = 0.0
         end if
       end if
C Compute and return the yield stress
       yieldHardEpsp = hardPart * tempPart
       return
       end


C *********************************************************************
C Function to compute the Johnson-Cook hardening / depsp
C *********************************************************************
       function yieldHardDepsp (
C Parameters
     1 epsp , depsp , temp ,
C Constants of the constitutive law
     2 parA , parB , parC , parn , parm , pardepsp0 , parT0 , parTm)
       include 'vaba_param.inc'
C Hardening part of the Johnson-Cook law
       hardPart = 0.0
C Dependence to the deformation rate
       if (depsp .gt. pardepsp0) then
         hardPart = (parA + parB * epsp**parn) * parC / depsp
       end if
C Dependence to the temperature if parT0 < temp < parTm
       tempPart = 1.0
       if (temp > parT0) then
         if (temp < parTm) then
           tempPart = 1.0 - ((temp - parT0) / (parTm - parT0))**parm
```

```
          else
            tempPart = 0.0
         end if
        end if
C Compute and return the yield stress
      yieldHardDepsp = hardPart * tempPart
      return
      end


C **********************************************************************
C Function to compute the Johnson-Cook hardening / T
C **********************************************************************
      function yieldHardTemp (
C Parameters
     1 epsp, depsp, temp,
C Constants of the constitutive law
     2 parA, parB, parC, parn, parm, pardepsp0, parT0, parTm)
      include 'vaba_param.inc'
C Hardening part of the Johnson-Cook law
      hardPart = parA + parB * epsp**parn
C Dependence to the deformation rate
      if (depsp .gt. pardepsp0) then
        viscPart = 1.0 + parC * log (depsp/pardepsp0)
      else
        viscPart = 1.0
      end if
C Dependence to the temperature if parT0 < temp < parTm
      tempPart = 0.0
      if (temp > parT0 .and. temp < parTm) then
        tempPart = -parm*(((temp - parT0)/(parTm - parT0))**(parm))
     1    / (temp - parT0)
      end if
C Compute and return the yield stress
      yieldHardTemp = hardPart * viscPart * tempPart
      return
      end


C **********************************************************************
C Function to compute the numerical Johnson-Cook hardening / epsp
C **********************************************************************
      function yieldHardEpspNum (
C Parameters
     1 yield, epsp, depsp, temp,
C Constants of the constitutive law
     2 parA, parB, parC, parn, parm, pardepsp0, parT0, parTm)
      include 'vaba_param.inc'
C Increment of the plastic strain
      deltaEpsp = 1.0e-1
      if (j_sys_Dimension .eq. 2) deltaEpsp = 1.0e-8
      epspForward = epsp + deltaEpsp
c yieldForward
      yieldForward = yieldStress (epspForward, depsp, temp,
     1 parA, parB, parC, parn, parm, pardepsp0, parT0, parTm)
      yieldHardEpspNum = (yieldForward - yield) / deltaEpsp
      return
      end
```

```fortran
C **********************************************************************
C Function to compute the numerical Johnson-Cook hardening / depsp
C **********************************************************************
      function yieldHardDepspNum (
C Parameters
     1 yield , epsp , depsp , temp ,
C Constants of the constitutive law
     2 parA , parB , parC , parn , parm , pardepsp0 , parT0 , parTm)
      include 'vaba_param.inc'
c Increment of the plastic strain rate
      deltaDepsp = 1.0e-1
      if (j_sys_Dimension .eq. 2) deltaDepsp = 1.0e-8
      depspForward = depsp + deltaDepsp
c yieldForward
      yieldForward = yieldStress (epsp , depspForward , temp ,
     1 parA , parB , parC , parn , parm , pardepsp0 , parT0 , parTm)
      yieldHardDepspNum = (yieldForward - yield) / deltaDepsp
      return
      end


C **********************************************************************
C Function to compute the numerical Johnson-Cook hardening / T
C **********************************************************************
      function yieldHardTempNum (
C Parameters
     1 yield , epsp , depsp , temp ,
C Constants of the constitutive law
     2 parA , parB , parC , parn , parm , pardepsp0 , parT0 , parTm)
      include 'vaba_param.inc'
c Increment of the temperature
      deltaTemp = 1.0e-1
      if (j_sys_Dimension .eq. 2) deltaTemp = 1.0e-8
      tempForward = temp + deltaTemp
c yieldForward
      yieldForward = yieldStress (epsp , depsp , tempForward ,
     1 parA , parB , parC , parn , parm , pardepsp0 , parT0 , parTm)
      yieldHardTempNum = (yieldForward - yield) / deltaTemp
      return
      end
```

A.3   Contents of LICENSE